Proceedings of the 9th Meeting of Japan CF Research Society

Edited by Hiroshi YAMADA

March 28-29, 2009

Shizuoka-ken Sangyo Keizai Kaikan

Shizuoka, Japan

PREFACE

The 9th Meeting of Japan CF Research Society, JCF9, was held at Shizuoka-ken Sangyo Keizai Kaikan, 28-29 March 2007. This is the Proceedings.

Japan CF-Research Society (JCF) was established in March 1999, with scientific presentations and annual general meeting JCF1 at Osaka University on 29-30 March, aiming at promotion of CF researches in Japan and sending the information to the world. The CF researches concern investigation of nuclear reactions that have been newly found and are considered to be taking place in the environment of condensed matter. The main goal is to develop science and technology to extract meaningful energy and extensive application of the CF phenomena. The CF researches are based on a variety of scientific fields and require collaboration efforts from nuclear physics, fusion science, radiation physics, quantum science and technology, accelerator and particle beam science, laser science, molecular dynamics, condensed-matter physics, surface physics, catalysis science, physical chemistry, metallurgy, electrochemistry, hydrogen science, thermodynamics, acoustics, and so on.

Following JCF1, we have successfully organized JCF meetings almost every year; JCF2 (Hokkaido University, 21-22 October 2000), JCF3 (Yokohama National University, 25-26 October 2001), JCF4 (Iwate University, 17-18 October 2002), JCF5 (Kobe University, 15-16 December 2003), JCF6 (Tokyo Institute of Technology, 27-28 April 2005), JCF7 (Kagoshima University, 27-28 April 2006), and JCF8 (Doshisha University, 29-30 November 2007). For almost all meetings from and after JCF4, we have published electronic versions (via internet) of Proceedings in addition to their printed versions, which are written in English. This is because we strongly intend to be one of the key societies for international cooperation and information exchange.

The scientific area of CF researches in the world is now called Condensed Matter Nuclear Science (CMNS), since establishment of The International Society for Condensed Matter Nuclear Science (ISCMNS; http://www.iscmns.org/) in 2003. Accumulation of research efforts by researchers in the world since 1989 has revealed existence of nuclear reactions in condensed matter that are considered to occur by synergic effects of nuclear and condensed-matter physics under peculiar circumstances in the condensed matter. Concrete results obtained in latest reports are especially noteworthy. Clean deuteron-related fusion with ^{4}He ash and cold transmutation of host metal and/or added nuclei in metal-hydrogen isotope systems are regarded as actual consequences of latest CMNS studies, both in experiments and theories. JCF has been keeping close relation and collaboration with ISCMNS and researchers in the world.

Papers submitted to JCF9 have been peer-reviewed by JCF Editorial Board chaired by Professor Hiroshi Yamada, Iwate University. One or two referees were offered to review each paper submitted, who made extensive reviewing to give constructive comments, questions and recommended corrections, if any. After receiving the revised versions, the papers have been accepted for publication. The Proceedings of the JCF meeting does not necessarily contain all contributions presented at the relevant JCF meeting. Some authors are permitted, if they wish, to make their contribution as "A note without reviewing" within 4 pages. Program and Abstracts of all the presentations at JCF9 are available on a JCF webpage http://dragon.elc.iwate-u.ac.jp/jcf/JCF9/.

We thank all participants of JCF9.

September 2009,

Akira Kitamura (Prof., Kobe University), Director-in-Chief, JCF
Hiroshi Yamada (Prof., Iwate University), Chairman, JCF Editorial Board

CONTENTS

THEORY

NOTE

Proceedings of JCF9, March 28-29, 2009, Shizuoka-ken Sangyo Keizai Kaikan, Shizuoka, Japan

Gas and heat balance during plasma electrolysis (2)

T. Jang, K. Matsuzawa, S. Mitsushima, and K. Ota
Chemical Energy Laboratory, Yokohama National University

Abstract : During the plasma electrolysis in potassium and sodium carbonate solutions, we observed that the evaluated amount of hydrogen and oxygen exceed theoretical amount which was calculated by the Faraday`s law. The amount of excess gas increased with the temperature of electrolyte. Excess heat also increased with temperature.

Keyword : water electrolysis; plasma electrolysis; hydrogen generation; excess heat

1. Introduction

Water electrolysis is well known as a process which produces hydrogen and oxygen with 1.23 V of theoretical cell voltage at the room temperature. Normally these reaction follows Faraday`s law for the amount of gas production, and the energy conservation law rules the energy balance.

During plasma electrolysis, an excess gas was detected comparing with Faraday`s law.[1] Moreover, there was a possibility of an excess heat production in the electrolysis.[2] These results show new method of hydrogen generation as energy resource. However, the reproducibility was not sufficient, and an explanation of the phenomena was required. In previous study, the concentration of electrolyte affected the outbreak and expire voltage of plasma, and reproducibility of excess gas evaluation were conformed. In this study, we have studied behavior of gas and energy balance at different temperature of electrolyte during the plasma electrolysis, and evaluated the error range of them.

2. Experimental

Figure 1 is a schematic draw of the electrolytic flow cell. The cell was composed of an acrylic tubing, which had an internal diameter of 2 cm, an external diameter of 5 cm, and a length of 30 cm. The anode was a 20mm diameter, 10mm in length hollow cylindrical platinum which has 99.99% purity with 55mesh. The cathode was a 1.5mm diameter tungsten rod which has 99.95% purity, and coated with Teflon tube except 10mm for the cathode. It was placed at the center of the cylindrical anode. The distance between the electrodes was about 10 mm.

Plasma occurred at the cathode, 200 V of cell voltage, and decreased to 110 V for constant voltage experiment. The electrolyte temperature of the inlet and outlet of the cell was measured with Pt-100 resistance thermometers (HAYASHI DENKO, JIS C 1604-1997, range: -73 – 373 K, accuracy: ± (0.15+0.002×temperature)K, repeatability : ±0.15 K).

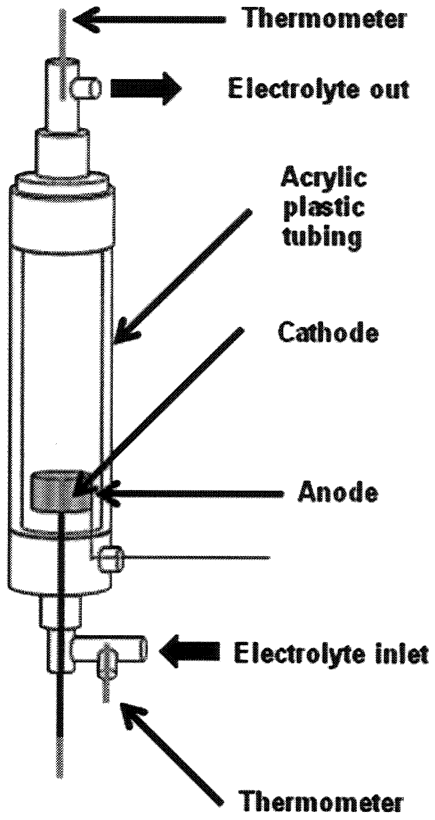

Fig. 1 Schematic draw of electrolyte flow cell

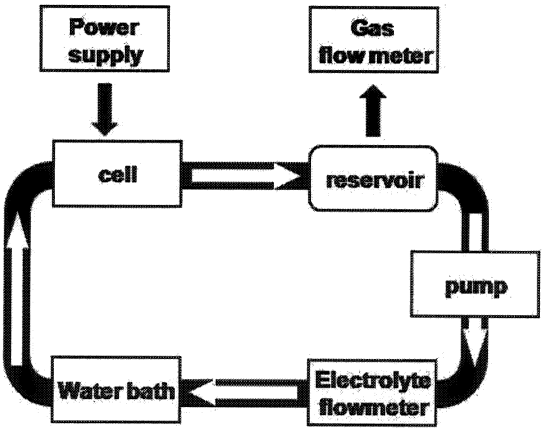

Fig. 2 Schematic draw of flow system.

Figure 2 is a schematic draw of the flow cell system. The electrolyte circulated in the system accelerated by pump (IWAKI PUMPS, V-15SCG1T, range: 0.4 – 1400ml/min 273 - 393 K), passing through a reservoir and electrolyte flowmeter (KOFLOC, FM3101, range : 0.4 - 4 L/min, 273 - 363 K, accuracy : ± 3%, repeatability: ± 0.5F.S.). Hydrogen and oxygen generated during electrolysis were separated at the reservoir, and the rate of gas generation was measured by gasflowmeter (HORIBA STEC, VP-3U, range: 20 - 1000ml/min, accuracy : 0.5%,). The electrolyte was 0.2mol/L Na_2CO_3, K_2CO_3 light water solution.

At the each experiment, inlet temperature of the electrolyte were kept at 299, 305, 311, and 323 K. The flow rate of the electrolyte were varied to maintain the temperature difference between inlet and outlet less than 5 K, and it ranged from 12 to 18 ml/sec.

During the electrolysis, cell voltage, current, inlet and outlet temperatures of the electrolyte, room temperature, reservoir temperature, and the electrolyte flow rate were measured. The input energy was calculated as the product of the cell voltage and the current.

The output of energy was the sum of the heat energy which calculated from the enthalpy change of the electrolyte, and latent energy. The latent energy was determined from the flow rate of the gaseous product. The energy balance was calculated by the following equations.

$$EB = \frac{f_E \cdot \Delta T \cdot d \cdot C_p + f_g \cdot \Delta H}{U \cdot I} \quad (1)$$

U , I , f_E , ΔT , d , C_P , f_g , ΔH , and EB were the cell voltage, the cell current, the electrolyte flow rate, the

temperature increase between the inlet and outlet of the electrolyte, the density of the electrolyte, heat capacity of the electrolyte, the generated gas flow rate, the latent energy of the H_2 and O_2 evolution, and the energy balance.

Table 1 shows the density and heat capacity of Na_2CO_3, K_2CO_3 light water solution from 299 to 323 K. Change of electrolyte density and heat capacity of temperature was too small to consider the effect of them.

Table 1 Density and heat capacity of 0.2 M 299 - 323 K Na_2, K_2CO_3 solution.[3)]

Electrolyte	Density ($g \cdot cm^{-3}$)	C_p ($J \cdot K^{-1}g^{-1}$)
Na_2CO_3	1.016	4.108
K_2CO_3	1.021	4.040

The current efficiency is the gas generation amount per the theoretical amount by the Faraday's law. Therefore, the details are as follows;

$$n_{ex} = (P_{air} - P_{vapor}) \cdot v_e / (R \cdot T) \quad (2)$$

$$n_{th} = N_a \times I / F \quad (3)$$

$$\eta = n_{ex} \times n_{th} \quad (4)$$

n_{ex}, P_{air}, P_{vapor}, v_e, R, T, n_{th}, N_a, F, and η were gas generation per second, atmospheric pressure, vapor pressure, generated gas flow rate, gas constant, temperature of produced gas during electrolysis, theoretically generated gas flow rate, gas generation amount per electron, Faraday constant, and gas balance. The theoretical generated gas flow rate was determined from Faraday's law of water electrolysis. Therefore, the ratio of hydrogen to oxygen was 2:1.

3. Result and discussion

Figure 3 shows the average of cell current during 1 hour experiments as a function of the average inlet temperature of 0.2 mol / L K_2CO_3 and Na_2CO_3 electrolyte. Although the current was higher when K_2CO_3 solution was introduced than the Na_2CO_3, K_2CO_3 showed rapid decrease of current depend on the temperature of electrolyte than Na_2CO_3 does.

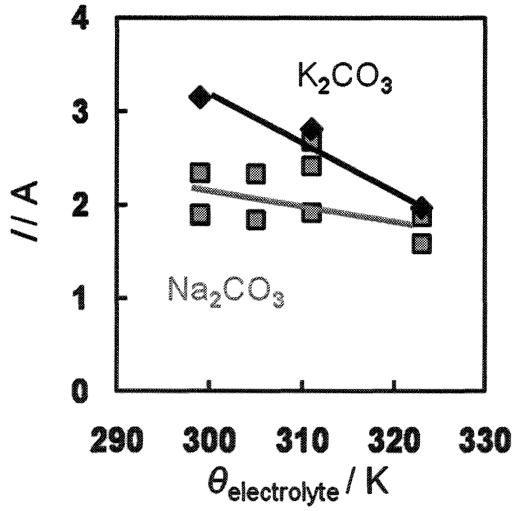

Fig. 3 Relationship between current and electrolyte temperature during 110V plasma electrolysis using 0.2M Na_2, K_2CO_3 solution.

Figure 4 shows the average latent energy of the hydrogen which produced during the 1 hour electrolysis as a function of the inlet electrolyte temperature. When K_2CO_3 solution

was introduced, the amount of the enthalpy and evaluated gas was higher than that of Na_2CO_3solution.

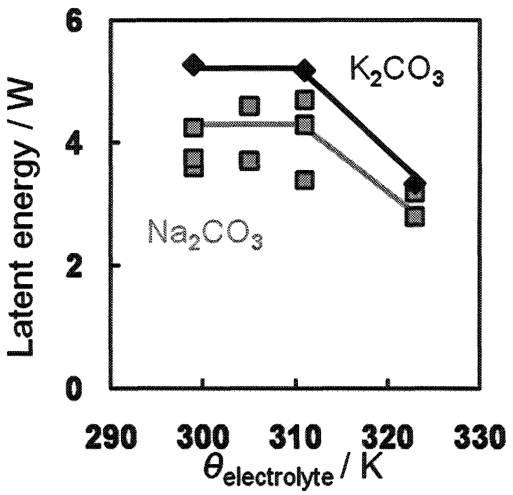

Fig. 4 Relationship between latent energy and electrolyte temperature during 110V plasma electrolysis using 0.2M Na_2, K_2CO_3 solution.

Figure 5 shows the average heat energy during the electrolysis as a function of the inlet electrolyte temperature. Despite the current decreased with the temperature as shown in Fig. 3, heat energy was almost independent of it.

Figure 6 shows the gas balance during the electrolysis. In every experiment, at least 10% of excess gas evaluation was observed. The balance was higher with K_2CO_3, but gradually decreased with the temperature of electrolyte.

Figure 7 shows the energy balance during the electrolysis. Although the energy balance was below the 100% under low inlet temperature, excess heat generation up to 140% was observed when the temperature of electrolyte was high. Comparing K_2CO_3 and Na_2CO_3 solution, K_2CO_3 solution showed higher energy balance.

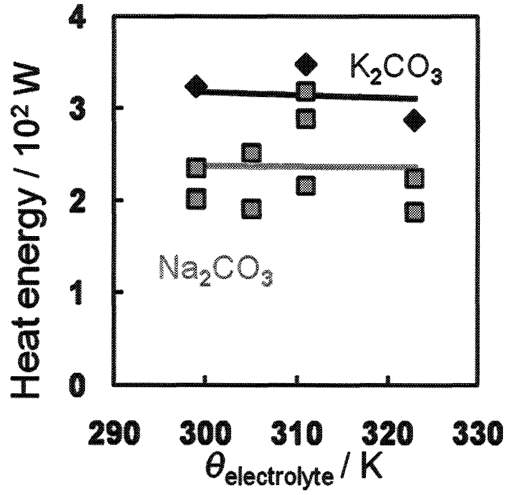

Fig. 5 Relationship between heat energy and electrolyte temperature during 110V plasma electrolysis using 0.2M Na_2, K_2CO_3 solution.

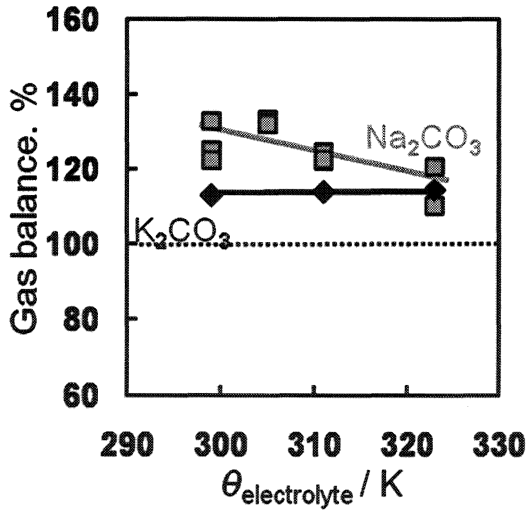

Fig. 6 Relationship between gas balance and electrolyte temperature during 110V plasma electrolysis using 0.2M Na_2, K_2CO_3 solution.

Figure 8 shows the spectrum of plasma emission while various temperature of electrolyte introduced. In this spectrum, peak

of H and O at 655.8 nm and 776.75, 844.23 nm was observed. These results suggest that the possibility of direct heat decomposition of water by the plasma.

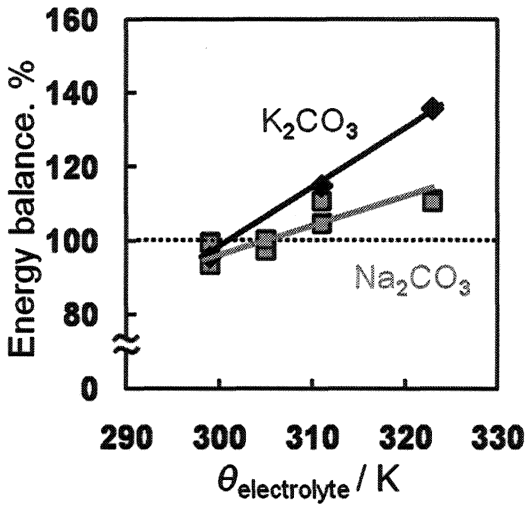

Fig. 7 Relationship between energy balance and electrolyte temperature during 110V plasma electrolysis using 0.2M Na_2, K_2CO_3 solution.

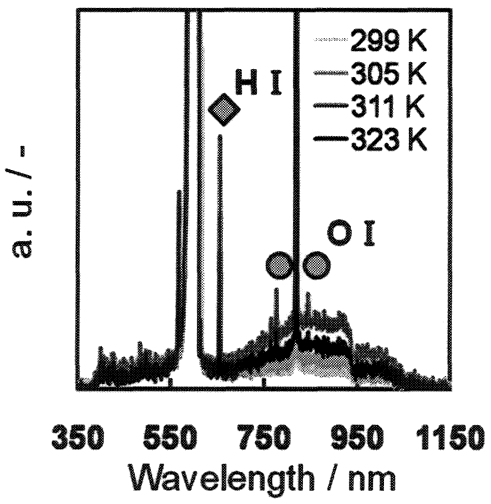

Fig. 8 Spectrum of plasma emission during 110V plasma electrolysis using 0.2M $NaCO_3$ solution.

4. Conclusions

During the plasma electrolysis using various temperature of 0.2mol/L K_2CO_3 and Na_2CO_3 solution, exceed gas evaluation was observed, and energy balance excess 100% using high temperature of electrolyte. Although the error range of gas was about 92 – 108% and energy balance was 94 – 107%, gas always exceed 108% and energy exceed 107% using high temperature of electrolyte. Considering the spectrum of plasma emission, there is a possibility that the direct heat decomposition of water occurs.

References

1. T. Mizuno, T. Ohmori, T. Akimoto, and A. Takahashi,*Jpn. J. Appl. Phys.* **39**, 6055(2000)

2. T. Mizuno, T. Akimoto, K. Azumi, and T. Ohmori, *Jpn. J. Appl. Phys.* **44**, 396 (2005)

3. Nihon kagakukai. Kagakubinran kisohen 2nd edition, 774 .(1966)

Proceedings of JCF9, March 28-29, 2009, Shizuoka-ken Sangyo Keizai Kaikan, Shizuoka, Japan

Investigation of Transmutation from Sr to Mo Using Deuterium Permeation through Palladium Membranes

Junsi Gao, Tatsumi Hioki, Naoko Takahashi, Shogo Hibi, Atsushi Murase and Tomoyoshi Motohiro

Solar Energy Utilization-Domain, Frontier Research Center,
Toyota Central Research & Development Laboratories, Inc.,
Nagakute, Aichi 480-1192, Japan, E-mail: e1424@mosk.tytlabs.co.jp

Based on the progresses of the first stage experiments where we developed a new method for eliminating sulfur contamination and obtained the high permeation rate [1], we carried out the permeation experiments relating to the low energy nuclear transmutations using three kinds of the palladium membranes; Sr-implanted pure Pd membranes, Sr-implanted multi-layered Pd membranes for investigating element transmutation from Sr to Mo, and third, pure palladium foils without Sr-implantations in order to check the impurity Mo. For the Sr-implanted pure Pd system, the as-purchased Pd foil was first annealed in a vacuum chamber and air furnace, then, Sr ions were implanted into it, and the D_2 permeation through it was performed for about 10 days. X-ray photoelectron spectroscopy (XPS) method was used. For all the permeated samples, Mo atoms were detected on their surfaces. Using additional pure Pd samples, we have checked the origin and the frequency of Mo contamination. Then it is concluded that there is a reasonable possibility of the transmutation of Sr into Mo during the D_2 permeation through Pd membranes.

1. Introduction

Recently, the low energy nuclear transmutation has been paid attention to; this is mainly because low energy nuclear reactions could potentially provide 21st Century society a limitless and environmentally-clean energy source for generating electricity. The low energy nuclear transmutation also implies a revolution in our understanding of the nucleus, a fundamental breakthrough in science.

In 1989, Martin Fleishmann and Stanley Pons claimed achieving nuclear fusion at comparatively "cold" room temperatures — in a simple tabletop laboratory device termed an electrolytic cell. [2, 3] But other scientists could not completely reproduce their results. However, after 20 years, Mosier-Boss and colleagues presented a new result at the American Chemical Society's 237th National Meeting. [4] They observed the pattern of "triple tracks" which is caused, they claim, by high-energy nuclear particles resulting from a nuclear reaction. They say: passing the electric current through the solution caused reactions within seconds. They used a special plastic, CR-39 [5] to capture and track any high-energy particles that may have been emitted during reactions, including neutrons emitted during the fusion of deuterium atoms.

In 2002, Yasuhiro Iwamura reported another low energy nuclear transmutation. Iwamura and his colleagues at Mitsubishi's Advanced Technology Research Center have observed the direct transmutation of one element (Cs) into another (Pr) using D_2 gas permeation through a sandwich of thin alternating layers of palladium (Pd) and CaO sitting on a top layer of bulk Pd. [6, 7] This kind of transmutation experiments has been extensively studied in some detail by more than tens separate laboratories worldwide: Beijing University and Tsinghua University in China; Lab des Sciences Nucleaire in France; Frascati Laboratory and University of Leece in Italy; Hokkaido University, Mitsubishi Corporation, Iwate university and Kobe University in Japan; Kiev National Shevchenko University in Ukraine, Joint Institute for Nuclear Research in Russia; Portland University, Texas A & M University, and University of Illinois Urbana-Champaign in the USA [8-18]. Although the positive results in the reproducible experiments were obtained in several laboratories, they were not always convincing enough. This investigation is still going on. This is because it is entirely new idea that the direct nuclear transmutation was carried out from one element into another, and also because it could have a variety of potential practical applications of great importance, a new supply of cheap, clean energy. Therefore, it is very significant to investigate the realization possibility of the low-energy nuclear transmutation for a new application and a new study fields.

2. Experimental Descriptions and Apparatus

We performed the D_2 permeation experiments using three kinds of membranes: Sr-implanted pure Pd, Sr-implanted multi-layer Pd, and pure Pd without Sr-implanted. For the Sr-implanted pure Pd, the as-purchased 50μm-Pd foil (with purity up to 99.97%; Nilaco Corporation.) was first annealed in a vacuum chamber and then annealed in an air furnace. The sample with a size 25×25 mm^2 was

dip into methanol to be cleaned with supersonic wave for 3 min and then annealed in air or vacuum ($<5\times10^{-7}$Torr) at different temperatures, and finally cooled down to the ambient temperature in the furnace. In the case of Sr-implanted multi-layer Pd, the CaO/Pd multi-layer was deposited on the Pd foil which was annealed with the same procedures as in the Sr-implanted pure Pd system, and then Sr ion implantation and the D_2 permeation were carried out to it. For the pure Pd, the experimental procedures are almost same as the first kind of samples, except for Sr-implantation. In addition, for the permeated samples, we carried out a post annealing, i.e. annealing the samples in air after D_2 permeation. Before and after D_2 permeations, the surfaces of the samples were analyzed using ULVAC-PHI X-ray photoelectron spectroscopy (XPS) with Quantera SXM, which was equipped with Al-K_α (1486.6eV, 15kV-400W) X-ray source; the analysis area is 300×1500 μm, and the analysis chamber pressure was the 3×10^{-9} Torr.

Figure 1 shows the schematic of the deuterium permeation system used in this study, which consists of three main parts, palladium foil, chamber A and chamber B. Chamber A is evacuated to a pressure of 0.5 Pa, using an oil-free pump; chamber B is evacuated to a high vacuum with a pressure lower than 7×10^{-4} Pa using a turbo molecular pump. In addition, chamber A is connected to a gas storage chamber which is filled with D_2 gas, so that chamber A has a comparatively stable pressure during the permeation in the case of filling gas every ten hours.

3. Results and Discussions

3.1. Characteristics of the standard spectrum of Mo and influence of sulfur to Mo analysis.

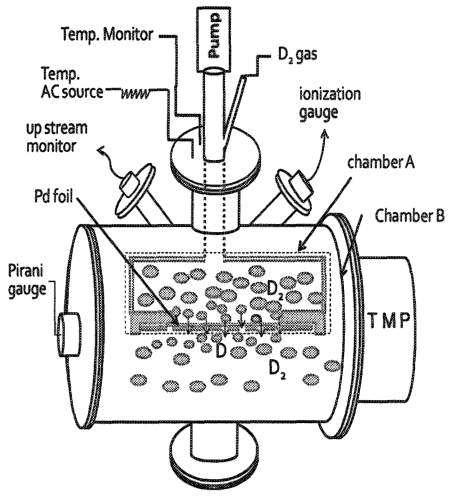

Fig. 1. Schematic of deuterium permeation apparatus.

In order to evaluate Mo element on the sample surface, it is first necessary to know a standard XPS spectrum of Mo. According to the Handbook of X-ray Photoelectron Spectroscopy, [19] there are three features of XPS spectrum of Mo: ① the position of $3d_{5/2}$ peak is located at 228.0 eV; ② the difference (ΔE) of the binding energies between two peaks is equal to 3.13 eV, ③ the intensity ratio of these two peaks is 3/2. When Mo chemical compound is formed, the 3d peaks will shift. However, the difference of binding energy and the intensity ratio are unchanged. In addition, some lines may be interfered by more intense, overlapping lines from other elements.

According to these three characteristics, we first demonstrate the result of a sample (referring to No.0 in Fig.3) which was permeated by D_2 gas for 324 hours. On this sample, initially, we didn't observe the spectrum similar to the standard spectrum of Mo. However, when it was subjected to the post annealing in air at 1000℃ for 10 min after the permeation to eliminate the sulfur segregated from the bulk during the permeation, the Mo 3d peak was observed. This showed that the "transmuted Mo" with a very small amount was usually overlapped by the S 2s line. When it was treated using the post annealing, the segregated sulfur was eliminated, and Mo could be detected. Hence, the influence of sulfur to the analysis of the transmuted Mo has been clarified. This is very significant to the evaluations of experimental results.

3.2. Mechanism of non-uniform generation of transmuted elements

It has been understood that sulfur segregation during the D_2 permeation decreased the permeation rate and hid the Mo 3d peaks by overlapping it with the S 2s line. Each S atom, on average, blocked 3.7 D_2 adsorption sites,[20] resulting in a drastic decrease of the permeation rate. In other words, deuterium atom can't permeate through around the sulfur-occupied sites. Therefore, when sulfur atom segregates at a certain place where element transmutation hasn't happened, there will be no transmuted element in that place, because deuterium atom can't permeate through there, as shown in Fig. 2. Hence, even if initial elements Sr or Cs are uniformly distributed on the sample surface, the transmuted elements may distribute non-uniformly. Iwamura et al. reported a result at ICCF12: [7] they used the ion implantation method to form a layer with laterally uniform distribution of Cs atoms on the Pd complex, but they observed the non-uniform distribution of Pr transmuted from Cs, and they

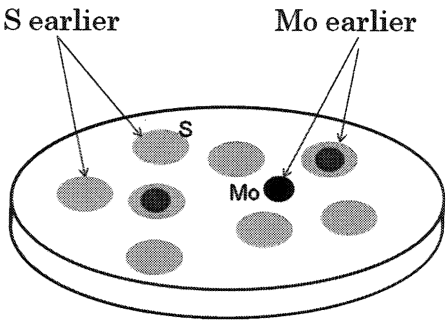

Fig. 2. A schematic of the influence of the segregated sulfur to the uniformity of the element transmutation.

left the mechanism unsolved.

3.3. Analysis method of the transmuted Mo

A D_2 permeation experiment is usually carried out for two weeks. In this permeation experiment, three important points should be taken into account, first, sulfur gradually segregates to the sample surface during the permeation, resulting in non-uniform occurrence of transmutation; second, the S 2s peak of the segregated sulfur overlapped the Mo 3d peaks, leading to masking of the weak Mo 3d peaks, third, in order to observe Mo on the permeated sample, the segregated sulfur atoms have to be eliminated. Considering the relatively high melting point (2623 ℃) of Mo, the post air annealing of 1000℃ is used to eliminate S. Thus, after the D_2 permeation, the sample was treated using the post annealing and eliminated the segregated sulfur, which is referred to the sample No.1 in Fig.3. In addition, after the post air annealing, it is very important to examine the variation of the S 2p lines. If the S 2p lines become much weaker than those of the sample without the post annealing, the segregated sulfur is surely eliminated. And in this case, it is possible to observe Mo peak. Figure 3 shows the results of the sample No.1, the peak at around the S 2p lines indeed became much weaker, compared with that of sample No.0

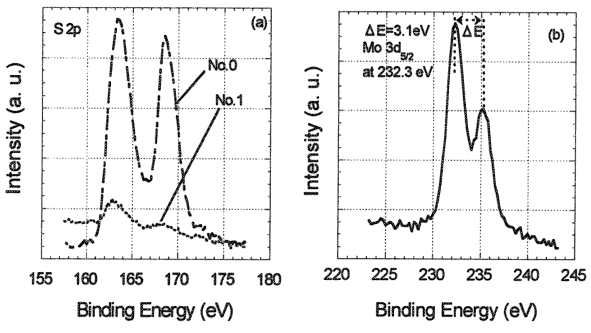

Fig. 3. The XPS spectra of sample No.1. (a) the spectrum at around S 2p; (b) the spectrum at around Mo 3d.

(in Fig.3 (a)). Meanwhile, the peak around Mo 3d was obtained (in Fig. 3(b)), which has the three features mentioned earlier for the standard Mo peak.

Since Mo was first confirmed on the permeated Sr-Pd sample, we have repeated the same experiments a few times. Another two samples were prepared according to the exactly same procedures; Mo 3d peaks of them were also confirmed on these two samples which are referred to samples No2 and No3, as shown in Fig. 4. Samples No.2 and No.3 have the same Sr-implanted density, but their peaks are a little different in the range from 232.3 eV to 234.0 eV of the binding energies, and also they are different from that of No.1.

First, the peak positions of three samples are a little different, and they are not at 228 eV, this was possibly caused by different chemical compounds of MoO_3 which was formed at high temperature post annealing; second, the peak of sample No.1 is almost symmetrical, without the component of the energy loss peak, which indicates that the observed peak is from predominantly surface distributed Mo. However, the lines of sample No.2 and No.3 are a little asymmetrical, and there is a distinct energy loss peak at Mo $3d_{3/2}$ for No.2, which indicates that the peak was formed mainly by Mo atoms residing in the subsurface layer.

3.4 Element conversions from Sr-multi-layer Pd samples

In this section, two samples of the Sr-implanted multi-layer Pd membranes will be described, which are referred to samples No.M1 and No.M2, respectively. The XPS spectra at around Mo 3d peaks are shown in Fig.5 where two spectra are compared, which are from

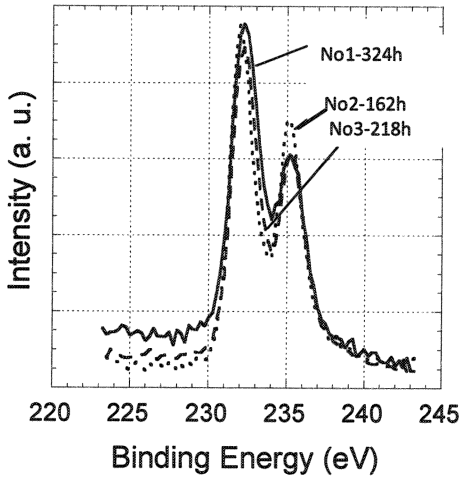

Fig. 4. The XPS spectra at around Mo 3d for samples No.1, No.2 and No.3.

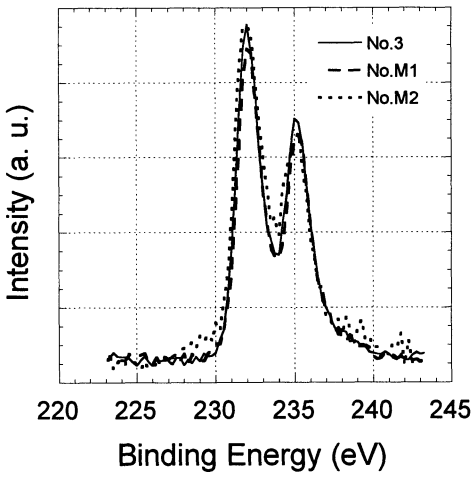

Fig. 5. Comparison of the spectra at around Mo 3d peaks in samples No.3, No.M1 and No.M2

samples No.3, No.M1 and No.M2. Although the spectrum of No.3 was obtained from Sr-Pd sample, while the spectra of No.M1 and No.M2 from Sr-multi-layer Pd samples, all the spectra looks almost the same and also the same as the standard spectrum of Mo, except for the peak shift. In addition, the almost same spectra of these 3 samples also demonstrated that the transmuted Mo is not related with CaO layer which may act as an obstacle preventing the segregation of the bulk impurities, such as S, Si and Al, to the surface during the D_2 permeation.

In addition, in order to demonstrate Mo transmutation from the permeation, we analyzed each sample before the permeation. In spite of no peaks of Mo on the Sr-Pd samples and No.M1 before the permeation, unfortunately, we noticed a Mo peak on the surface of sample No.M2 before the permeation. This Mo detected is surely the impurity Mo. It is speculated that the contaminant Mo atoms were possibly got mixed into the samples during multi-layer deposition.

3.5 About the impurity Mo

In the last section, it has been pointed out that we detected Mo atoms on the surfaces of one of two Sr-multi-Pd samples. It is supposed that this resulted from the multi-layer preparation process. However, we haven't entirely clarified whether Mo impurity exists or not in the Pd bulk, and whether it segregates from the bulk to the surface or not during the permeation. Hence, the purpose of this section is to investigate possible ways of Mo contamination, and to evaluate the influences of the Mo contaminations on the transmutation results. Four pure Pd samples without Sr-implanted were used for checking impurity Mo during the permeations, which are referred to samples No.S1-S4. And sample No.S4 was implanted with Ar ions. All samples were carefully analyzed in each step using the XPS method. First, we investigated if Mo, like sulfur, segregated from Pd bulk during the D_2 permeation. After the D_2 permeations through the 4 samples, Mo contaminations were detected on one sample. Second, we investigated the samples with the different kind of the ion implantations. Namely, Ar ions, instead of Sr ions, were implanted into a pure Pd sample (No.4 (Ar)). After the long period of D_2 permeation, no impurity Mo was detected on the Ar-implanted Pd sample.

4. Conclusions

The Table 1 and 2 shows the XPS analysis data for the three kinds of samples. ① In the case of Sr-ion-implanted pure Pd samples, before the D_2 permeation, no Mo was detected, but after the D_2 permeation, both Mo and Sr were detected, as listed in Tab.1. ②In the case of Sr-ion-implanted-multi-layer samples, before the D_2 permeation, Mo was detected in one sample; after the D_2 permeation, Mo was detected in both two samples, as listed in Tab. 1 ③ In the case of pure Pd samples, before the D_2 permeation, Mo was not detected, neither Sr do, but after the D_2 permeations, Mo was detected in only one out of 4 samples; no Mo was detected for the Ar-implanted sample (No.S4) before and after the D_2 permeations, as listed in Tab.2. Comparing above results of three kinds of the permeation experiments and the analysis results before and after permeations, it may be concluded that there is a convincing possibility of the transmutation of Sr into Mo during the D_2 permeation through Pd membranes.

Tab.1 Mo and Sr concentrations on Sr-implanted Pd

Sample Number	Sr- Pd Samples			
	after D_2		before D_2	
	Mo	Sr	Mo	Sr
No.1	1.03	20.0	0.0	5.6
No.2	1.63	16.4	0.0	12.3
No.3	1.87	8.86	0.0	5.0
No.M1	1.01	13.8	0.0	10.2
No.M2	0.79	9.76	0.27	7.44

Tab.2 Mo and Sr concentrations on the permeated pure Pd

Sample Number	Pure Pd Samples (%)					
	after D_2			before D_2		
	Mo	Sr	S	Mo	Sr	S
No.S1	0.00	0.00	0.26	0.00	0.00	0.32
No.S2	0.10	0.00	0.23	0.00	0.00	1.29
No.S3	0.00	0.00	4.00	0.00	0.00	4.20
No.S4 (Ar)	0.00	0.00	1.10	0.00	0.00	1.85

Acknowledgements

The authors gratefully acknowledge Drs. H. Azuma, Dr. Y. Itoh for their valuable discussions, Mr. A. Itoh for his technical assistance, Professor J. Kasagi of Tohoku University for his helpful discussions.

References

1. J. S. Gao, T. Hioki, N. Takahashi and T. Motohiro, JCF-8, Nov.29, 2008, Kyoto.
2. M. Fleischmann, S. Pns and M. Hawkins, J. Electroanal. Chem. **201** 301 (1989).
3. M. Fleischmann, S. Pons, M. W. Anderson, L.J. Li and M. Hawkins, J. Electroanal. Chem. **287** 293 (1990).
4. American Chemical Society. "'Cold Fusion' Rebirth? New Evidence for Existence Of Controversial Energy Source." Science Daily 23 March 2009.
5. S. Kar, M. Borghesi, L. Romagnani, S. Takahashi, and A. Zayats, JOURNAL J. of Applied Physics **101**, 044510 (2007)
6. Y. Iwamura, M. Sakano and T. Itoh, Jpn. J. Appl. Phys. **41**, 4642–4650 (2002).
7. Y. Iwamura, T. Itoh, M. Sakano, N. Yamazaki and S. Kuribayashi, Proc. ICCF12, Yokohama, Japan, Nov.27-Dec.2 (2005), World Scientific, Singapore, pp. 178-187.
8. Q.M. Wei, B. Liu, Y.U. Mo, *et al.*, Proceedings of the ICCF11, Marseilles, France, Oct. 31-Nov. 5, 351-358 (2004)
9. M. Apicella, V. Violante, F. Sarto, A. Rosada, E. Santoro, et al., Proc. ICCF12, Yokohama, Japan, Nov.27-Dec.2 (2005), World Scientific, Singapore, pp. 264-271.
10. A.G. Lipson, G.H. Miley, A.S. Roussetski, et al., Proc. ICCF12, Yokohama, Japan, Nov.27-Dec.2 (2005), World Scientific, Singapore, pp. 293-303
11. Frascati V. Violante, G. Mazzitelli and L. Capobianco, Proceedings of the ICCF10, Cambridge, Massachusetts, USA, August24-29 (2003), World Scientific, Singapore, pp.405-420, ISBN 891-256-564-7.
12. M. Apicella and V. Violante, Proceedings of the ICCF12, Yohama, Japan, Nov.27- Dec.2 (2005), World Scientific, Singapore, pp.264-271, ISBN 981-256-640-6
13. S. Taniguchi, S. Shimadu, H. Yamada and S. Narita, Proceedings of the ICCF12, Yokohama, Japan, Nov.27-Dec.2 (2005), World Scientific, Singapore, pp.284-288, ISBN 981-256-640-6.
14. A. Kitamura, R. Nishio, I. Iwai, R. Satoh, A. Taniiko and Y. Furuyama, Proceedings of the ICCF12, Yohama, Japan, Nov.27-Dec.2 (2005), World Scientific, Singapore, pp.272-277, ISBN 981-256-640-6.
15. V.I. VysoTskii, Proceedings of the ICCF12, Yohama, Japan, Nov.27-Dec.2 (2005), World Scientific, Singapore, pp.206-213, ISBN 981-256-640-6.
16. F.A. Gareev, I.E.Zhidkova, and Yu.L. Patis, Proceedings of the ICCF11, Marseilles, France, Oct.31-Nov.5 (2004), World Scientific, Singapore, pp. 459-476, ISBN 981-256-640-6.
17. J. Dash and A. Ambadkar, Proceedings of the ICCF11, Marseilles, France, Oct.31-Nov.5 (2004), World Scientific, Singapore, pp. 477-484, ISBN 981-256-640-6.
18. G.H. Miley and P.J. Shrestha, Proceedings of the ICCF10, Cambridge, Massachusetts, USA, Aug.24-29 (2003), World Scientific, Singapore, pp. 361-378, ISBN 891-256-564-7.
19. John F. Moulder, William F. Stickele, Peter E. Sobol and Kenneth D. Bomben, *Handbook of X-ray Photoelectron Spectroscopy,* Edited by Jill Chastain, Published by Perkin-Elmer Corporation Physical Electronics Division, 6509 Flying Cloud Drive, Eden Prairie, Minnesota 55344 USA.
20. A. Kulprathipanja, G.O. Alptekin, J.L. Falconer, and J. D. Way, J. Membr. Sci. **254,** 49 (2005).

Proceedings of JCF9, March 28-29, 2009, Shizuoka-ken Sangyo Keizai Kaikan, Shizuoka, Japan

Characterizing deuterium absorption/desorption behavior with multi-layered Pd

S. Narita*, H. Yamada, Y. Fukuda, H. Nagai, T. Takahashi, S. Hiyama, J. Narumi, T. Murakami

Department of Electrical Engineering and Computer Science, Iwate University

Morioka, Iwate, 020-8551, JAPAN

* narita@iwate-u.ac.jp

ABSTRACT

It is widely recognized that a specified properties of multi-layered sample plays an important role to induce low energy nuclear reaction in condensed matter, and understanding the deuterium dynamics in such sample may lead us to clarify the mechanism of the reaction. We have examined various type of multi-layered sample and their behavior of deuterium desorption process followed by a nuclear reaction. An anomalous heat evolution with explosive gas release was sometimes observed in desorption test. Additionally, numerous tracks were recorded on CR-39 detector. Those phenomena might be evidences of nuclear reaction, and associated with a peculiar behavior of deuterium desorption caused by unique sample structure. We have characterized the each sample properties and searched for the condition to induce the nuclear reaction effectively.

Keywords: multi-layered sample, Pd, Pd membrane, deuterium, CR-39

1. Introduction

In various experiments for deuterium diffusion with multi-layered or hetero-structured Pd sample, possible nuclear phenomena such as anomalous heat evolution, nuclear transmutation, and particle emission have been observed [1-3]. It is widely recognized that a specified property of deuterium dynamics in the multi-layered sample plays an important role to induce a low energy nuclear reaction (LENR) in condensed matter, and understanding the dynamics in detail may lead us to clarify the mechanism of LENR.

We have investigated deuterium behavior in absorbing and desorbing process for multi-layered Pd sample, followed by nuclear phenomena. In the study, we examined hetero-structure sample such as surface-coated Pd foil with Au and/or CaO membrane (Pd/Au, Pd/CaO, and Au/Pd/CaO). A part of the results were reported at JCF8 meeting [4]. In desorption experiment in the highly evacuated chamber, anomalous heat evolution which can be distinguished from chemical reaction was observed simultaneously with explosive gas desorption. Possible particle emission was also suggested in the experiment. We have been trying to find out the origin of those phenomena. In this paper, we report the updated results in our continuous study.

In addition, we have taken notice of a unique property of Pd membrane. Hydrogen has been considered as the source of future energy and various technologies have been widely studied. Among the energetic researches in the field, development of the technology for hydrogen purification is an important issue. For producing pure hydrogen and its isotopes, Pd membrane has been paid attention with the hydrogen permeability [5,6]. Considering the permeability of Pd membrane, we have tested the Pd foil sample coated with Pd membrane (Pd/Pd) for the purpose of controlling deuterium diffusion. The characteristics of such sample are also discussed in this study.

2. Experiment

The multi-layered samples were prepared by depositing some materials onto the Pd foil by Ar ion beam sputtering. The Pd foil with the size of 4 mm x 25 mm x 0.1 mm was employed as the substrate of the sample. After washing the sample by acetone and aqua regia, Au, CaO, or Pd layers were formed.

For loading deuterium to the sample, it was exposed to 5-10 atm deuterium gases for 23 hours. The weight of the sample was measured before and after loading, then the loading ratio (D/Pd) was calculated from the difference.

The desorbing test was examined as follows; the D loaded sample was put into the chamber which can be highly evacuated by TMP ($\sim 10^{-4}$ Pa). The pressure in the chamber and the sample temperature were

monitored continuously for ~24 hours. The ionization gauge and thermo-couple was used for their measurements, respectively. Since explosive gas out-diffusion may result the anomalous phenomenon, the sample was supplied with an electric current to enhance degassing in some sets of experiments.

The CR-39 track detector (Fukuvi Chemical Industry) was used for detecting charged particles which can emit during desorption test. The detector is made of diethyleneglycol bis allylcarbonate with the thickness of 1 mm. When a charged track crosses the CR-39, a part of the energy of the particle is deposited. As the result, chemical composition of the materials is changed along the track trajectory. If we make etching process for the detector in chemical reagent, track pit appears because the etching velocity for the area where a track passed is larger than other area. The etching conditions optimized for this study were 5 N NaOH solutions at 70 ℃ for 8 h. The 4 pieces of CR-39 were placed surrounding the sample. A piece of CR-39 was also set far from the sample in the chamber for background estimation.

3. Results and Discussion

The D/Pd for each sample type is shown in Fig.1. It is found that multi-layered structure apparently helps improve the loading ratio. The D/Pd does not seem to depend on the sample structure and the materials. It has been claimed that the frequency of observing anomalous phenomena such as excess heat increases for higher D/Pd [7]. Therefore, the validity of multi-layered structure is surely proved in terms of improving the loading ratios. Note that the D/Pd ratios shown in the figure are the value averaged over the sample entirely. The ratio can be much higher locally in a microscopic model.

Fig.2 shows the time resolved behavior of the sample temperature and the pressure in the chamber in desorption test with applying the electric current for the sample Au/Pd/CaO. The temperature increased just after applying DC current, then, it reached to the thermal equilibrium state balancing exothermic and endothermic process. After a certain time period, sudden heat evolution occurred simultaneously with gas desorption. It happened a few times in this experiment. This anomalous heat evolution was also observed for other multi-layered sample, but the trigger condition in sample structure has not been specified. Since the gas desorption is, in principle, the endothermic reaction, the temperature should decrease in the process. Moreover, the chamber was highly evacuated and the deuteride reaction which caused a heat evolution is hardly considered. Therefore, this heat evolution might imply the occurrence of nuclear phenomenon.

We have searched for the trigger conditions of

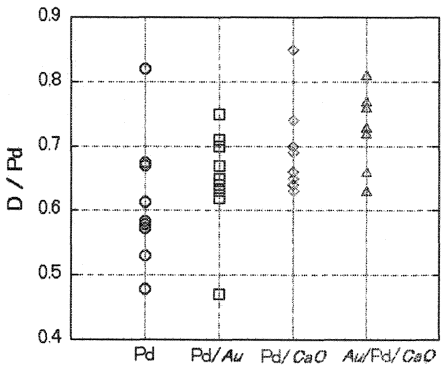

Fig.1. D/Pd for various multi-layered samples.

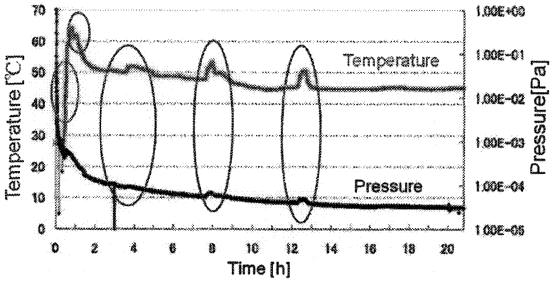

Fig.2. Time dependence of the sample temperature and the pressure in the chamber.

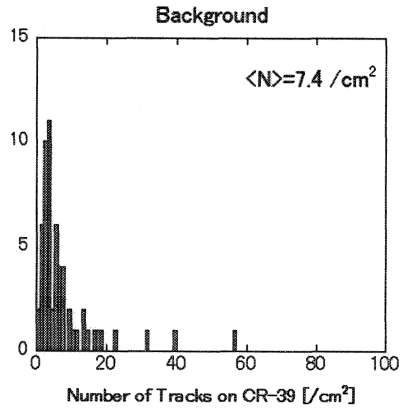

Fig.3. Number of tracks on CR-39 for background runs.

the phenomenon from the various points of view. At the JCF8, we mentioned that the initial temperature determined by Joule heat might be concerned with the trigger condition. However, with updated results after JCF8, no specified condition in the initial temperature has been observed. It is now supposed that the applying the electric current and the initial temperature of the sample determined by Joule heat is

not essential for triggering the phenomenon but just helping the deuterium diffusion from the sample.

The CR-39 analysis was performed for detecting particle emission in parallel with the measurement of heat evolution. An anomalous event was searched by investigating the excess in the number of tracks on CR-39 comparing with background runs. Fig.3 shows the number of tracks for background runs. The averaged number of tracks for these runs was found to be 7.4/cm^2. In several runs for every type of sample, we found significant excess. Here we considered the anomalous events with tracks above 40/cm^2. The number of such run is 1 out of 3 for plain Pd foil sample, 5 out of 10 runs for Pd/Au sample, 3 out of 8 runs for Pd/CaO sample, and 2 out of 10 runs for Au/Pd/CaO sample. For some runs, marked number of tracks (N>100/cm^2) was observed. Fig.4 (a)-(d) show the track diameter distributions of such runs and the background one. The anomalous tracks seem to have clear peak and the averaged diameters were smaller than that of background. The characteristics of tracks registered on the detector for these runs are definitely different from background one. If the particle is generated by a specific reaction, it has a monochromatic energy. Then, the track diameter should have a peak. Note that the collimating system is not equipped in our apparatus, and the track diameter can be wider than that in ideal case, depending on incident angle and the area size of the sample. The particle emission during the desorption experiment are now suggested. Assuming these anomalous tracks are originated by alpha particles, the energy was estimated to be above 4 MeV from the calibration data [5,8].

Although the correlation between the heat evolution and the anomalous tracks on CR-39 are not clear, both events could be considered as evidences of a nuclear reaction. While, a trigger mechanism of these phenomena are not still clear. As described above, we observed heat evolution and gas out-diffusion at almost same time. Such radical D desorption is just a hint to understand the mechanism, for now. If we control the deuterium desorption from the sample, the anomalous events may occur more frequently. Then, we took into account for the specific characteristics of Pd membrane. The multi-layered structure of crystalline bulk Pd and non-crystalline Pd membrane has a unique property in deuterium absorption/desorption [9]. Additionally, it has been proved that a fine-structure Pd such as nano-size Pd plays an important role in the study of LENR in condensed matter. Then, we examined the Pd/Pd sample.

In prior to the experiment, we investigated the surface and crystal condition of Pd membrane formed by our sputtering condition. We prepared sample of Pd membrane deposited on Si substrate by sputtering

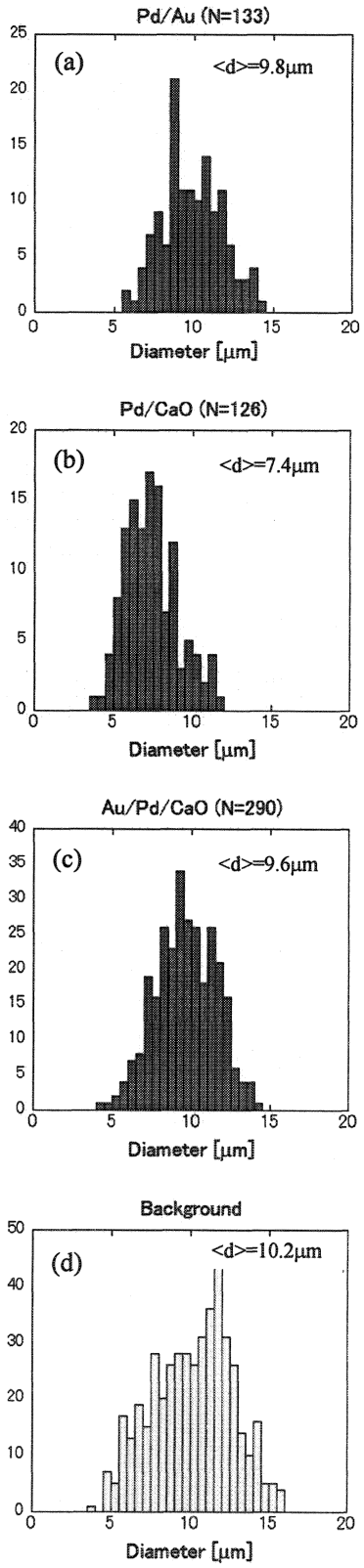

Fig.4. Diameter distributions for the events with significant number of tracks detected; (a) Pd/Au sample with N=133/cm^2, (b) Pd/CaO sample (N=126/cm^2), (c) Au/Pd/CaO (N=290/cm^2), (d) Background events.

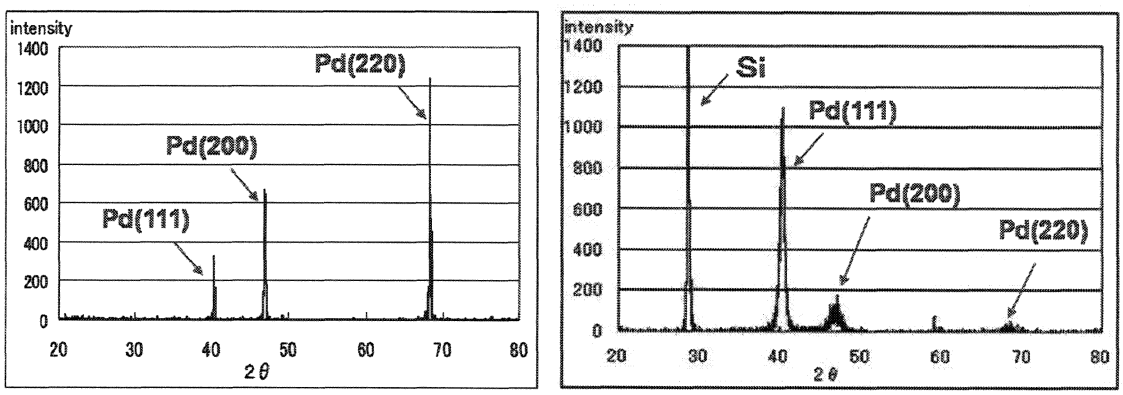

Fig.5. Diffraction angle for XRD analysis for Pd foil (left) and Pd membrane deposited on Si substrate (right).

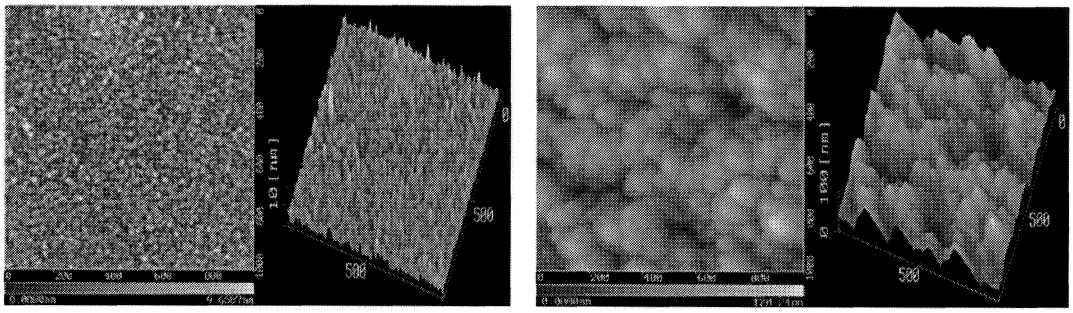

Fig.6. AFM image (top and bird eye's view; 1μm x 1μm).
Left: Pd foil, Right:Pd membrane.

and looked at crystal and surface conditions by XRD and AFM analyses. As shown in Fig.5, the XRD result showed some peaks, corresponding to Pd crystal arrangements, with slightly wider width. This implied that Pd atoms exist with polycrystalline state and the crystallinity is not so fine. Fig.6 shows AFM images of the Pd foil and Pd membrane. For Pd membrane, Pd atoms formed clusters and the grain boundaries were seen. The surface of the membrane was much rougher than that of Pd foil. It turned out that the membrane has different structure and atomic arrangement from bulk ones.

The loading test was examined for Pd/Pd sample. A peculiar behavior was seen. The rectangular-shaped sample started to deform just after opening the loading cell and heat evolution resulting from a chemical reaction of D with atmospheric gas was observed. The deformation was supposed to be caused by inner stress of the sample by radical D diffusion (Fig.7). The similar deformation has been reported by Yamaguchi *et al.* [2]. The characteristic of Pd membrane for prompting deuterium diffusion has been proved.

We performed charged particle detection by

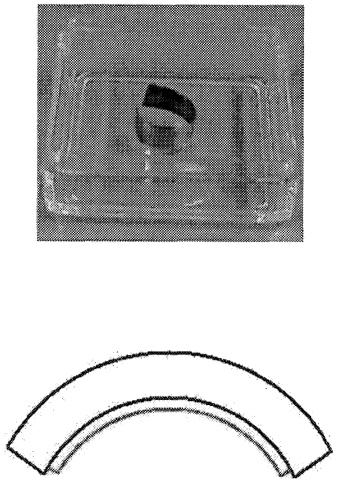

Fig.7. Sample deformation initiated by radical deuterium desorption.

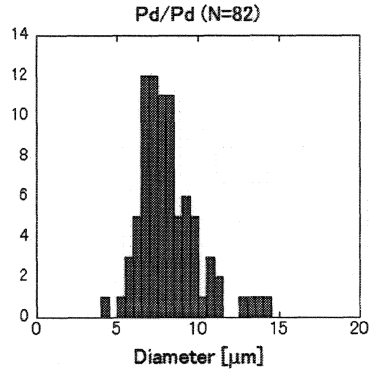

Fig.8. Diameter distribution for the events with significant number of tracks (N=82) on CR-39.

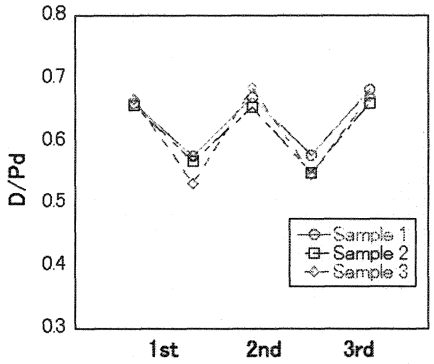

Fig.9. Change of D/Pd for the iteration of absorption and desorption experiment.

CR-39 in D desorption process for the experiment with this Pd/Pd sample. The events with anomalous tracks on CR-39 ($N>40/cm^2$) were observed in 5 out of 18 runs. The track diameter distribution for the events with tracks of $82/cm^2$ is shown in Fig.8. Comparing the distribution with the background one shown in Fig.4 (d), a clear peak has been seen. In addition, the averaged value in an anomalous run was significantly smaller. This result suggests the charged particle detection with a specific energy.

Assuming these tracks are originated from nuclear reaction, the reaction frequency can be roughly estimated. The number of events induced during desorption experiment can be expressed as follows;

$$n = N_{evt} \cdot \Omega \cdot \varepsilon$$

where, n is the number of tracks recorded, N_{evt} is the number of nuclear events, Ω is detector coverage to the sample and about ~0.1 in our configuration, and ε is the detection efficiency of CR-39 for charged track and it is usually considered to be ~1. Now, for the events with number of tracks n~100, the number of events estimated to be above 1000. This number is considerable as nuclear reactions.

Now we found the unique property of Pd membrane, that is, controlling D diffusion efficiency from the D loaded Pd. Here, we may consider this property to apply the transmutation test which has been performed by permeation experiment by MHI group and so on. MHI group has found that the conversion rate of Cs to Pr transmutation is proportional to average flow rate in their permeation experiment, and obtained ~0.3 for passing 10^{23}~10^{24} D atoms/cm^2 through sample surface [10]. As referred above, Pd/Pd sample is capable to release D atoms contained in short time and the situation is similar to higher flow rate in the permeation experiment. For example, the flow rate of 1 sccm/cm^2 in the permeation experiment is supposed to correspond to passing ~10^{18} D/cm^2/sec [11]. The experiment usually continues for 2 weeks and the total number of D is about 10^{23}~10^{24}. While in desorption method, the sample with loading ratio (D/Pd) of 0.7 contains about 10^{21} D atoms, and this number of D can pass the sample surface in quite short time controlling deuterium diffusion by using Pd/Pd sample. If we iterate absorption and desorption procedure with Pd/Pd, we may induce the selective transmutation reaction much effectively.

Then, the preliminary test of transmutation by absorption/desorption method was performed. In the permeation test by MHI, Pd/CaO complexes sample was used, but, for now, we examined prepared Pd/Au/Pd sample instead composed of thin Pd and Au layer deposited onto Pd foil (t=0.3mm). The thicknesses of Pd and Au membrane were ~500 nm and 10 nm respectively. The intermediate Au membrane was formed expecting to realize higher D density in the interface region. Cs was deposited on the surface of Pd membrane side by electrolysis using Cs_2CO_3/H_2O electrolyte. The sample with being deposited Cs was loaded D exposing 10 atm deuterium gases for 24 hours, then put in the evacuated cell for 24 hours. This set of absorbing/desorbing process was repeated three times. After the experiment, the sample composition was analyzed by ICP-MS, especially paying attention to ^{141}Pr and $^{137}La/Ba$, which was reported as transmutation products from ^{133}Cs in some experiments [1,12]. Fig.9 shows the changes of loading ratio. For every sample tested, the desorption efficiency was not so high. The total number of D which passed the sample surface was about 10^{21}. In our current study, no clear signal of ^{141}Pr or $^{137}La/Ba$ was observed. For now, various parameters in the experiment have not been optimized. It might be the reason why we have not found the transmutation reaction. In order to improving the desorption efficiency, we will test various configuration of the sample including the identical one used in MHI

permeation experiment.

4. Summary

The behavior of deuterium absorption and desorption followed by possible nuclear phenomena have been examined for the multi-layered sample. The multi-layered sample showed unique properties in deuterium dynamics. Especially, the Pd membrane coated onto Pd foil promotes the deuterium desorption effectively. This specific property can be applied to various technologies for not only LENR study but also development of hydrogen energy system. Anomalous heat evolution and tracks on CR-39 have been observed in the deuterium desorption process from the sample. We should keep trying to clarify the origin of these phenomena, especially for the relation to a nuclear effect.

References

1. Y. Iwamura *et al.*, Jpn. J. Appl. Phys. 41 (2002) 4642.
2. E. Yamaguchi *et al.*, Jpn. J. Appl. Phys. 29 (1990) L666.
3. A.G. Lipson *et al.*, Proc. of ICCF12 (2006) 293.
4. S. Narita *et al.*, Proc. of JCF8 (2008) 5.
5. Y. Shi et al., J. Membrane Sci. 322 (2009) 302.
6. W. Chen *et al.*, Int. J. Hydrogen Energy 34 (2009) 2440.
7. M. Mckubre *et al,* Proc. of ICCF3 (1992) 5.
8. A.Roussetski *et al.*, Proc. of ICCF11 (2006) 274.
9. H. Tamura (ed), "Suiso-kyuzou-goukin" (1998) (in Japanese)
10. Y. Iwamura *et al.*, Proc. of JCF5 (2003) 60.
11. Y. Iwamura *et al.*, Proc. of ICCF10 (2006) 435.
12. H. Yamada *et al.*, Proc. of JCF8 (2008) 26.

Proceedings of JCF9, March 28-29, 2009, Shizuoka-ken Sangyo Keizai Kaikan, Shizuoka, Japan

CMNS Research Progressing in Kobe University
-Deuterium Permeation and Absorption–

A. Kitamura[1]*, T. Yamaguchi[1], T. Nohmi[1], Y. Sasaki[1], Y. Miyashi[1], A. Taniike[1], Y. Furuyama[1], and A.Takahashi[2]

[1]Division of Marine Engineering, Graduate School of Maritime Sciences, Kobe University

[2]Professor Emeritus, Osaka University

*kitamura@maritime.kobe-u.ac.jp

Experimental studies on condensed matter nuclear science (CMNS) ongoing in Kobe University are reviewed. One is the subject of nuclear transmutation during forced permeation of deuterium (D) through multi-layered films of CaO/X/Pd, with X being an element to be transmuted, which is described in detail in the present paper.

The second subject is to confirm heat and ^{4}He generation by D absorption in nano-sized Pd powders reported by Arata and Zhang, and to investigate the underlying physics. We have installed a twin system to perform calorimetry during D_2 or H_2 absorption by micronized powders of Si, Pd, Pd-black, and Pd-Zr oxide compounds. The research is performed as a joint research program with Technova Inc., and is described in detail in the separate two papers presented by the joint group in the present proceedings.

Keywords: Nuclear transmutation, Condensed matter nuclear science, Permeation, Accelerator analysis, Sputtering

1. Introduction

It has been claimed that forced permeation of deuterium (D) through X-deposited (Pd/CaO)/Pd samples induced nuclear transmutation from the element X to Y, where (X, Y) being (^{133}Cs, ^{141}Pr), (^{88}Sr, ^{96}Mo), (^{138}Ba, ^{150}Sm) and (^{137}Ba, ^{149}Sm) [1,2]. In our previous work [3] to replicate the phenomena, we used XPS to characterize the CaO/Sr/Pd sample. The XPS method has a high sensitivity of detection limit, 7×10^{12} atoms/cm^2, but it is applicable only to the near-surface (< 3 nm) region, and is necessarily destructive when measurement of the depth distribution over tens of nm is required.

The basic configuration of the samples used in the present work is vacuum/(CaO/Sr/Pd)$_n$/CaO/Sr/Pd/(D_2) with exception of some runs with no CaO layer or with additional Pd layer on the top, where n = 9 or 0. In the samples used in refs. [1,2], the nuclei to be transmuted are located on the sample surface, and exposed to D_2 gas atmosphere. In most of the present work, however, they are embedded in the sample between the CaO layer and the Pd layer/bulk, and exposed to D permeating through the sample. Accordingly, we use PIXE to measure nondestructively the time-dependent concentration of the elements in the sample *in situ* and simultaneously, at the cost of increasing the sensitivity limit to 1×10^{14} atoms/cm^2.

In addition to the modified version of the sample exposure system [3,4] with reversed flow direction installed at a beam line of a tandem electrostatic accelerator 5SDH-2, a stand-alone D permeation system [5] is used to examine the phenomenon by *in-situ* or *ex-situ* PIXE/ERD analysis, respectively.

2. Experimental apparatus and procedure

The major system is an *in-situ* system shown in Fig. 1. The film was mounted on a vacuum flange with O-ring seal, and the rear surface was exposed to D_2 gas for 7 - 48 days. The sample area effective for D permeation was 3.7 cm^2, and the D_2 gas pressure was maintained at 0.04 - 0.1 MPa by occasionally replenishing the reservoir. The D flow rate through the complex sample kept at 70°C was 0.01 – 0.15 sccm, which was calculated from the pressure change. We performed *in situ* analyses for characterization of the sample before, during and after D permeation, namely, 3-MeV proton PIXE for elemental analysis, 2.5-MeV ^{3}He NRA or 4-MeV ^{4}He ERDA for D distribution analysis. The ^{4}He ERDA method has a spatial resolution of about 100 nm. For monitoring the incident particle fluence, RBS was applied simultaneously.

The other system, the *ex-situ* system shown in Fig. 2, is a D-absorption apparatus arranged independently of the accelerator analysis system. In the analysis, we intended to make a large incident angle (85°) measurement to increase PIXE sensitivity. First, we made PIXE analysis, before mounting the sample on a vacuum flange to expose the rear surface to D_2 gas at a pressure of 0.1 MPa. After finishing D permeation the PIXE analysis was made again, while NRA and ERDA for D distribution analysis were skipped in the *ex-situ* runs.

Fabrication procedure for the CaO/Sr/Pd sample is as follows. A 0.1-mm-thick Pd plate was annealed for 3 to 10 hours at 570 - 1170 K, and then immersed in aqua regia/H_2O or aqua regia/D_2O for 100 seconds. Sr atoms were deposited on one side of the Pd bulk surface using electrochemical deposition, by carefully placing the Pd bulk plate on the surface of the 10-mM $Sr(NO_3)_2/D_2O$ solution. Finally, a CaO layer with a thickness of 2 - 8 nm was deposited on the Sr/Pd samples. For samples containing thin layers of Pd such as Pd/CaO/Sr/Pd and $(CaO/Sr/Pd)_9$/CaO/Sr/Pd, the Pd thin layers with thickness of 54 nm or 18 nm were deposited also by RF sputtering.

3. Results of permeation runs

As typical examples, the PIXE spectra observed in the Run 15 for the sample (V)/Pd/CaO/Sr/Pd/(D_2) are shown in Fig. 3(a). A pair of K_α-K_β X-ray peaks are clearly found for Sr. However, those for Mo are rather difficult to identify, although an analysis software

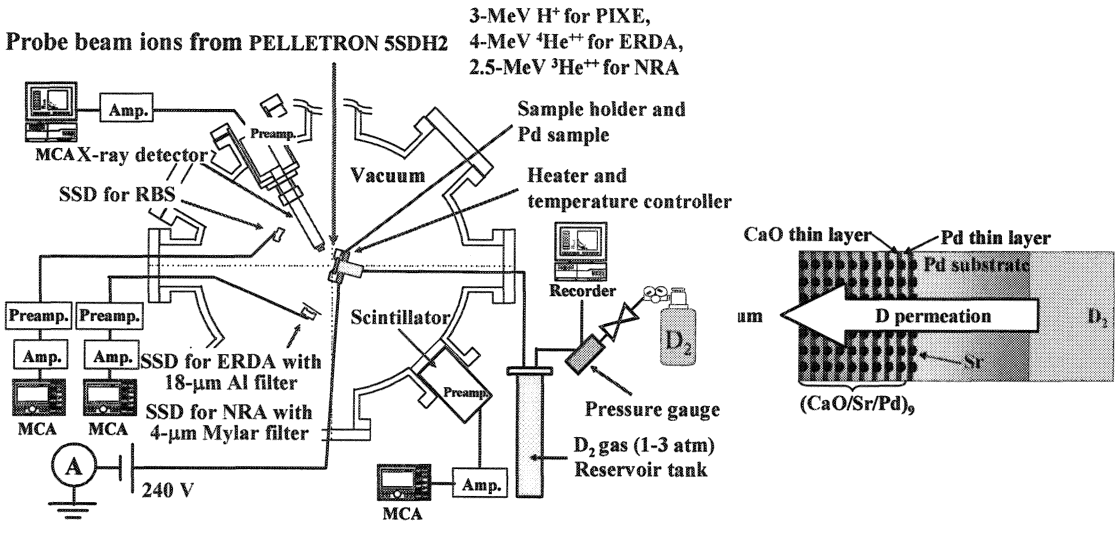

Fig.1. A schematic of the *in situ* experimental setup (left), and an example of the sample configuration (right).

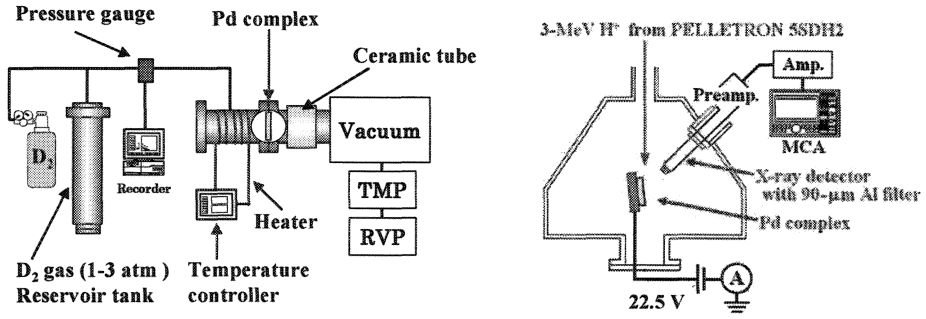

Fig. 2. A schematic of the gas permeation system (left) and the *ex situ* sample characterization system (right).

GUPIXWIN [6] can calculate the areal density of Mo, A_{Mo}, with little certainty based on the measured spectra. The areal densities of Sr and Mo, A_{Sr} and A_{Mo}, respectively, given by GUPIXWIN are shown in Fig. 3(b) as a function of the time-integrated flow rate, or the permeation fluence of D, F_D. A slight increase (0.6×10^{15} cm^{-2}) in A_{Mo} accompanied by a more pronounced decrease (3.1×10^{15} cm^{-2}) in A_{Sr} is observed after the 490-hour permeation run.

Distribution of D at 350 h (F_D = 7.8×10^{22} cm^{-2}) measured by ^{4}He-ERDA is shown in Fig. 3(c). Although the D density of about 2×10^{22} cm^{-3} ($PdD_{0.29}$) near the surface is relatively low, it increases toward the depth to the saturation value of 5.8×10^{22} cm^{-3} ($PdD_{0.85}$) at about 0.5 μm. This implies that release of D_2 molecules following recombination of atomic D at the vacuum/Pd interface is sufficiently fast, and the D flow is diffusion-limited in the near-surface region incorporating the CaO/Sr/Pd interface. On the surface, H concentration amounts 5 – 10 % of the total hydrogen isotope density, which is probably due to ion-beam-induced hydrocarbon deposition from gas phase contaminants. Since the distribution FWHM is almost the same as the spatial resolution of 100 nm, the H atoms are expected to be localized in the uppermost layer with little mixing with bulk D atoms.

Table I summarizes the results of all runs including those for samples with W additive described later in section 5. For the *in-situ* samples, *i.e.*, run #6 through #15, PIXE and ERDA measurements were performed several times during a run. The values of A_{Sr} and A_{Mo} listed in the table are those obtained in the first and the last measurements, while those of the D fluence and the composition D/Pd are at the end of the absorption run. For the *ex-situ* samples, *i.e.*, run #B1 through #B4, the PIXE measurements were done for 8 - 26 different points on each sample, and the averaged values are given in Table I.

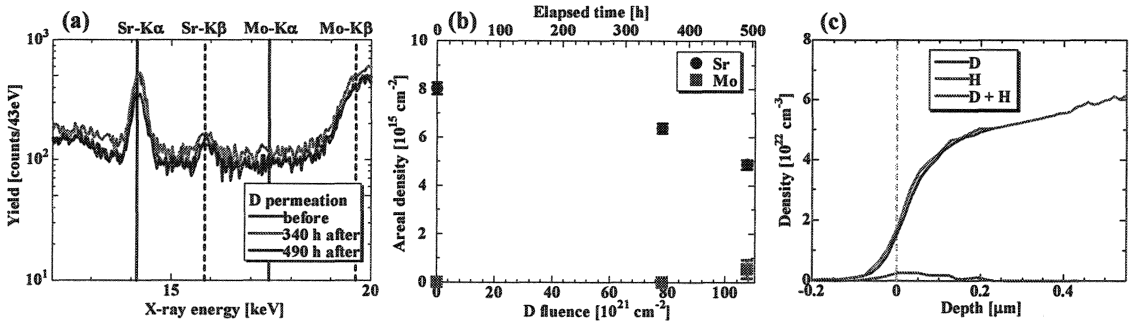

Fig. 3. (a) PIXE spectra, (b) temporal variation of the areal densities of Sr and Mo expressed as a function of D fluence (time-integrated flow rate), and (c) density profiles of hydrogen isotopes measured at 350 h in the Run 15.

Table I. Summary of permeation runs for samples with Sr or W additive.

Run #	Sample configuration (V)=vacuum, M=CaO/Sr/Pd	D flow rate (sccm)	D flux (sccm/cm^2)	Time (h)	D fluence (10^{22}cm^{-2})	D/Pd	Areal density (10^{15}cm^{-2}) before - after	
							Sr / W	Mo / Pt
6	(V)/CaO/Sr/Pd/(D_2)	0.42	0.114	1170	21.1	0.56	2.6 - 2.6	5.0 - 4.7
7	(V)/CaO/Sr/Pd/(D_2)	0.062	0.017	610	1.64	0.4	21.2 - 15.3	1.3 - 1.1
8	(V)/CaO/Sr/Pd/(D_2)	0.08	0.022	470	1.63	0.81	4.6 - 3.8	1.2 - 1.0
9	(V)/CaO/Sr/Pd/(D_2)	0.049	0.013	2320	4.39	0.59	2.5 - 2.5	0 - 1.2
10	(V)/M[9]/CaO/Sr/Pd/(D_2)	0.47	0.127	620	12.6	0.86	49.5 - 52.0	0.2 - 0.4
11	(V)/Pd/M[9]/CaO/Sr/Pd/(D_2)	0.03	0.008	970	1.33	0.02	24.1 - 21.3	0 - 0.8
12	(V)/Sr/Pd/CaO/Pd/(D_2)	0.64	0.173	440	12.4	--	3.5 - 2.2	0 - 0
13	(V)/Sr/Pd/CaO/Pd/(D_2)	0.35	0.095	660	10.1	0.07	5.0 - 4.4	0 - 0.5
14	(V)/Pd/CaO/Sr/Pd/(D_2)	0.026	0.007	470	0.51	--	4.4 - 4.2	0 - 0.8
15	(V)/Pd/CaO/Sr/Pd/(D_2)	0.5	0.135	490	10.7	0.78	8.0 - 4.9	0 - 0.6
B1	(V)/CaO/Sr/Pd/(D_2)	0.05	0.021	930	4.44	--	5.2 - 0.7	0.1 - 0.1
B2	(V)/Pd/CaO/Sr/Pd/(D_2)	0.07	0.029	810	5.4	--	8.1 - 1.5	0.3 - 0.4
B3	(D_2)/Sr/Pd/CaO/Pd/(V)	0.09	0.024	570	2.33	--	3.4 - 1.4	0.3 - 0.2
B4	(D_2)/Sr/Pd/CaO/Pd/(V)	0.34	0.092	590	8.77	--	18.8 - 7.8	0.3 - 0.4
16	(V)/Pd/CaO/W/Pd/(D_2)	1.31	0.354	170	9.87	0.17	0.16 - 0.04	2.1 - 1.2
17	(V)/Pd/CaO/W/Pd/(D_2)	0.26	1.44	170	39.6	--	0.82 - 0.82	0.35 - 0.34

In every run we were unable to find any element having the atomic number between 38 (Mo) and 46 (Pd) in the PIXE spectra. In some runs marginal increase in A_{Mo} was observed in exchange for decrease in A_{Sr}, but with little quantitative consistency; an increase in A_{Mo} was too little to compensate the decrease in A_{Sr}. In other runs we sometimes have decreasing areal densities of both Sr and Mo.

Moreover, identification of Mo peak by GUPIXWIN was not definite in most cases. We need Mo atoms with areal density larger than $3\times\square 10^{15}$ cm^{-2} to make a clear identification by PIXE analysis.

However, it is interesting to note that A_{Sr} decreased with increasing D fluence in most runs, which is clearly seen in Fig. 4(a), where A_{Sr} normalized to the initial value in each run are traced. On the other hand, in about half of the runs A_{Mo} is increasing, which is traced in Fig. 4(b).

A possible reason for the decrease might be sputtering by 3-MeV protons used as the probe beam for PIXE analysis and/or 4-MeV ^{4}He for ERDA. A simulation program ACAT [7] has been employed to estimate the sputtering yield for a Sr target to show that contribution of sputtering to the decrease would be 2 orders of magnitude smaller than the decrease observed. However, the sputtering yield for deposited atoms weakly bonded to the bulk atoms should be much larger than the bulk atoms.

The sputtering yields calculated for 1-keV proton incidence on various target materials are plotted in Fig.

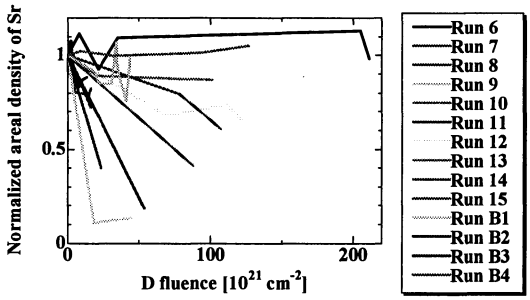

Fig. 4(a). Normalized areal density of Sr plotted against fluence (integrated flow rate) of deuterium.

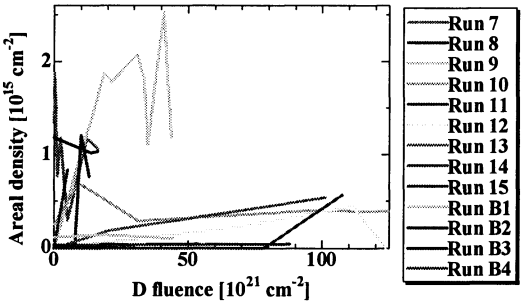

Fig. 4(b). Areal density of Mo plotted against fluence (integrated flow rate) of deuterium.

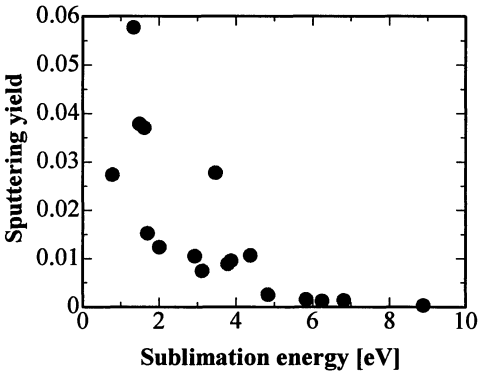

Fig. 5. Calculated sputtering yield by 1-keV protons plotted as a function of sublimation energy for various materials.

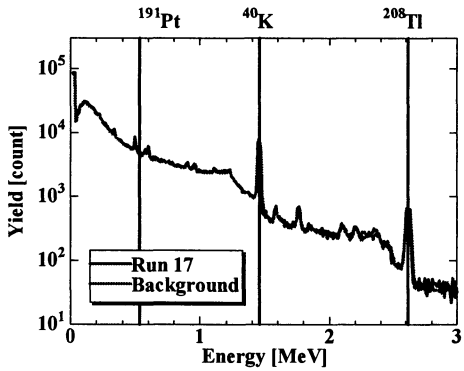

Fig. 6. Gamma ray spectra measured for a Pd/CaO/W/Pd sample after D permeation up to a fluence of 3.96×10^{23} cm^{-2}.

5 as a function of the sublimation energy of the material. It is implied that the sputtering yield for atoms such as those adsorbed, which have bonding energies of the order of 0.1 eV, can be orders of magnitude greater than the bulk atoms. This could account for the decrease in A_{Sr}. If this is the case, the measured values of A_{Mo} are also suffering from the sputtering loss, which could result in the apparently smaller "transmutation" yield.

5. Possible transmutation to radioisotope

If the transmutation product is a radioisotope, the detection will be extremely easier. The detection limit would be as low as 10^5 atoms/cm^2. If we assume the regularity of transformation that the atomic number and the mass number increase by 4 and 8, respectively, we can expect production of the following radioisotope emitting 0.538-MeV γ rays;

$$^{183}_{74}\mathrm{W}(14.4\%) \xrightarrow{\text{MHI trans.}} {}^{191}_{78}\mathrm{Pt} \xrightarrow{\text{EC},\gamma\,(2.86\mathrm{d})} {}^{191}_{77}\mathrm{Ir}.$$

For this purpose, we prepared samples with a structure (V)/Pd/CaO/W/Pd/(D_2). The thickness of the first Pd layer and the second CaO layer were 38 nm and 2 nm, respectively. The tungsten atoms were introduced into the samples by implantation with 380-keV W^{++} ions accelerated by the tandem Pelletron, and were expected to distribute at a depth of 40 nm with a range straggling of 16 nm.

Before and after D permeation, PIXE measurements were performed to reveal existence of W and Pt as shown in Table I. The latter is one of impurity elements contained in the virgin Pd samples with no radioactive isotope of ^{191}Pt. The tendency of decreasing areal densities of both W additive and impurity Pt was again confirmed as seen in Table I.

Gamma ray measurements were performed with an NaI(Tl) scintillation probe during permeation, and an HPGe detector after finishing the permeation. An example of the output spectrum from the latter detector is shown in Fig. 6. Unfortunately, we were unable to find the 0.538-MeV γ ray peak in the spectra.

6. Conclusions for transmutation works

Employing both *in situ* and *ex situ* accelerator analyses, we have tried to replicate the nuclear transmutation of Sr to Mo under deuterium permeation through a variety of multilayered CaO/Sr/Pd samples. Apparently positive results were obtained in 8 runs out of 14, although the identification of Mo peaks in the PIXE analysis was not definite. It has been implied that sputtering loss of the atoms could be responsible for the observed tendency that areal density of Sr decreases in

most cases, while increase in that of Mo is modest.

In addition to the accelerator analyses, γ-ray detection was tried for samples implanted with W atoms in expectation of transmutation from ^{183}W to radioactive ^{191}Pt, however without positive result yet.

We have at least three problems to be solved in future research; to improve the sample uniformity, to increase the D permeation rate, and to increase the amount of the additive atoms to be transmuted.

7. Deuterium Absorption to Pd Powders

Results on the second subject obtained by the cooperative work with Technova Inc. [8,9] is briefly summarized here.

To confirm heat and ^4He generation by deuterium (D) absorption in nano-sized Pd powders reported by Arata and Zhang, and to investigate the underlying physics, we have installed a twin system of double structured vessels to perform flow calorimetry during D_2 or H_2 absorption by a variety of micronized Pd samples. We can perform D_2 and H_2 absorption runs for two samples at the same time under the same environmental condition.

Characteristics of deuterium/hydrogen absorption and accompanying heat generation have been compared for three kinds of Pd powders; commercially available 0.1-μmϕ Pd powder, commercially available Pd-black, and nano-sized powder of mixed Pd and Zr oxides fabricated by Santoku Cooperation, Kobe, Japan. It has been found that the D(H)/Pd ratio and absorption energy is an increasing function of fineness of the sample surface.

The Pd·Zr mixed oxides have revealed their interesting and exciting characteristics:

1) D-gas charge in the 1st phase (zero pressure interval) gave 35 % excess heat compared to H-gas charge. In the 2nd phase of pressure rise up to the final 1 MPa, significant excess heat of about 2 kJ/g-Pd for D-gas charge was observed, while essentially zero output energy was observed for H-gas charge.

2) D(H)/Pd loading ratio reached very large values of 1.1 at the end of the 1st phase.

3) Released energy per D- or H-atom in the 1st phase was 2.2 - 2.5 eV/D or 1.3 - 2.1 eV/H, which are anomalously large compared with known values of 0.5 eV and 0.2 eV per D- or H-atom respectively for surface adsorption and lattice absorption of hydrogen atoms into bulk Pd metal.

4) No increase of neutron counts was seen, nor increase of gamma-ray counts.

References

[1] Y. Iwamura, M. Sakano and T. Itoh: Jpn. J. Appl. Phys. 41 (2002) 4642-4650.

[2] Y. Iwamura *et al.*: Proc. ICCF12, 2005, Yokohama, Japan, (World Scientific Publishing Co. Pte. Ltd, 2006) 178-187.

[3] A. Kitamura, R. Nishio, H. Iwai, R. Satoh, A. Taniike and Y. Furuyama: Proc. ICCF12, 2005, Yokohama, Japan, (World Scientific Publishing Co. Pte. Ltd, 2006) 272-277.

[4] T. Yamaguchi, T. Nohmi, H. Iwai, A. Taniike, Y. Furuyama, and A. Kitamura: Proc. 8th Meeting of Japan CF Research Society, Nov. 29-30, 2007, Doshisha Univ. (JCF Research Soc., 2008) 15-19.

[5] T. Yamaguchi, Y. Sasaki, T. Nohmi, A. Taniike, Y. Furuyama, A. Kitamura, and A. Takahashi: http://www.ler-canr.org; to be published in Proc. 14th Int. Conf. Condensed Matter Nuclear Science (ICCF14), Aug. 10-15, 2008, Washington DC.

[6] J. L. Campbell: http://pixe.physics.uoguelph.ca/gupix/main/.

[7] Y. Yamamura and Y. Mizuno : IPPJ-AM-40 (Institute of Plasma Physics, Nagoya Univ., 1985).

[8] Y. Sasaki, A. Kitamura, T. Nohmi, Y. Miyoshi, A. Taniike, A. Takahashi, R. Seto, and Y. Fujita: Deuterium Gas Charging Experiments with Pd Powders for Excess Heat Evolution, (I) Results of absorption experiments using Pd powders, this Proceedings.

[9] A.Takahashi, A. Kitamura, T. Nohmi, Y. Sasaki, Y. Miyoshi, A. Taniike, R. Seto, and Y. Fujita Deuterium Gas Charging Experiments with Pd Powders for Excess Heat Evolution, (II) Discussions on Experimental Results and Underlying Physics, this Proceedings.

Proceedings of JCF9, March 28-29, 2009, Shizuoka-ken Sangyo Keizai Kaikan, Shizuoka, Japan

Deuterium Gas Charging Experiments with Pd Powders for Excess Heat Evolution

(I) Results of absorption experiments using Pd powders

Y. Sasaki[1*], A. Kitamura[1], T. Nohmi[1], Y. Miyoshi[1], A. Taniike[1],
A. Takahashi[2], R. Seto[2], and Y. Fujita[2]
[1]Division of Marine Engineering, Graduate School of Maritime Sciences, Kobe University;
Higashinada-ku, Kobe 6580022, Japan; *088w508w@stu.kobe-u.ac.jp
[2]Technova Inc., Chiyoda-ku, Tokyo 1000011, Japan

A twin system for hydrogen-isotope absorption experiments has been constructed to replicate the phenomenon of heat and ^{4}He generation by D_2 gas absorption in nano-sized Pd powders reported by Arata and Zhang, and to investigate the underlying physics. For Pd-Zr oxide nano-powders, anomalously large energies of hydrogen isotope absorption, 2.4 ±0.2 eV/D-atom and 1.8 ±0.4 eV/H-atom, as well as large loading ratio of D/Pd =1.1 ±0.0 and H/Pd =1.1 ±0.3, respectively, were observed in the phase of deuteride/hydride formation. The sample charged with D_2 also showed significantly positive output energy in the second phase after the deuteride formation. For comparison, results for 0.1−μmϕ Pd powder samples and Pd-black samples are also shown.

Introduction

Arata and Zhang recently reported that highly pure D_2 gas charging of Pd nano-powders in the form of Pd/ZrO_2 nano-composite induced significantly higher temperatures inside the reactor vessel than on the outside wall for more than 50 hours, while runs with H_2 gas showed almost no temperature difference.[1)] To verify that the excess heat originated in a nuclear process, a QMAS was employed to show the existence of ^{4}He as nuclear ash in the vessel and in the powder after the charging. The charging system is a sophisticated and simplified version of the previous-generation DS reactor[2)]. Replication experiments using systems similar to the DS reactor with Pd-black seem to be successful[3,4)]. It is extremely important to confirm the phenomenon of heat and ^{4}He generation with fully quantitative confidence.

In the present work we constructed an experimental system to replicate the phenomenon and to investigate the underlying physics. An oxide sample of mixture of Pd (34.6 %) and Zr (65.4 %) was fabricated by Santoku Corporation, Kobe, Japan, and has an average particle size of 7.7 μm, a specific surface area of 37.1 m^2/g, and an average Pd grain size of 10.7 nm. If we assume perfect oxidation of the metal elements, 10 g of the sample contains 3.0 g of Pd.

Experimental system

The D_2/H_2 absorption system is composed of two identical chambers (an A_1·A_2 twin system): one for a D_2 gas foreground run, and the other for H_2 gas background run. As shown in Fig.1 and Fig.2 each part has an inner reaction chamber containing Pd powder and an outer chamber that is evacuated to provide thermal insulation for calorimetry. A sheath heater and a cooling water pipe (copper) are wound on the outer surface of the reaction chamber for baking the sample powder and for flow calorimetry to estimate the heat production rate, respectively. A pair of thermocouples is provided for the flow calorimetry by measuring the temperature difference between the inlet and the outlet of the cooling water.

The D_2 gas is nominally 99.5 % pure and the H_2 is 99.998 % pure. Flow rate control of D_2/H_2 gas purified through a liquid-nitrogen cold trap is made with a Pd membrane filter which also serves as an additional purifier. The Pd membrane (0.2 mm-t, 99.95 %) separates the evacuated reaction chamber (50 mℓ) and the gas reservoir filled with D_2/H_2 at 1 MPa. The gas permeation rate is controllable between 0.1 and 25 sccm by varying the membrane temperature from the room temperature to 900 K. All parameters measured are stored in a PC with an acquisition period of 1 min.

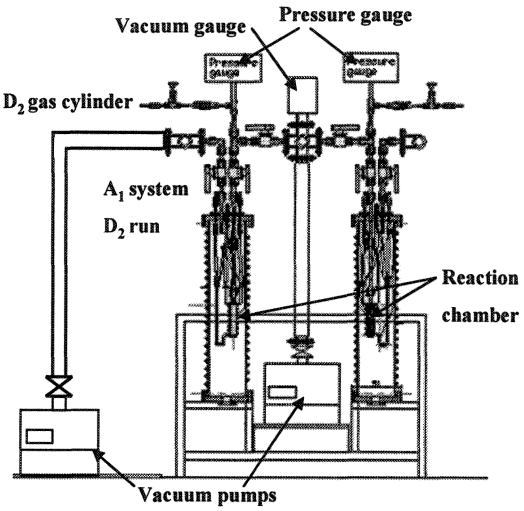

Fig.1. Reduced view of the A_1·A_2 twin system

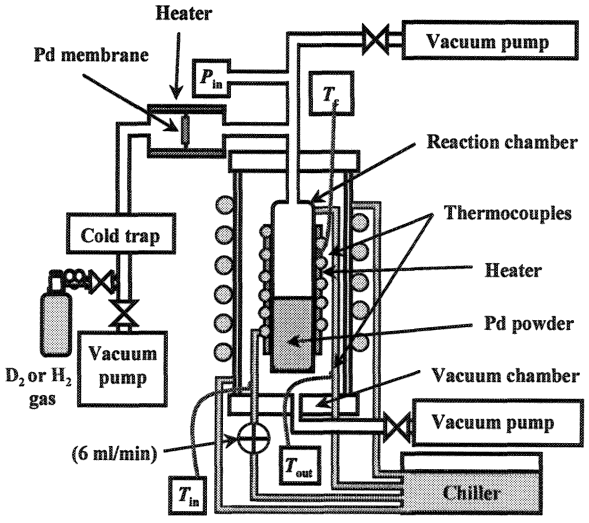

Fig.2. Functional view of A_1

Preliminary experiments

As a calibration of the flow calorimeter, we measured the heat recovery rate under a variety of conditions; with input power of 1, 3, 6 and 10 W, and D_2 gas pressure of 0, 0.1, 0.3 and 1.0 MPa in the reaction chamber. The coolant flow rate was 6 mℓ/min in all cases. The heat recovery rate was found to be almost independent of the pressure and the input power, and the averaged value is (63.1 ± 5.8) %. Temperature response to a stepwise variation of the input power was found to be expressed as a simple exponential function with a time constant of 5.2 min.

We examined temperature uncertainty and drift, with no sample powder put in the A_1 chamber filled with H_2 gas at a pressure of 1MPa. The inlet-outlet temperature difference and the output power deduced from it showed short-term fluctuation as shown in Fig.3. If we regard an experimental error in the present system as the standard deviation of the longitudinal data, the error or the uncertainty for the output power and the integrated output energy measured for the A_1·A_2 system is evaluated to be 0.014 W and 0.83 kJ for 1000-min acquisition. In the prototype system A_0, which had the larger time constant and smaller sensitivity of heat measurement, and was used in the 1st stage experiments with the 0.1-μmϕ Pd powder and the Pd-black[5], a temperature drift observed sometimes resulted in the

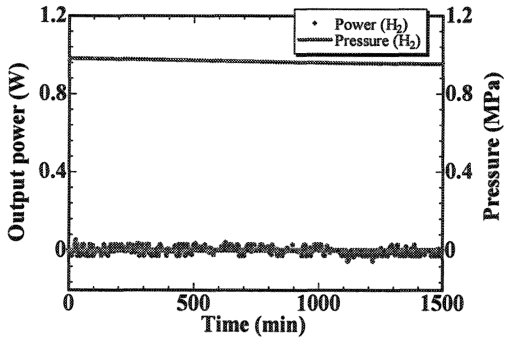

Fig.3. Blank run with no sample powder.

larger error of 4.0 kJ for 1000-min run.

Run number definition

In the following, the run number is designated by "G-PN#M", with G, P, N and M being the gas species, the powder species, powder ID, and the number of repeated use, respectively. The powder species include PP (Pd powder with particle diameter of 0.1 μm and a purity of 99.5 %), PB (Pd-black with a particle size of "300 mesh" and purity of 99.9 %), and PZ (mixed oxides of Pd·Zr). For example, "D-PB2#3" represents the third absorption run with D_2 using a Pd-black sample "2" following evacuation and baking after two cycles of evacuation-baking-absorption.

Results by ϕ0.1μm-Pd powder

First, we describe absorption runs using the A_0 system for five gram of 0.1-μmϕ Pd powder. The reaction chamber filled with the powder was evacuated and heated for baking at 430 K. Then highly pure D_2 or H_2 gas was introduced into the reaction chamber through the Pd membrane filter. The results for the case of D_2 and H_2 absorption are compared in Fig.4. After the gas was introduced, pressure did not begin to rise for a while. During this phase (the first phase) the Pd powder absorbed almost all of the D_2 (H_2) gas atoms as they flowed in, and heat was released as a result of adsorption and formation of deuterides (hydrides). After about 30 minutes, the powder almost stopped absorbing gas; the gas pressure began to rise, and the heat release from deuteride (hydride) formation subsided. This is the beginning of the 2nd phase, and the gas flow rate in the 1st phase is evaluated from the rate of the pressure increase. From the flow rate multiplied by the duration of the 1st phase, loading was estimated to reach $PdD_{0.43}$ ($PdH_{0.44}$).

The output powers are integrated over the 1st phase to give the output energies of 0.10 kJ/g-Pd(D) and 0.08 kJ/g-Pd(H), which are divided by the loading ratio of 0.43 and 0.44 to give the heat of solution ΔH_s of 0.24 eV/atom-D and 0.20 eV/atom-H, respectively. The values appear to be somewhat larger than those found in literatures[6-10]. However, they are consistent with each other, when we take into account that the differential heat of solution is a decreasing function of the loading ratio; ΔH_s = 0.15, 0.12, 0.070, and 0.061 eV/H for H/Pd ratio of 0.5, 0.55, 0.6 and 0.65[9,10]. The difference between D and H, the isotope effect, is rather large, but is not considered to be anomalous, since we find $\Delta H_s(D)/\Delta H_s(H)$ = 1.25 in ref. [9]. On the other hand, the output energies in the 2nd phase, *i.e.*, the output powers integrated over the 2nd phase with duration of 1,400 min, are smaller than the experimental error mentioned above, and "excess heat" is not meaningful in this case. The results are summarized in Table I, which includes those for the Pd-black and the Pd·Zr mixed oxide samples.

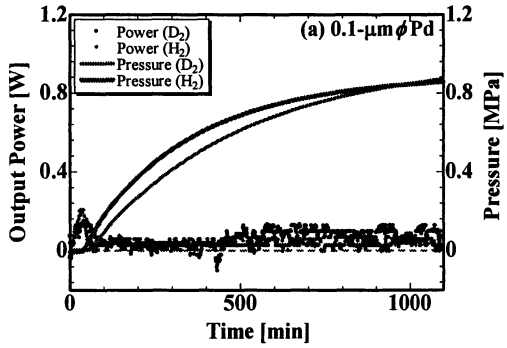

Fig.4. Evolution of heat and pressure in the vessel after introduction of D_2 gas (blue/light blue) or H_2 gas (red/pink) to 0.1-μmϕ Pd powder (D-PP1#1 and H-PP2#1). Power is slightly higher for D than H after 500 min.

Results by Pd-black

The second kind of the sample tested is commercially available 300-mesh Pd-black whose surface has a kind of nano-scale fractal structure finer than the 0.1-μmϕ

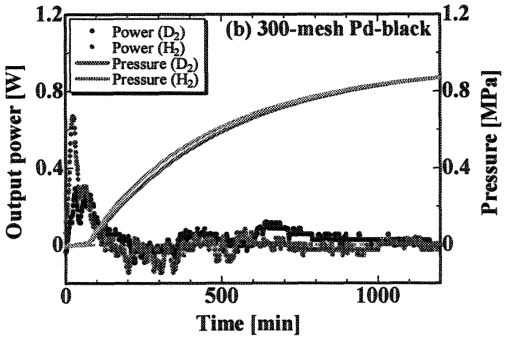

Fig.5. Evolution of heat and pressure in the vessel after introduction of D_2 gas (blue/light blue) or H_2 gas (red/pink) to 300-mesh Pd-black (D-PB1#1 and H-PB2#1). Power is slightly higher for D than H in the 2nd phase.

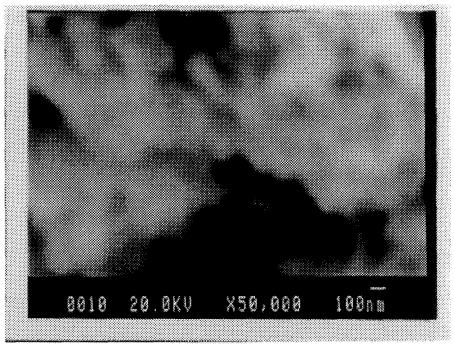

Fig.6. SEM photograph of the surface of Pd-black before the absorption run.

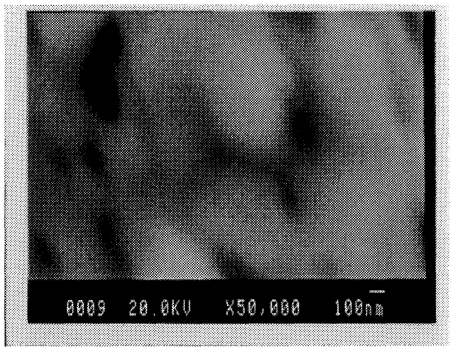

Fig.7. SEM photograph of the surface of Pd-black after the absorption run.

Pd powder. The performance of Pd-black absorption of D_2 using the A_0 system is compared with that of H_2 in Fig.5. It is very interesting to note that: (1) much higher loading to $PdD_{0.88}$ or $PdH_{0.79}$ is realized, and (2) the output energies in the 1st phase, E_{1st} = (0.67 ±0.12) eV/atom-D and (0.62 ±0.11) eV/atom-H, are 2 - 3 times larger than those for the 0.1-μmϕ Pd powder and those found in the literatures[6-10]. On the other hand, the output energy of 8.3 ± 4.5 kJ (2.6 ± 1.4 kJ/g-Pd) in the 2nd phase of D_2 absorption appears to be larger than that in the case of H_2. The difference is only marginal compared with the above-mentioned error due to the temperature drift of 5.5 kJ in the present case.

Using the improved twin system $A_1 \cdot A_2$, we compared the performance of the Pd-black sample PB3 with a prolonged duration of the 2nd phase of 4,500 min, which was subjected to repeated use with the sample baking before absorption made at 440 K for 3 h (#2), or at 570 K for 1 h (#3). The results are shown in the 6th row through the 8th in Table I.

First we notice that the first run (D-PB3#1) has essentially the same D/Pd ratio and the energy output E_{1st} as those with the A_0 system. Second the repeated use retains almost the same or even higher energy output E_{1st} in spite of the significantly smaller D(H)/Pd ratio. This interesting fact could be related to some structural change of the sample. The SEM photograph of the sample indicated clumping together and disappearance of the fine structure on the scale of several tens of nm. They are shown in Figs. 6 and 7.

As for the 2nd phase, we have little to discuss, when we take into account that they are comparable to the error of 4.0 kJ/1000-min mentioned above for the A_0 system.

Results by Pd-Zr oxide compounds

Now we describe the performance of the mixed oxides of Pd·Zr that are thought to have even finer mesoscopic structure. The results of six runs using virgin PZ samples are summarized in the last 6 rows in Table I. Those of runs with repeated use of the PZ sample will be discussed in the next paper[12] together with the above-mentioned PB samples. Using the $A_1 \cdot A_2$ twin system, the runs H-PZ(2*n*)#1 were performed

Table I. Comparison of absorption runs for the 0.1-μmϕ Pd powder (PP), the 300-mesh Pd-black (PB), and the Pd·Zr nano-composite (PZ).

Run #	weight of Pd [g]	Flow rate [sccm]	Output energy [kJ]		Specific output energy [kJ/g]		D/Pd or /Pd (1st ph.)	E1st [eV/D(H)]
			1st phase	2nd phase	1st phase	2nd phase		
D-PP1#1	5.0	2.7	0.5±0.4	2.5±4.1	0.10±0.07	0.52±0.83	0.43	0.26±0.14
D-PP1#2	5.0	3.8	0.5±0.2	4.0±4.4	0.10±0.05	0.79±0.88	0.44	0.25±0.09
H-PP2#1	5.0	5.4	0.4±0.2	2.6±3.9	0.08±0.03	0.53±0.80	0.44	0.20±0.07
D-PB1#1	3.2	3.6	1.7±0.3	8.3±4.5	0.54±0.10	2.60±1.40	0.88	0.67±0.12
H-PB2#1	3.6	4.2	1.6±0.3	(-2.2±4.6)	0.45±0.08	(-0.62±1.30)	0.79	0.62±0.11
D-PB3#1	20.0	2.9	9.3±1.1	1.1±0.5	0.47±0.06	0.06±0.02	0.79	0.65±0.08
D-PB3#2	20.0	0.9	3.3±0.5	3.4±2.6	0.17±0.03	0.17±0.13	0.23	0.79±0.05
H-PB3#3	20.0	2.1	3.2±0.2	14±4.6	0.16±0.01	0.68±0.24	0.24	0.74±0.05
D-PZ1#1	3.0	1.8	7.0±0.2	6.8±1.3	2.33±0.05	2.27±0.43	1.08	2.4±0.05
H-PZ2#1	3.0	2.3	3.6±0.1	(-5.1±1.4)	1.20±0.02	(-1.70±0.47)	1.00	1.3±0.02
D-PZ3#1	3.0	1.9	6.4±0.2	6.2±1.4	2.13±0.05	2.07±0.47	1.08	2.2±0.05
H-PZ4#1	3.0	3.6	4.8±0.1	1.9±1.4	1.60±0.02	0.63±0.47	0.86	2.1±0.03
D-PZ5#1	3.0	2.0	7.1±0.2	1.3±1.4	2.38±0.03	0.42±0.45	1.04	2.5±0.03
H-PZ6#1	3.0	5.9	7.1±0.1	(-0.2±1.4)	2.36±0.02	(-0.08±0.48)	1.34	1.9±0.02
Averagefor PZ		(D)	6.9±0.4	4.8±3.0	2.3±0.1	1.6±1.0	1.1±0.0	2.4±0.2
		(H)	5.2±1.8	(-1.1±3.6)	1.7±0.6	(-0.4±1.2)	1.1±0.3	1.8±0.4

simultaneously with D-PZ(2n-1)#1, where n = 1, 2, and 3. The A_1 subsystem was used for D-PZ1#1, D-PZ3#1 and H-PZ6#1. In all runs, the PZ sample used was 10 g, and the baking temperature was 570 K for 3 h. The output energy in the 2nd phase is the power integrated over 1,600 min. Examples of the evolution of the output power and the pressure for runs D-PZ1#1 and H-PZ2#1 are shown in Fig.8.

We notice the following four facts in the 1st phase: (1) very large output energies that are more than 3 times greater than those for the Pd-black samples, (2) very large D/Pd (H/PD) ratios of 1.1 ±0.0 (1.1 ±0.3) that are even higher than those for the PB samples, (3) surprisingly large E_{1st} = (2.4 ±0.2) eV (D) and (1.8 ±0.4) eV (H) on the average, and (4) larger isotope effect in E_{1st} compared with those for 0.1-μmϕ powder and Pd-black; the difference just exceeds the error range determined from standard deviations.

In two runs using H_2, we have negative values for the

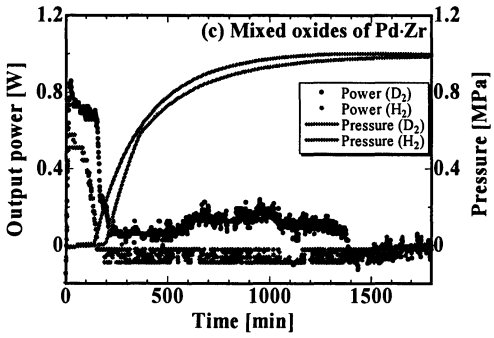

Fig.8. Evolution of heat and pressure in the vessel after introduction of D_2 gas (blue/light blue) or H_2 gas (red/pink) to Pd-Zr oxide compounds (D-PZ1#1 and H-PZ2#1). Heat-power level by D is larger than that by H in the 1st phase and also in the 2nd phase.

specific output energy in the rather stable 2nd phase. This should be considered to be due to slight shift in the zero point of the thermocouple signal.

Finally, it should be mentioned that we observed nothing other than steady background in the neutron counter and the scintillation probe located just outside the outer chambers.

More discussions and conclusions on results and underlying physics are given in our succeeding paper[12] in this Proceedings.

References

1) Y. Arata and Y. Zhang: The special report on research project for creation of new energy, J. High Temperature Society, 2008, No. 1.

2) Y. Arata, and Y. Zhang: *Condensed Matter Nuclear Science, Proc. 12th Int. Conf. on Cold Fusion* (ed. A. Takahashi, Y. Iwamura, and K. Ota, World Scientific, 2006) pp.44-54.

3) V. A. Kirkinskii, A. I. Kumelnikov: *Proc. ICCF13, Sochi, 2007* (Publisher Center MATI, Moscow, ISBN 978-5-93271-428-7) pp.43-46.

4) J. P. Biberian and N. Armanet: ibid. pp.170-180.

5) T. Nohmi, Y. Sasaki, T. Yamaguchi, A. Taniike, A. Kitamura, A. Takahashi, R. Seto, and Y. Fujita: http://www.ler-canr.org; to be published in Proc. 14th Int. Conf. Condensed Matter Nuclear Science (ICCF14), Washington DC, 2008.

6) *Hydrogen in Metals II -Topics in Applied Physics*, 29, ed. G. Alefeld and J. Voelkl (Springer, 1978).

7) A. Koiwai, A. Itoh, and T. Hioki: Japan Patent 2005-21860 (P2005-21860A).

8) C. P. Chang, *et al.*: Int. J. Hydrogen Energy, 16 (1991) 491.

9) M. M. Antonova: *Sboistva Gidriedov Metallov* (Properties of Metal-hydrides) (Naukova Dumka, Kiev, 1975; translated by NissoTsushinsha, Wakayama, 1976) [in Japanese].

10) Y. Fukai, K. Tanaka, and H. Uchida: *Hydrogen and Metals* (Uchida Rokakuho, Tokyo, 1998) [in Japanese].

11) H. Fujita: J. High Temperature Society 24 (1998) 272.

12) A. Takahashi, A. Kitamura, T. Nohmi, Y. Sasaki, Y. Miyoshi, A.Taniike, R. Seto, and Y. Fujita: Deuterium Gas Charging Experiments with Pd Powders for Excess Heat Evolution, (II) Discussions on Experimental Results and Underlying Physics, this Proceedings

Proceedings of JCF9, March 28-29, 2009, Shizuoka-ken Sangyo Keizai Kaikan, Shizuoka, Japan

Deuterium Gas Charging Experiments with Pd Powders for Excess Heat Evolution (II) Discussions on Experimental Results and Underlying Physics

A.Takahashi[1*], A. Kitamura[2], T. Nohmi[2], Y. Sasaki[2],
Y. Miyoshi[2], A. Taniike[2], R. Seto[1], and Y. Fujita[1]
[1]Technova Inc. *akito@sutv.zaq.ne.jp
[2](Division of Marine Engineering, Graduate School of Maritime Sciences, Kobe University)

Experimental results obtained for Pd/PdO/ZrO_2 nano-composite samples are summarized and the underlying physics is discussed. Arata-Zhang's May 2008 excess heat result was replicated quantitatively. Using Pd/PdO/ZrO_2 powders (produced by Santoku Co., Kobe Japan), we obtained: 1) D-gas charge in the first phase (zero pressure interval) gave 20~90% excess heat than H-gas charge. 2) In the second phase of pressure rise, significant excess heat (about 2 kJ/g-Pd) for D-gas charge was observed, while near zero level excess heat for H-gas charge was observed. We discuss the underlying surface and nano-particle physics in views of the enhanced surface adsorption potential by fractal sub-nano-scale trapping points on nano-Pd particle, the diffusion to inner shallower Bloch potential of regular Pd lattice, and the drastic mesoscopic and isotopic effect of surface and lattice rearrangement of nano-Pd particle by full D(H)-absorption to make deeper D(H) trapping potentials of surface adsorption (about 2 eV for D) and intermediate surface state trapping.

1. Introduction

The aim of this research, the experimental apparatus, experimental procedure and observed results with deuterium and protium gas charging experiments with various nano-fabricated Pd powders are described in our other two papers in this proceedings[1]. The Pd/PdO/ZrO_2 nano-composite samples (about 10 nm diameter Pd particles dispersed in about 7 micron size ZrO_2 flakes) produced very interesting performance with deuterium (D) versus protium (H) absorption and exothermic energy generation.

We discuss our results with 100 nm Pd particle powders and Pd-black powder, and compare our results to the Arata-Zhang work[2]. Our results with nano-Pd/ZrO_2 samples are interesting because specific surface effects in adsorption and following absorption into inner "lattice" sites appears to be taking place, resulting in anomalously large stoichiometry values (x>1) of PdDx and deep trapping potential (or released energy). Compared with the 100 nm Pd particle-powders, 10 nm Pd particles dispersed in ZrO_2 are showed drastic mesoscopic effects with isotopic difference.

2. Trend of Heat-Power Evolution

The evolution of heat and gas-pressure can be evaluated for two phases: the first phase and the second phase, as we show in typical data (Fig. 1).

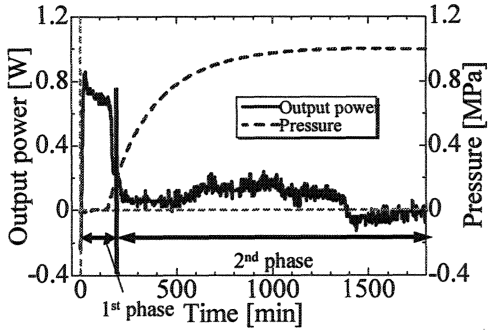

Fig. 1: Typical heat (power) evolution data with Pd/ZrO_2 nano-composite sample with D-gas charge (D-PZ1#1 run)

The first phase is defined as the time-interval where reaction chamber (cell) keeps nominal "zero" gas-pressure. This means almost all D(H)-gas entering the cell is absorbed by the nano-Pd powder. Heat (power) evolution curve in the first phase may be regarded mostly as the normal chemical heat of formation during D(H)-gas absorption into nano-Pd powders. However, there may also be an anomalous nuclear-reaction component to this heat, that we discuss later.

The trend of heat-power evolution in the second phase is very isotope dependent, as shown in typical data in Fig. 2.

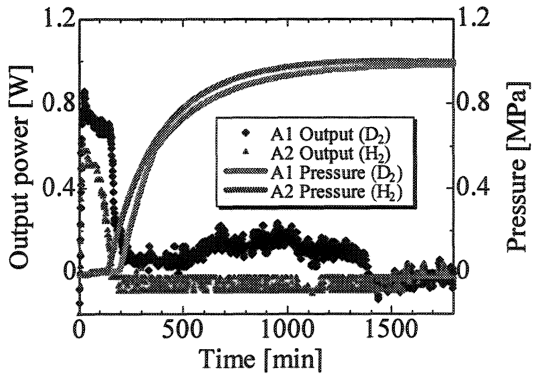

Fig. 2: Typical "excess heat-power" evolution by D-charge for Pd/ZrO2 sample (D-PZ1#1run), compared with "zero-excess" power level by H-gas charge (H-PZ2#1 run)

The H-gas charge have given "zero" power level (sometimes negative integrated values according to zero-level drift of calorimetry) in the second phase. Obviously, the D-gas charge to $Pd/PdO/ZrO_2$ nano-composite sample produced much more heat than the H-gas charge, for both phases.

3. Results and Discussions for First Phase Data

We summarize the integrated data of D(H)/Pd ratios, Heat per one-gram-Pd, Energy per D(H) atom absorption and gas-flow rates in **Table 1 (see end of text).**

First we discuss the data for 100 nm Pd-particle powders (D-PP and H-PP runs in Table 1). Loading ratios, D(H)/Pd, are 0.43 and 0.44 respectively for deuterium (D) and protium (H) gas charging. Specific energies per absorbed D (or H) atom E_{1st} (or ΔH_s) values are 0.24 eV/atom-D and 0.20 eV/atom-H. When D(H) is absorbed in metal lattice, surface adsorption traps D(H) molecule (or atom) first and diffuse into inner lattice sites (O-sites of Pd, usually) gradually. Fig. 3 illustrates typical form of surface trapping potential and inner periodical (Bloch) trapping potentials.

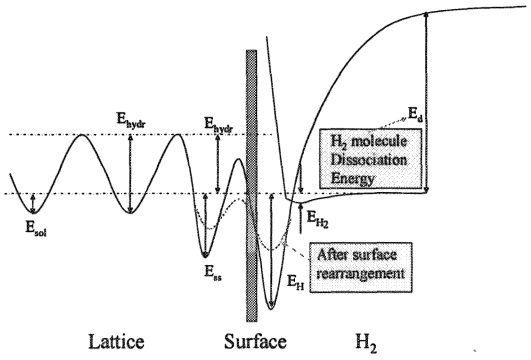

Fig. 3: Image of D(H) trapping potentials at surface adsorption (depth E_H) and lattice absorption (depth E_{hydr}); trapped D(H) atom diffuses gradually into inner Bloch trapping potentials through the QM tunneling. After full loading (x=1 for PdDx), rearrangement of Pd lattice may happen to make shallower potentials.

For known, textbook values[3], E_H is about 0.5 eV and

E_{sol} is 0.23 eV. The difference, E_H-E_{sol}, becomes the energy released per D(H)-atom absorption in lattice and is about 0.25 eV for bulk Pd lattice.

The observed E_{1st} (ΔH_s) values for 100 nm Pd particle powder are near to this value of bulk Pd metal. This means that 100 nm Pd particle works as bulk-metal for D(H) absorption.

We will see E_{1st} values for Pd-black and $Pd/PdO/ZrO_2$ nano-composite samples will have given much larger energies (deeper trapping potentials) to show the drastic mesoscopic effects.

Next, we look integrated data for Pd-black samples (D-PB and H-PB runs) in Table 1. E_{1st} values in averages of runs are 0.70 ± 0.15 eV/atom-D and $0.69\pm$ 0.10 eV/atom-H. These values are significantly higher than the bulk value about 0.25 eV. For the virgin runs (#1 runs), significantly high loading at $PdD_{0.88}$ or $PdH_{0.79}$ were observed. However, for runs with used samples (#2, #3, #4 runs), loading ratios were as small as 0.23 in average. Nevertheless the specific E_{1st} values were observed as same as the virgin (#1) runs. This fact means that microscopic active adsorption sites on surface of used Pd-black are working in the same way as the virgin Pd-black sample, although effective area of active surface decreased to 1/3 or less.

We made SEM observation for Pd-black samples of "before" and "after" usage[1]. We found the used Pd-black sample powders clumped together to be bigger sizes (about 10 times) than the virgin one and "fractal" nano-structures on surface of virgin Pd-black samples were flattened. We observed excess heat-like event in local time interval of the first phase data for virgin Pd-black and positive excess heat in the second phase, while heat-power level dropped drastically for the used Pd-black runs (#2 run and later runs). We understand that Pd-black has good nano-structure for making anomalous "CMNS effect", but the clumping-together effect by absorbing D(H) makes the CMNS effect disable. To overcome this, we need to avoid the clumping-together effect. The clumping-together effect is not sintering, because we did not observe the clumping-together by baking Pd-black powders up to 300 deg C before #1 run.

The idea by Arata-Zhang group[2] is of dispersed Pd nano-particles (5 nm diameter) in ceramics as ZrO_2 flakes to block the clumping-together effect.

Now we discuss the integrated data in the first phases for $Pd/PdO/ZrO_2$ samples (D-PZ and H-PZ runs in Table 1). We observed heat-power levels were strongly dependent on the D(H) gas-flow rate. The larger gas-flow rate has trend to give larger excess heat level in the first phase, but the first phase ends earlier than it does with smaller flow rate. This is understood as the faster gas-flow saturates the D(H) powders more quickly. Therefore, to compare specific values of E_{1st} (released energy per D(H)-atom), D(H)/Pd (loading ratio) and heat (in kJ) per g-Pd, it is more appropriate to see the underlying physics.

Our first surprise is that for all measured loading ratios, the D(H)/Pd values for the first phases are greater than 1.0. In other words, overloading occurred (x=1.1 in average for PdD(H)x stoichiometry) in usual sense, even though the background gas pressure were nearly zero (near vacuum). This must be considered a drastic mesoscopic effect of D(H) absorption by the Pd nano-composite samples. For the known bulk Pd-metal, D(H) atoms are trapped in Bloch potentials (see Fig. 3) at O-sites for $x<1.0$. The observed anomalous data of $x>1.0$ should show that the additional trappings at T-sites happened by the mesoscopic effect (about 5000 Pd atoms existing in a 5 nm diameter particle).

The data for specific released energy E_{1st} values are

also anomalously large and isotope (D or H)-dependent. These are 2.2-2.5 eV/atom-D and 1.3-2.1 eV/atom-H. Deuterium gives larger E_{1st} values. These released energy values are 5-10 times of the conventional value 0.25 eV for bulk Pd metal. These values are however dependent on the gas-flow rate, and they call for further investigation. As the PZ samples gave drastic mesoscopic effects, compared to the 100 nm Pd powder, we need to do further studies by changing the nano-Pd particle size.

We measured the ratios of [heat/D]/[heat/H] in the first phases. We obtain ratios as 1.94 to 1.3 for the first and second PZ runs. The data we deduced from Arata-Zhang's first phase is about 1.3. We can say our data for the first phase quantitatively replicated the Arata-Zhang result, although Arata-Zhang used 5 nm diameter Pd nano-particles dispersed in ZrO_2 flakes and ours was 10 nm.

4. Excess Heat for the Second Phase

As summarized in Table 1, we observed positive excess heat in the second phase of the D-PZ series runs for virgin (first run) samples. We tested three pairs of samples with simultaneous runs with D-gas in cell A_1 (with the D-PZ5 in cell A_2) and H-gas in A_2 (with H-PZ6 in cell A_1). For the D-PZ5 run, the D-gas cylinder was exhausted in the second phase and the gas pressure decreased (because of a leak), so that excess heat phenomenon was not observed. For the earlier two PZ runs, we observed clear excess heat only for D-gas charging, 2.27 and 2.07 kJ/g-Pd in the time interval of 1600 minutes.

Arata-Zhang gave 29.2 kJ with 24.4 g Pd/ZrO_2 sample. Assuming their sample contained 7.7 g net Pd weight, we get 2.8 kJ/g-Pd for a 3000-minute time interval with higher D-gas pressure (10 MPa maximum), after correcting specific H-absorption energy E_{1st} value (about 1 eV/atom-H as we observed). We can say that our results for second phase heat was comparable to (or may have exceeded) Arata-Zhang's data, given that their data was for a duration about two times longer, with higher gas pressure.

In Fig. 5, we show the rather steady excess heat evolution for used $Pd/PdO/ZrO_2$ samples (D-PZ3#2 and H-PZ4#2 runs).

We obtained total excess heat of 3.3 kJ/g-Pd for 9000 minutes of D-gas charging and later evacuation.

Before the end of run, we observed significant excess heat evolution after the evacuation of the A_1 (D-gas) cell. The expanded data is shown in Fig.6.

We speculate that the so called "heat after death event" was observed in the gas-loading experiment. The degassing data after evacuation and baking clearly shows very interesting performance of the Santoku-sample: it retained 100 times more D-atoms after evacuation compared to the Pd-black. (See Fig. 4).

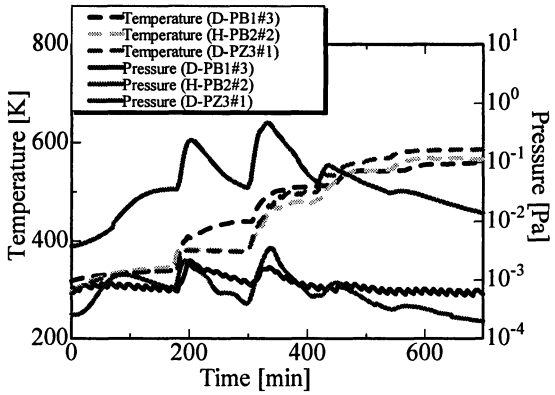

Fig. 4: De-gassing data for Santoku-sample compared with that for Pd-black; Santoku-sample retains 100 times D(H)-atoms by its very deep trapping potentials of the mesoscopic effect of dispersed Pd-nano particles

The heat after death event may take place by trapped

deuteron cluster (namely TSC-formation by Takahashi model[4]) at very deep (maybe about 2 eV for D absorbed PZ-sample) surface adsorption potentials, where deuterons from inner Bloch trapping potentials diffuse gradually to surface trapping points to form transient 4D/TSC cluster and makes 4D → ^{4}He+^{4}He+47.6M eV reactions[4] as a green nuclear energy source.

Lastly, we discuss possible chemical energy release by oxidation of charged D(H)-gas, because the samples contained PdO and ZrO_2 components. Figure 4 clearly shows that D(H)-gas was mostly absorbed by Pd in the PZ samples, since Pd-black gave same pattern of degassing.

It is unlikely that the ZrO_2 is making large contributions to these quantities. We have to consider the reduction of PdO_x followed by production of xD_2O (xH_2O) and PdD_y (PdH_y). The reaction energies Q_D and Q_H are evaluated to be $(162.6\times x + 70.0\times y)$ kJ and $(156.6\times x + 58.0\times y)$ kJ, respectively. For the assumed values of $x = 1 \sim 0$ and $y = 0 \sim 1$, Q_D and Q_H are 0.84 ~ 0.73 eV/D and 0.81 ~ 0.60 eV/H, respectively. These are too small to account for both the observed E_{1st} energies and the isotope effects.

There might be a yet-unknown atomic/electronic process governing the phenomenon in the present mesoscopic system, or the concept of "atom clusters" might apply. However, it seems rather difficult to imagine that such a large isotope effect only occurs in the electronic process of adsorption and/or hydride formation. Some nuclear process as suggested by the 4D/TSC model could be a candidate for the phenomenon.

5. Concluding Remarks

Arata-Zhang's Excess Heat Result was replicated quantitatively by our more precise heat and loading ratio measurements.

For Pd/PdO/ZrO_2 powders (Santoku-samples):

1) The D-gas charge in the first phase (zero pressure) gave 20-90% excess heat than the H-gas charge.

2) In the second phase, significant excess heat (about 2 kJ/g-Pd) for the D-gas charge, while zero level for the H-gas charge, was observed.

No increase of neutron counts was seen, neither increase of gamma-rays over natural backgrounds.

D(H)/Pd ratios in the end of first phase was x>1.0, namely over-loading (x=1.1 in average). Flow rate dependence of x-values should be investigated further.

Further experiments changing conditions will be fruitful for developing clean energy devices.

Nano-Pd dispersed sample (Santoku, Pd/ZrO_2) retained 100 times more D(H) atoms after evacuation, than the Pd-black case. The mesoscopic effect of Pd-nano-particles, namely surface and lattice rearrangement, probably makes deep D(H) trapping potentials (1.0-2.5 eV). We need to study D(H)-gas flow-rate dependence. Stable excess heat production is expected for #2 and later runs. We need further studies of this. We plan to conduct detection of nuclear products by the B-system.

Replication by other groups is important to confirm our results.

Funding

This is a joint research project of Kobe University and Technova Inc. for fiscal year 2008.

References:

1) Y. Sasaki, A. Kitamura, T. Nohmi, Y. Miyoshi, A. Taniike, A. Takahashi, R. Seto, and Y. Fujita; Deuterium Gas Charging Experiments with Pd

Powders for Excess Heat Evolution, (I) Results of absorption experiments using Pd powders, (this meeting)

2) Y. Arata and Y. Zhang: The special report on research project for creation of new energy, J. High Temperature Society, No. 1. 2008.

3) Y. Fukai, K. Tanaka, Y. Uchida: Hydrogen and Metal (in Japanese), Uchida-Roukakuho Pub., Tokyo, ISBN=4-7536-5608-X (2002)

4) A. Takahashi: Cold Fusion 2008- Mechanism of Condensed Cluster Fusion (in Japanese), Kogakusha, ISBN=978-4-7775-1361-1 (2008)

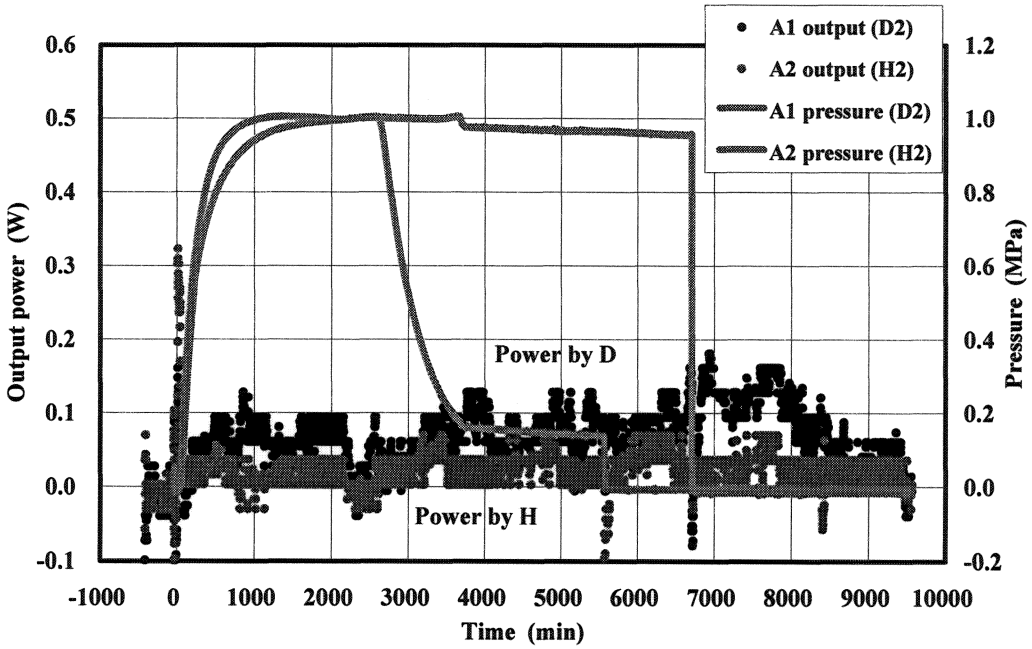

Fig. 5: Long lasing excess heat evolution from a previously used Pd/PdO/ZrO_2 sample

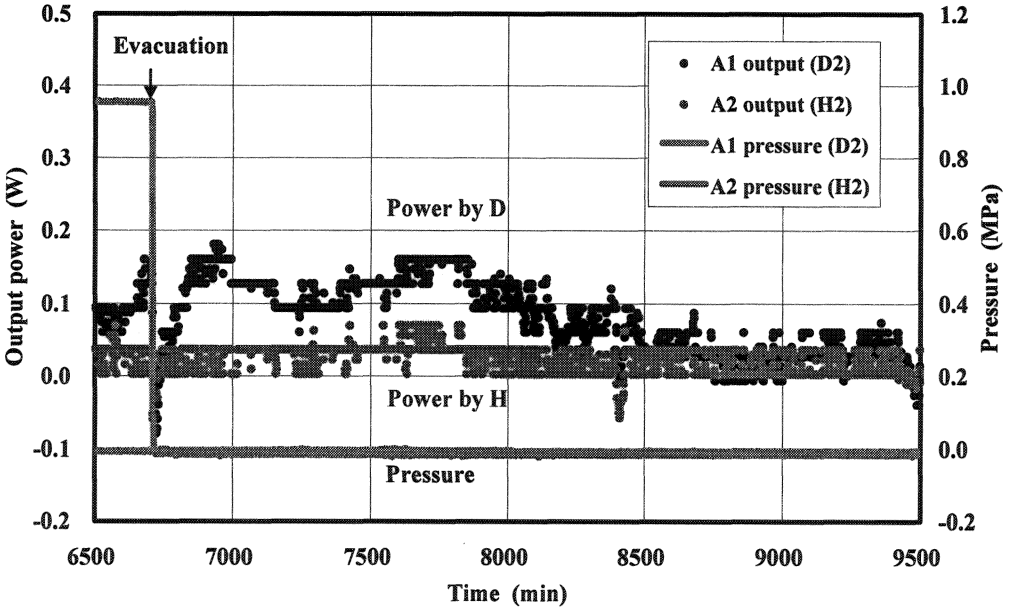

Fig. 6: "Heat after death" event observed after the evacuation of A_1 (D-gas) cell for D-PZ3#2 run

Table 1: Summary of Integrated Data for phase-1 and phase-2, comparing 100 nm Pd powder, Pd-black and Pd/Zr nano-composite samples.

Run number	weight of Pd [g]	Flow rate [sccm]	Output energy [kJ] 1st phase	Output energy [kJ] 2nd phase	Specific output energy [kJ/g] 1st phase	Specific output energy [kJ/g] 2nd phase	D/Pd or H/Pd (1st ph.)	E_{1st} [eV/D(H)]
D-PP1#1	5.0	2.7	0.5±0.4	2.5±4.1	0.10±0.07	0.52±0.83	0.43	0.26±0.14
D-PP1#2	5.0	3.8	0.5±0.2	4.0±4.4	0.10±0.05	0.79±0.88	0.44	0.25±0.09
H-PP2#1	5.0	5.4	0.4±0.2	2.6±3.9	0.0810.03	0.53±0.80	0.44	0.20±0.07
D-PB1#1	3.2	3.6	1.7±0.3	8.3±4.5	0.54±0.10	2.60±1.40	0.88	0.67±0.12
H-PB2#1	3.6	4.2	1.6±0.3	(-2.2±4.6)	0.45±0.08	(-0.62±1.30)	0.79	0.62±0.11
D-PB3#1	20.0	2.9	9.3±1.1	1.1±0.5	0.47±0.06	0.06±0.02	0.79	0.65±0.08
D-PB3#2	20.0	0.9	3.3±0.5	3.4±2.6	0.17±0.03	0.17±0.13	0.23	0.79±0.05
H-PB3#3	20.0	2.1	3.2±0.2	14±4.6	0.16±0.01	0.68±0.24	0.24	0.74±0.05
D-PZ#1	3.0	1.8	7.0±0.2	6.8±1.3	2.33±0.05	2.27±0.43	1.08	2.4±0.05
H-PZ2#1	3.0	2.3	3.6±0.1	(-5.1±1.4)	1.20±0.02	(-1.70±0.47)	1.00	1.3±0.02
D-PZ3#1	3.0	1.9	6.4±0.2	6.2±1.4	2.13±0.05	2.07±0.47	1.08	2.2±0.05
H-PZ4#l	3.0	3.6	4.8±0.1	1.9±1.4	1.60±0.02	0.63±0.47	0.86	2.1±0.03
D-PZ5#1	3.0	2.0	7.1±0.2	1.3±1.4	2.38±0.03	0.42±0.45	1.04	2.5±0.03
H-PZ6#1	3.0	5.9	7.1±0.1	(-0.2± 1.4)	2.36±0.02	(-0.08±0.48)	1.34	1.9±0.02
Average		(D)	6.9±0.4	4.8±3.0	2.3±0.1	1.6±1.0	1.1±0.0	2.4±0.2
for PZ		(H)	5.2±1.8	(-1.1±3.6)	1.7±0.6	(-0.4±1.2)	1.1±0.3	1.8±0.4

Proceedings of JCF9, March 28-29, 2009, Shizuoka-ken Sangyo Keizai Kaikan, Shizuoka, Japan

High Energy Charged Particle Detection During Gas Permeation Experiment Using A Newly Developed Detector System

Yu TORIYABE and Jirohta KASAGI

Laboratory of Nuclear Science, Tohoku University
Mikamine 1, Taihaku-ku, Sendai 982-0826, Japan
E-mail: toriyabe@lns.tohoku.ac.jp

A detector system with charged particle identification for high temperature gas permeation experiment was developed. We employed a phoswich scintillation counter which consists of a thin YAP(Ce) scintillator and a slower plastic scintillator, BC-444. Scintillation pulse signals were recorded by a digital storage oscilloscope to realize careful off-line analyses by using the pulse shape discrimination (PSD) technique. Moreover, the system has large plastic scintillators surrounding the reaction chamber: they serve as veto counters and reject cosmic ray events. Consequently, the system can identify energetic charged particles for emission rate as low as 3 counts/day. In a long period measurement of gas permeation through a Pd/CaO/Pd complex foil, a slight difference of counting rate between D_2 gas permeation and vacuum condition was observed in the high energy region. It is suggested that high energy charged particles, most probably α particles, are emitted during D_2 gas permeation.

1. Introduction

Anomalous nuclear reactions have been reported in a gas loading system such as electrical discharge, gas permeation, gas desorption and so on[1]. However, charged particle detection in such condition was seldom reported except measurements using a solid state track detector (CR-39)[2,3]. A high reliable Si semiconductor detector (SSD) cannot be applied in high temperature hydrogen atmosphere. Noise (leak current) is non-linearly increased with temperature rise, and it loses energy resolution. A silicon surface barrier detector (SSB) has a thin SiO_2 (p-type) layer on the surface. The layer is reduced in hydrogen atmosphere and results in an unstable operation. Although a detector made by ion implantation can avoid the reduction problem, a thin (less than 150 μm) ion implantation detector has never been commercially supplied because of technical problems. Therefore, a particle identification technique by ΔE – E telescope array cannot be employed for a several MeV α particle detection. (150 μm SSD stops ~ 20 MeV α particle.)

As we reported at JCF8[4], we have developed a new detector system with charged particle identification for gas permeation experiments[5]. This paper describes a present performance of the system and results of charged particle measurement during D_2 gas permeation through Pd complex samples.

2. Detector system

2.1. YAP(Ce) characteristics

We have considered and tested various scintillation materials, and finally selected Cerium doped Yttrium Aluminum Perovskite ($YAlO_3$) scintillator (YAP(Ce))[6,7] as the most preferred detector. The YAP(Ce) is mechanically and chemically stable and temperature dependence of light yield is within +2 ~ -8 between 290 and 460 K when we normalize the yield to 100 at 298 K as shown in Fig. 1. This characteristic is one of the best in well known scintillation materials.

However, energy resolution of commercial quality crystal is bad: FWHM for 5.5 MeV α particles is 21%. Furthermore, temperature dependence of decay constant is larger than that of the light yield. It decreases about 20% at room temperature region.

2.2. Phoswich detector

We have made a phoswich detector in order to reject unwanted events. Fig. 3 shows an illustration of the phoswich detector. Two different scintillation materials are connected to one photomultiplier tube (PMT). In this system, the first scintillator is YAP(Ce) whose decay constant is about 30 ns. The second one is a plastic scintillator, BC-444, which has about 300 ns decay constant.

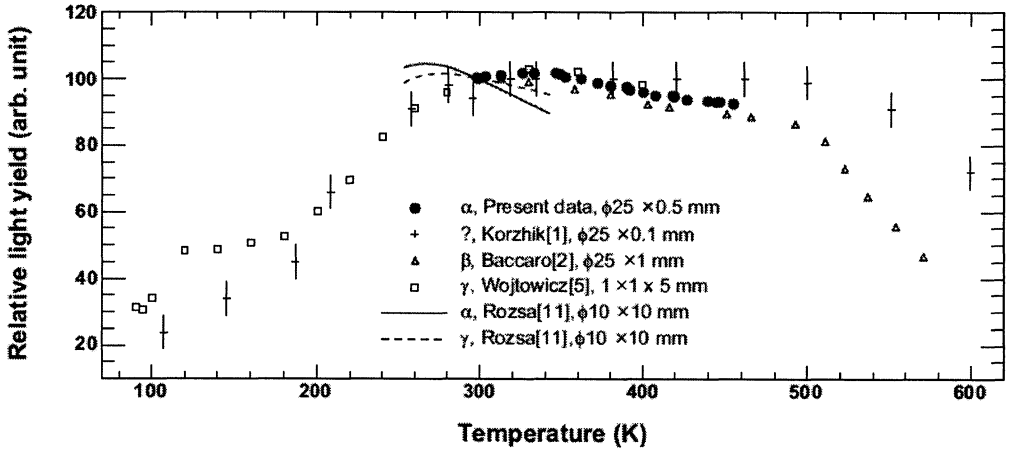

Figure 1. Temperature dependences of relative light yields of the YAP(Ce) in various conditions. All series of data are normalized to 100 at a standard temperature of 298 K. Closed circles show the present data.

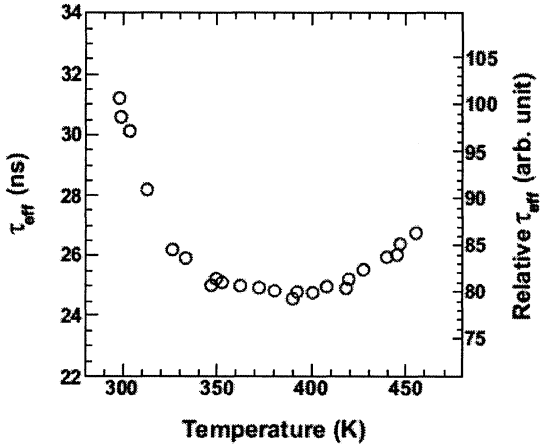

Figure 2. Temperature dependence of decay constant of YAP(Ce) excited by α-ray incidents. It decreases with a slope of -0.4% / K below 350 K.

We use 0.5 mm thickness YAP(Ce), which can stop 50-MeV α and 12-MeV proton. Charged particles emitted from the sample stop in the YAP(Ce) due to large energy loss of charged particles. Then an output pulse of PMT is originated only from YAP(Ce) scintillation.

On the other hand, cosmic rays or γ rays from natural radio isotopes, namely background events, can path through both scintillators. Thus, the output pulse consists of two components: YAP(Ce) and BC-444. We note that the output pulse of the background event has a longer tail caused by BC-444 and therefore we can discriminate the charged particle events (foreground: F.G.) from the background events (B.G.) by sorting out the decay time.

During operations we recorded all pulse shapes from the photomultiplier tube by a digital storage oscilloscope for precise off-line analyses. Record length is 1000 points / 1000 ns.

Energy calibration curve was obtained by 5.5 MeV α particle from spectroscopy grade ^{241}Am checking source and 8.8 MeV α from ^{228}Th.

2.3. VETO detectors

A permeation chamber equipped with the phoswich detector is placed is surrounded by large plastic detectors: VETO detector. If cosmic rays enter the main detector, the VETO detector would make a signal at the same time. We can reduce B.G. more by rejecting coincidence events between the phoswich and the VETO detector.

3. Experiment

The permeation experiment is carried out according to the procedure reported in Ref. 5. Pd foils with CaO/Pd multi layers were provided from MHI and Toyota Central R&D Labs., Inc. Cs was electrodeposited or Sr was ion implanted onto the surface of the multi layer side.

In the chamber, the multi-layer side was exposed to D_2 gas for about one week with the pressure of about 1.0 or 1.5 atm. D_2 gas permeated through the foil because the opposite side of the foil is in vacuum(~10^{-3} Pa under the permeation). Temperature of the sample can be

controlled by a ohmic heater at around 350K. Then a typical permeation rate is about 1 ccm.

After we performed the measurement with D_2 gas, we evacuated the chamber. The measurement without D_2 gas is the background one to be compared with the foreground.

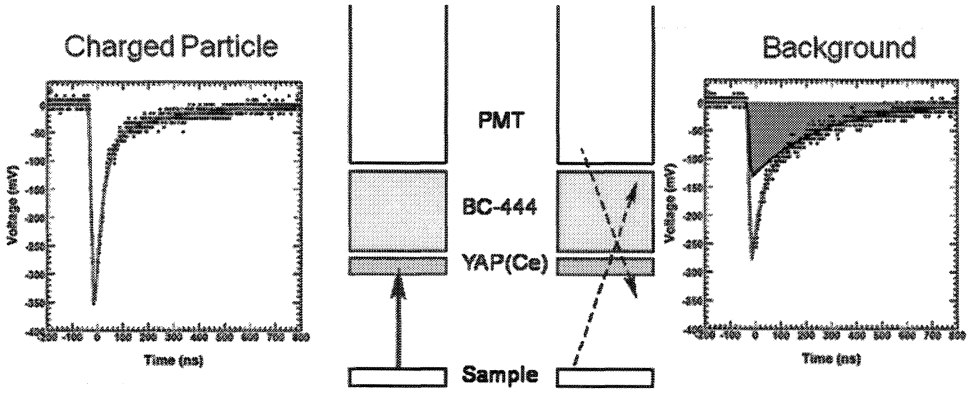

Figure 3. An illustration of a phoswich detector. A front scintillator is 0.5-mm thick YAP(Ce) and a back one is 5-mm thick BC-444 plastic. Decay constants of them are approximately 30 and 300 ns, respectively.

4. Results

After the permeation process, we carefully analyzed the off-line data. Cosmic rays and non-charged particles were rejected by information from VETO detector and PSD analysis, respectively.

Figure 4 shows total counts of charged particles during D_2, H_2 permeation and vacuum condition with Cs electrodeposited Pd complex sample provided by MHI. The horizontal axis shows equivalent energy of α particles.

Although counting rates for F.G. and B.G. are almost same below 10 MeV, the rate in D_2 gas condition is slightly larger than those in B.G. runs. Particular interest is events at around 25 MeV; this energy region is near the Q-value of the d(d, α) reaction, 23.8 MeV. However, a different MHI sample did not show such events. In this case, the permeation rate was very small, almost 0 ccm. We conjecture that small D_2 permeation rate cannot induce charged particle emissions.

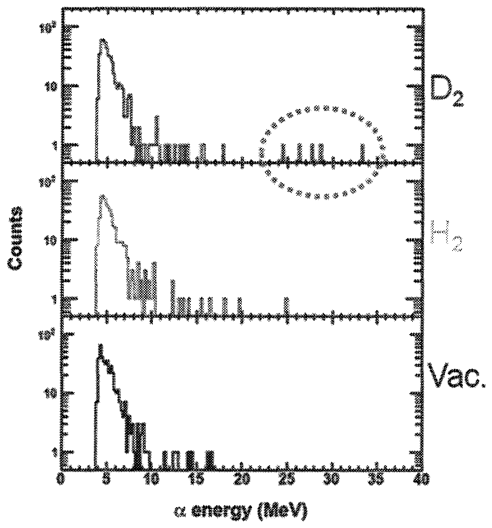

Figure 4. Number of charged particle counts during D_2(455 counts / 191.1 hours), H_2(444 / 168.4) permeation and vacuum(408 / 184.8) condition. The sample was Cs electrodeposited Pd complex provided by MHI.

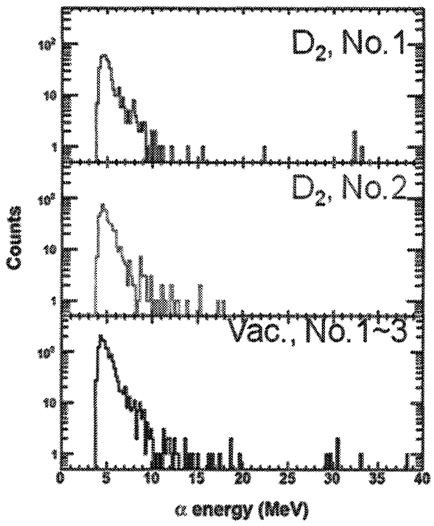

Figure 5. Number of charged particle counts during D_2 gas permeation for sample No. 1(682 counts / 188.7 hours) and No. 2(793 / 232.5), and vacuum(1959 / 684.7) condition for the samples provided by Toyota Lab. The vacuum condition shows the total counts for three samples.

We also measured particle emissions with three samples from Toyota lab. The samples are (1)50 μm-thick pure Pd foil, (2)100 μm-thick Pd with Sr implantation, (3)100 μm-thick Pd with Cs electrodeposition. Two of three samples (number 1 and 2) show higher counting rate at 5 – 10 MeV energy region as shown in Fig. 5.

We summarize the counting rate of the samples in Fig. 6 at the energy range of 5 – 10 and 10 – 40 MeV. Errors in Fig. 6 show one standard deviation.

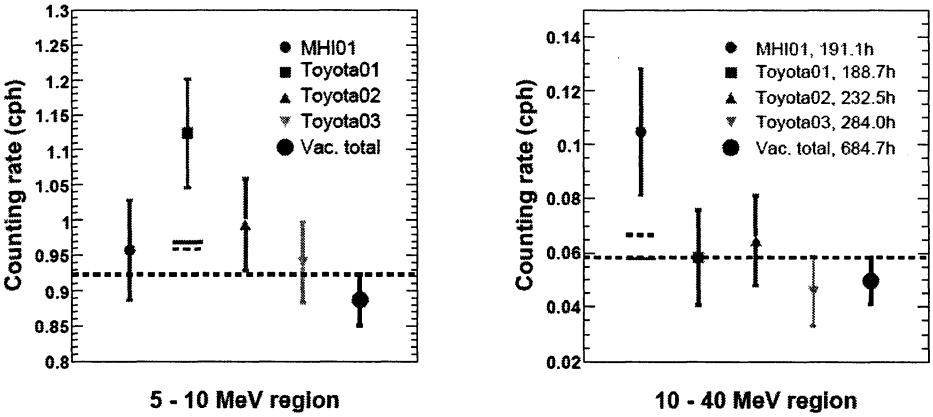

Figure 6. Counting rate of charged particle detection during D_2 gas permeation for some samples and vacuum condition. The vacuum condition shows the total counts for four samples. Errors show one standard deviation and we add 2σ lines for the case of Toyota01 in 5-10 MeV region and MHI01 in 10-40 MeV region.

The sample Toyota01 and 02 show larger counting rate at 5 – 10 MeV region. Especially, Toyota01 exceeds 2σ difference, which means charged particle emission is statistically reliable over 95 %. However, the PSD process has still problem for low energy analysis at present. The low energy pulse, namely small pulse, does not have enough intensity for numerical fitting of the decay time. Therefore discrimination of charged particles from B.G. becomes difficult.

In the case of MHI01, excess events appear in high energy, 10 – 40 MeV region. At this energy range, we can clearly separate the B.G. by the PSD analysis due to enough intensity. Therefore, this 1.5σ difference in the MHI01 case, implies only two possibilities, statistically fluctuation of background charged particles or real particle emissions caused by nuclear reactions in the samples. Here, the high energy counts were distributed around 25 MeV. This result would not deny the real particle emission possibility.

However, the difference, 1.5σ, is so small to conclude. Further study is required to establish a reliable result. At present we have not understood the origin of the high energy B.G. though we conjecture that elastic recoils d(μ, μ)d can possibly deposit high energy to the detector.

5. Conclusion

We developed a new charged particle detector system suitable for the gas permeation experiment. The main detector, YAP(Ce) is mechanically stable and temperature dependence of light yield can be negligible at the operation temperature ~ 350K. In order to reject unwanted events, we adopted YAP(Ce) / BC-444 phoswich detector. Pulse shapes of all events were saved by the digital storage oscilloscope and were analyzed precisely after the experiment. The PSD technique can clearly separate charged particle events from the B.G. Furthermore the system has large VETO detectors which can reject ~60% of cosmic-rays. Finally, the background rate is decreased to quite low level: 1.2 counts / day for E_α > 10 MeV. Therefore this system can identify 3 counts / day events for the clear evidence of nuclear reactions.

Using the detector system, we conducted gas permeation experiments with Pd complex. Significant difference between F.G. and B.G. (statistically reliable more than 95%) were

observed for $5 < E_\alpha < 10$ MeV with very high permeation rate for the thin and pure Pd. However the PSD analysis does not completely work at this region. At higher energy, the original sample supplied from MHI group shows 1.5σ difference. Especially, there are some events at near 25 MeV, which are candidate of monoenergetic alpha particles.

Because of low counting rate in foreground events we plan to improve the detector system to decrease B.G. And we also try to increase the foreground events to improve the material and permeation condition in further studies.

Acknowledgement

Pd complex samples were provided from Mitsubishi Heavy Industries, Ltd and Toyota Central R&D Labs., Inc. Authors would like to thank CMNS researchers at those laboratories.

This study is partially supported by JSPS grant.

References

1. A. Takahashi, *Proc. ICCF12*, 1, 2006.
2. R. A. Oriani and J. C. Fischer, *Jpn. J. Appl. Phys.*, **41**, 6180, 2002
3. P. Moisier-Boss *et al.*, *Eur. Phys. J. Appl. Phys.*, **40**, 293, 2007
4. Y. Toriyabe and J. Kasagi, *Proc. JCF8*, 20, 2007
5. Y. Iwamura *et al.*, *Jpn. J. Appl. Phys.*, **41**, 4642, 2002.
6. S. Baccaro *et al.*, *Nucl. Instr. & Meth. A*, **361**, 209, 1995.
7. M. Moszynski *et al.*, *Nucl. Instr. & Meth. A*, **404**, 157, 1998.

Proceedings of JCF9, March 28-29, 2009, Shizuoka-ken Sangyo Keizai Kaikan, Shizuoka, Japan

Heat Generation by Hydrogenation of Carbon Hydride

Tadahiko Mizuno, Hideo Kozima[1],

Laboratory of Electronic Materials Chemistry,Division of Material Chemistry, Graduate School of Engineering, Hokkaido University, Kita-ku Kita 13 Nishi 8, Sapporo 060-8628, Japan

[1]Cold Fusion Research Laboratory, 421-1202, Yatsu, Aoi, Shizuoka 421-1202, Japan

Summary

We observed anomalous heat generation during heating a small quantity of phenanthrene that was put in a cylinder with a Pt catalyzer and filled with high pressure hydrogen gas. It is very difficult to explain the total energy generation by a conventional mechanism of a chemical reaction. Because almost of all phenanthrene and hydrogen gas remained as it was after experiment. The heat generation sometimes reached to 0.1kW and continued for several hours. Moreover, we have confirmed γ ray emission at the same time. The correspondence between the heat generation and the gamma emission was not good but sometimes they showed good correlation. We have confirmed same result with high reproducibility by controlling the temperature and the pressure.

Introduction

We observed unusual reaction when hydrocarbon (a heavy oil fraction) was reacted under high pressure and high temperature with a metal catalyzer. It produces excess heat and weak radiation, specifically x-rays and gamma-rays. It is very difficult to explain the total energy generation by a conventional mechanism of a chemical reaction. Many studies concerning the hydrogenation of hydro-carbon have been performed for a long time [1-10]. We have motivated the idea of this reaction by following facts. Alkali hydride is made to react with the hydrogen gas at high temperature and high pressure. The hydride of Li is made at one atmosphere of hydrogen pressure in the reaction container made of the stainless steel at 725℃. LiH is made to react in melting Paraffin with hydrogen. NaH is made at high-pressure hydrogen to add the Phenanthrene and Anthracene in the mineral oil, and to distribute the sodium metal powder at 280℃. It has been reported that an extremely abnormal reaction in the process of such the hydrogenation. Such a report motivates us to vivificate the reaction.

Material and Methods

Figure 1 shows a schematic drawing for the measurement set up. Two types of reactor cylinders have been used in this study. The one is made from Inconel 625. Inconel reactor has 56mm outer diameter, 26mm inner diameter, 160mm height and the volume is 0.1l. The other one is made from SUS316L, 15mm outer

diameter, 9mm inner diameter and 300mm height with 0.02l capacity. The inconel cylinder can sustain 500 atm of pressure, while the SUS one is limited under 200 atm. Both can be heated up 850°C. The reactor is set in an electric furnace. It has hydrogen inlet, gas outlet and housing for a sensor of internal temperature measurement. Moreover, a thermo-couple for the measurement of the temperature of the outside wall of the reactor cylinder has been inserted between reactor walls and the inner wall of the heater.

The reactor is put in the heater. And there is an electric power supply described in right bottom of the graph, data logger and a recorder is set on them. After the metal catalyzer is put in the reactor, 1g weight of phenanthrene is put in and the cover is closed. And then, the reactor is evacuated to 10^{-3}mmHg with a vacuum pump. The hydrogen gas is supplied from the gas cylinder of 150atm pressures up to a constant pressure through a pressure regulator.

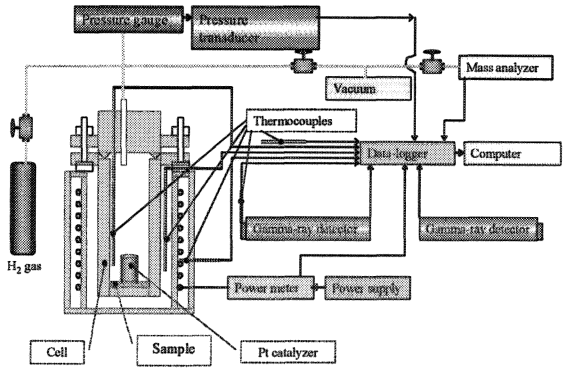

Fig.1: Schematic drawing for the measurement set up.

The electric furnace is supplied by a regulated electric power of 2-kW power supply. Temperatures of the space between the reactor and the furnace, and the inside of the reactor are continuously measured by R-type of sheath thermocouples. The temperature resolution of estimation through the system is 0.1degree.

Gamma-ray emissions are detected by a γ-ray detector (Aloka TCS-161) that is located 15 cm from the reactor. Its output is recorded continuously by the computer through a digital multimeter (Advantest, TR-6845). Temperatures of the furnace heater wire, of the inside of the reactor, of the outer reactor wall, of the surface of the gamma-ray detector, and of the room are also recorded by the computer through the multimeter. The mass spectrometer used in this study (ULVAC REGA201) can detect mass numbers up to 400.

Results and Discussion

We can estimate anomalous heat caused from the calibration curve obtained from the relationship between input power and the stable temperature of the reactor cylinder. We obtained the relationship between heater input and these temperatures to change the conditions of the sample presence, hydrogen pressure and the reactor. The temperature deviations stay in ±3°C if the hydrogen gas pressure increased from 1 to 100atm. It can be understand that the heat release caused by gas in the reactor is not noticeable when the case of inconel reactor.

Figure 2 shows an example of anomalous excess heat. In this test, 1g of phenanthrene was exposed to a mixture of 1 atm of hydrogen and 70 atm of helium gas. Heater power is initially set for 1.4kW, then after 3ks it is reduced to 700W. Finally, it is reduced to 640W. The

heater temperature (T_2) rises faster than the cell temperature (T_1). At 10ks they both stabilize at around 640°C, which is where the calibration curve predicts they will settle if there is no anomalous heat. However, they both soon begin to rise above the calibration point. At 9ks the cell temperature T_1 stabilizes for about 2ks as the heater temperature continues to rise. Then the cell temperature begins rising again and at 12ks it exceeds the heater temperature T_2. This temperature reversal is definitive proof that heat is being produced inside the cell. When power is turned off, at 16ks, the heater temperature T_2 peaks at 670°C and the cell temperature T_1 has reached 690°C, 20°C higher than T_2. Input heater power is 640W. The temperature at T_2 peaks at 670°C which is only as high as the calibrated point for this power level; it does not indicate any excess heat. Total energy is even more difficult to estimate than power, but given that the excess power persisted for 6ks (100min) it was at least 120kJ, for this test. Other tests have produced more energy.

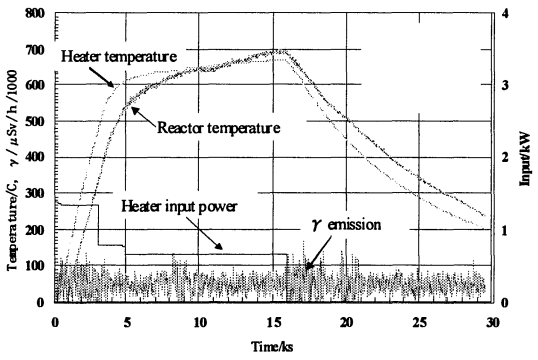

Fig. 2: An example of anomalous excess heat.

Figure3 shows the intensity distribution of gamma emission with the ionization chamber type detector. There are two peaks are shown at 0.11μSv/h and at 0.05μSv/h of the background by a peak analysis. Gamma emission stronger than the background is admitted when an excess heat had generated. Generation of heat was confirmed in the inconel reactor as above described. It has been understood that there was the generation of γ emission from these results. However, the temperature was measured by only a part of inside the reactor having large volume as 0.1l. It can not be understood where in the system the heat generation has occurred. We took the correspondence of the temperature and the Gamma emission with a small reactor. As for the measurement that uses the SUS reactor, the inside diameter is small as 9mm, and we puts the sample and the platinum catalyst in the bottom in the reactor, the thermo-couple touched the catalyst directly, then we can promptly measure the temperature. Thus, the correspondence of the γ emission and the temperature change can be seen directly.

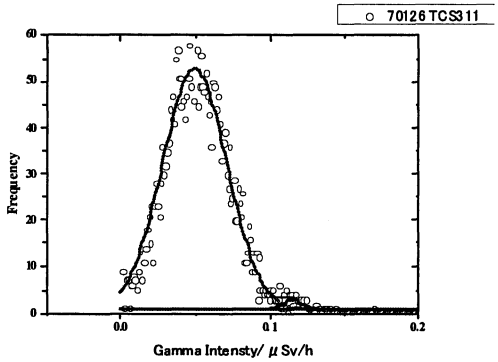

Fig.3: Intensity spectrum for the foreground γ emission in fig2.

Figure 4 shows the measurement result in the SUS reactor. This shows the temperatures and

the gamma emission that 1g of sample is heated with the platinum catalyst at 50atm H_2 pressure. The interval between each point showed the data collection is 5s. The heater input was 55W, and then the preset temperature was 595°C. The figure is shown the first 30ks-82ks interval.

It is understood that the reactor and the wall temperatures rose gradually though the initial temperature setting was 595°C. Moreover, it is understood that the temperature in the reactor, in this case, goes up previously, and the outside wall of the reactor goes up afterwards. Meanwhile, heater temperature has exceeded 700°C though that is not shown here. Moreover, it is understood that the temperature change in the reactor is extremely large.

It can be seen that the temperature rises rapidly after the emission of γ ray occurs. Especially, a strong γ emission corresponds to the rise of the heat. It is also admitted to correspond to the rise of the temperature at a weaker γ ray emission. Here, it shows rapid temperature change because the temperature returns to the preset temperature of 600°C again even if the temperature of the reactor goes up temporarily.

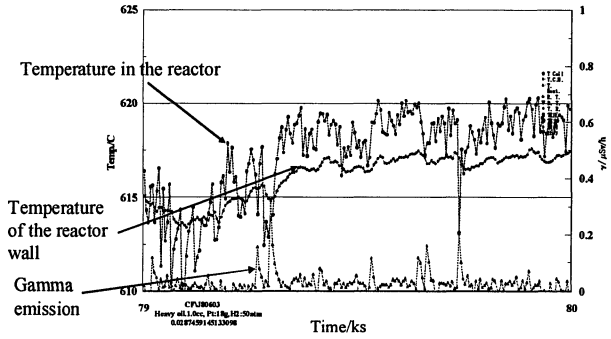

Fig. 4 : Gamma emission at the onset of anomalous heat.

Moreover, the following result was obtained by the ICP Mass analysis. In the analysis result of the solid was 99% ^{12}C in the carbon of the sample before experiment, and 50% or more was $^{13}C^{+}$ in the sample after experiment that excess heat had been occurred. Usually the reaction of hydrogenation of carbon hydride is exothermic, and heat is released corresponding to the ΔE. For example, ΔE is around -125 kJ/mole. But the enthalpy of the hydrogenation reaction of Phenanthrene is different depending on the temperature. It is a reaction of heat generation less than 300℃[11]. However, it is an endothermic reaction as kJ/mol at higher than 300℃. We observed the weight loss due to the reaction of phenanthrene in the high pressure of H_2 gas was under 0.01g. So, the molar of the phenanthrene was only 5.6×10^{-5}. Then the typical heat can be estimated as 11.2J. On the other hand, total heat observed was the order of 100 kJ; the heat was 10^4 times higher comparing with the calculation. Therefore, generation of heat is thought for the possibility of causing by the chemical reaction not to exist. In addition, the γ emission was observed during the experiment. It is shown that there was a generation of a certain kind of nuclear reaction through the correlation of the heat generation and the γ emission.

References

1. Chunshan Song and Andred D. Schmitz, Energy & Fuels, 11(1997) 656-661.

2. Elzbieta Fedorynska and Piotr Winiarek, , Reaction Kinetics and Catalysis Letters 63 (2) (1998) 235-239.

3. John R. Durland and Homer Adkins, J. Am. Chem. Soc., 59 (1937) 135-137.
4. Alfred Burger and Erich Mosettig, J. Am. Chem. Soc., 58 (1936) 1857-1860.
5. Weihua. Qian, Yosuke Yoda, Yoshiki Hirai, A. Ishihara and T. Kabe, Appl. Catal., A: General 184 (1999) 81-88.
6. Behzad Mahdavi, Jean Marc Chapuzet and Jean Lessard, Electrochim. Acta 38 (1993) 1377-1380.
7. Behzad Mahdavi, P. Los, M. Jean Lessard and Jean Lessard. Can. J. Chem. 72 (1994) 2268-2277.
8. Jean Mark Chapuzet, Behzad Mahdavi and Jean Lessard., J. Chim. Phys. 93 (1996) 1252-1261.
9. Behzad Mahdavi, Jean Marc Chapuzet, M. Jean Lessard and Jean Lessard, 76th CSC Conference, Sherbrooke, May 30-June 3, 1993.
10. Richard Menini, Anna Martel, Hugues Ménard, Jean Lessard and Olivier Vittori, Electrochim. Acta, 43 (1998) 1697-1703.
11. Wendell H. Wiser and Alex G. Oblad, Progress Report No. 2, (Covering the period January 1 – March 31, 1993) April 1993.

Proceedings of JCF9, March 28-29, 2009, Shizuoka-ken Sangyo Keizai Kaikan, Shizuoka, Japan

PRODUCING ELEMENTS OF MASS NUMBER 137 AND 141 BY DEUTERIUM PERMEATION IN DOUBLE MULTI-LAYERED Pd SAMPLES WITH Cs DEPOSITION

H. YAMADA, S. NARITA, K. IIDA, H. OHATA, S. SATO and H. NANAO*

Department of Electrical and Electronic Engineering, Iwate University, Ueda 4-3-5, Morioka, 020-8551 Japan *yamadahi@iwate-u.ac.jp*

*Department of Chemical Engineering, Iwate University, Ueda 4-3-5, Morioka, 020-8551 Japan

Abstract: Elemental analysis on Pd samples including double multi-layered Pd samples was performed after deuterium permeation experiment using TOF-SIMS. The TOF-SIMS has provided the anomalous count peaks at 135 and 137 u in spectra after deuterium permeation at 70℃, only when the multilayered Pd sample with a small amount of Cs was used. The substance with mass number 137 was effectively produced between the double multi-layered Pd samples. The substance could be ^{137}La, ^{137}Ba or ^{137}Cs produced during deuterium permeation by some nuclear transmutation occurring on/in the uppermost layer of the multi-layered Pd sample.

Keywords: Multi-layered Pd sample, Deuterium permeation, Transmutation, TOF-SIMS, Low energy nuclear reaction

1. Introduction

The experiment on nuclear transmutation from a selected element into another one around room temperature is of interest to provide important data for constructing a standard model of low energy nuclear reaction. Among several experiment methods for the transmutation, the gas permeation method is one of the promising methods. Iwamura et al. have studied using this method with Pd film complexes and have reported a low energy nuclear transmutation from Cs into Pr and from Sr into Mo on the surface of sample [1]. They used five-fold stack of Pd/CaO layers on a base bulk Pd foil in their experiment. Kitamura et al. have investigated the similar transmutation from Sr into Mo and have revealed that the transmutation also takes place between the thin layer and the base Pd foil.[2]

We have taken advantage of these gas permeation methods to perform the transmutation from Cs into Pr using samples with monolayer of Pd/CaO deposited on the Pd bulk [3-5]. We have not observed marked amount of Pr but detected a small amount of substance with mass 137 using TOF-SIMS. This series of tests have presented a strong suggestion that the substance of mass 137 formed during the D_2 gas permeation through the multi-layered Pd sample was a newly produced element.

The aforementioned suggestion and the result of experiment by Kitamura et al. have introduced us to use a sandwich-type combined sample consisting of two multi-layered Pd samples. The element Cs between the two multi-layered Pd samples was expected to transform effectively to another element in this study.

2. Experimental

The experimental method and setup to investigate the transmutation of Cs into other elements of larger mass number are basically the same as before.[3-5] We have used only single multi-layered Pd sample in previous studies. In addition to the single Pd sample, we used double multi-layered Pd samples in the present study. The double multi-layered Pd samples were formed as the combined samples as shown in Fig. 1. Two similar sheets of Pd bulk with the Pd/CaO layer(s) on the top were faced to each other, and made closely contacted with each other. Each multi-layered sheet consisted of several piles of thin layers and a base Pd foil of $0.1 \times 12.5 \times 12.5$ mm in size. The thin layers consisted of single- or five-fold stack of CaO and Pd thin layers, which were formed on the Pd foil by Ar ion beam sputtering of CaO followed by that of Pd. Each thickness of CaO

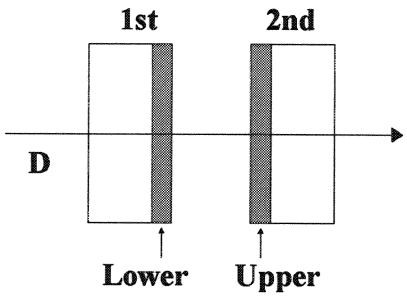

Fig. 1 Combined Pd sample.

and Pd layers were 2 and 18 nm, respectively. Only the thickness of the uppermost Pd layer was 40-50 nm.

After forming the thin layers on the base Pd foil, small amount of Cs was deposited on one of the surface of the uppermost Pd layers by an electrochemical method; the small amount of Cs was sandwiched between the two Pd sheets. A combined sample consisting of a Pd sheet with a single-fold Pd/CaO layer and a plain Pd foil was also used. No deuterium gas was loaded to the samples before deuterium permeation experiment. The chamber was usually filled with N_2 gas, when it is not used for experiments.

Just before the permeation experiment, the combined sample was set into the sample holder in an air environment and it was placed in the vacuum chamber. Then, the chamber was filled with deuterium gas at a pressure 0.2 MPa. The other side of combined sample was evacuated by a turbo molecular pump. The deuterium permeated from the chamber through the combined sample to the evacuated side by the pressure gradient for about 2 weeks. A heater was employed to keep the temperature of the chamber at 70℃ during the experiment.

After the permeation experiment, the heater is turned off and the chamber was filled with N_2 gas, then the sample was taken out from the holder. The Cs-deposited surface of the sample and the surface facing to it were analyzed by TOF-SIMS (ULVAC-PHI: TFS-2100). The primary ion in TOF-SIMS was Ga^+ and we measured at least three randomly selected areas of 40×40 μ m square. The spectra were obtained before and after a sputter cleaning of the uppermost surfaces of samples by the Ga^+ for 5-10 sec. In order to take into account the contamination from the environment, we prepared the control sample without exposure to deuterium gas flow, which was prepared by the same procedure as the permeation samples. We used 6 combined samples and 2 single Pd samples in this study, as shown in Table 1.

3. Result and Discussion

The anomalous peak was observed not only on Cs deposited surface but also on the opposite surface to the deposited one. A TOF-SIMS spectrum in a mass range of 132 – 142 u after sputter cleaning for a combined sample with a single-fold Pd/CaO layer is presented in Fig. 2, where an area on the opposite surface to the Cs deposited one was analyzed. The schematic view of cross-section of a combined sample is shown in this figure. A small peak of Cs is seen at 133 u in Fig 2, indicating a transfer of Cs from the deposited surface to the opposite one. Note that the isotopic abundance of ^{133}Cs is 100%.

Anomalous peaks are seen at 135 and 137 u in Fig. 2, where the count intensity of the former was lower than that of the latter. However, the peak intensity at 137 u has been sometimes observed to be slightly lower than that at 135 u [5]. These peaks were not observed for control samples. The calibrated mass obtained by the TOF-SIMS for the substance with mass number 135, the real mass of ^{135}Ba and CsD are 134.9092, 134.9057 and 134.9195 u, respectively. Accordingly the mass of the substance is 3.5 mu larger than that of ^{135}Ba and 10.3 mu smaller than CsD. Taking account of the former relatively small difference, one of the candidates for the substance could be ^{135}Ba.

Similar positive results of detecting substance with mass 137 was obtained in 5 cases out of total 8 cases, which are given in Table 1 as circled numbers ①－⑦. Cross mark (X) in the table means negative result for detecting anomalous substance with mass number 137. Since the number of runs for each test condition was only one in the present study, the negative results under the condition with the cross mark should not be

Table 1 Sample formation and position of deposited Cs on the surface of sample for deuterium permeation test.

	Films		^{133}Cs	Peak at M137	
	1st Lower	2nd Upper		1st, Lower	2nd, Upper
Single	Non	CaO 2 nm×5 Pd 18 nm×4 Pd 40 nm×1	2nd, Upper		①
	CaO 2 nm×5 Pd 18 nm×4 Pd 40 nm×1	Non	1st, Lower	×	
Double	CaO 2 nm×5 Pd 18 nm×4 Pd 40 nm×1	Pd foil	2nd, Upper	②	×
	Pd foil	CaO 2 nm×5 Pd 18 nm×4 Pd 40 nm×1	2nd, Upper	×	③
	CaO 8nm×1	Pd foil	2nd, Upper	×	×
	Pd foil	CaO 8 nm×1	1st, Lower	×	×
	CaO 2 nm×1 Pd 40 nm×1	CaO 2 nm×1 Pd 40 nm×1	2nd, Upper	④	⑤
	CaO 2 nm×5 Pd 18 nm×4 Pd 40 nm×1	CaO 2 nm×5 Pd 18 nm×4 Pd 40 nm×1	2nd, Upper	⑥	⑦

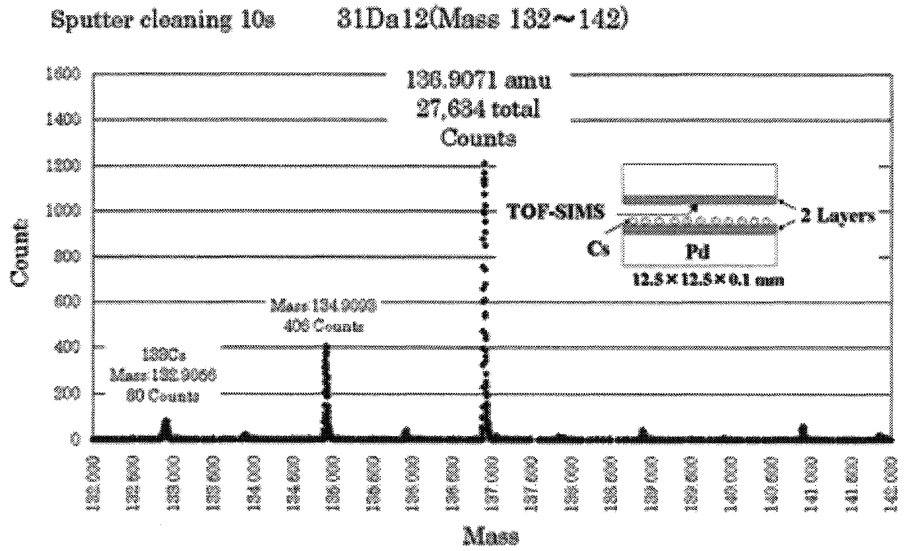

Fig. 2 TOF-SIMS spectrum in the mass range of 132-142 u for a combined Pd sample with a single-fold Pd/CaO layer after deuterium permeation.

regarded as definite ones.

Fig. 3 shows the normalized count intensity for 5 positive cases providing marked count peak at 137 u. The intensity is defined as the total count of secondary ions at 137 u divided by that of ^{69}Ga. The figure shows that the substance with mass number 137 was effectively produced between the double multi-layered Pd samples. Of particular interest is that the peak at 137 u for the opposite surface was higher than that for the Cs deposited surface.

Table 2 provides the most likely candidates of the substance with mass number 137. The peak position at ~133 u on the TOF-SIMS spectrum was taken as a standard indicating the real mass of Cs from which we have deduced the correct mass of

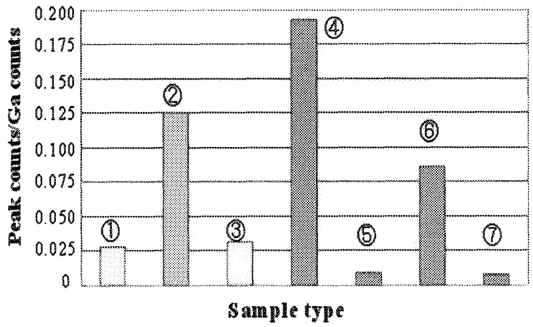

Fig. 3 Normalized count intensity at 137 u.

Table 2. Candidates for the substance with mass 137.

	Mass (u)	Peak deviation (mu)
CsD_2	136.9336	- 27.7
$^{106}PdOCH_3$	136.9219	- 15.9
Contaminating ^{137}Ba		
Produced ^{137}La	136.9065	0.5
Produced ^{137}Ba	136.9058	1.1
Produced ^{137}Cs	136.9071	- 0.1

substance with mass number 137. The peak deviation in the table is defined as (the obtained mass at 137 u−the obtained mass of Cs) −(the real mass of each substance− the real mass of Cs). These peak deviation values in Table 2 are deduced from the spectrum of Fig. 2.

As mentioned above, the count intensity observed at 137 u was usually higher than that observed at 135 u. In general, amount of CsD is thought to be much more than that of CsD_2 when they are formed by chemical process during the deuterium permeation experiment. Accordingly, It is unlikely that the substance with the mass 137 is CsD_2. Further, the value of peak deviation -27.7 mu for CsD_2 in the table is enough lager than the error range ±3 mu. This also implies that the substance with the mass 137 is not CsD_2.

The natural isotopic abundance of ^{105}Pd, ^{106}Pd and ^{108}Pd are 22, 27 and 26%, respectively. On the basis of the Pd natural isotopic abundance, the count intensity at139 u by $^{108}PdOCH_3$ formation should have been as large as that at 137 u , if we assume that the substance of mass 137 was $^{106}PdOCH_3$. In other words, a marked count due to $^{108}PdOCH_3$ should have been seen at 139 u in

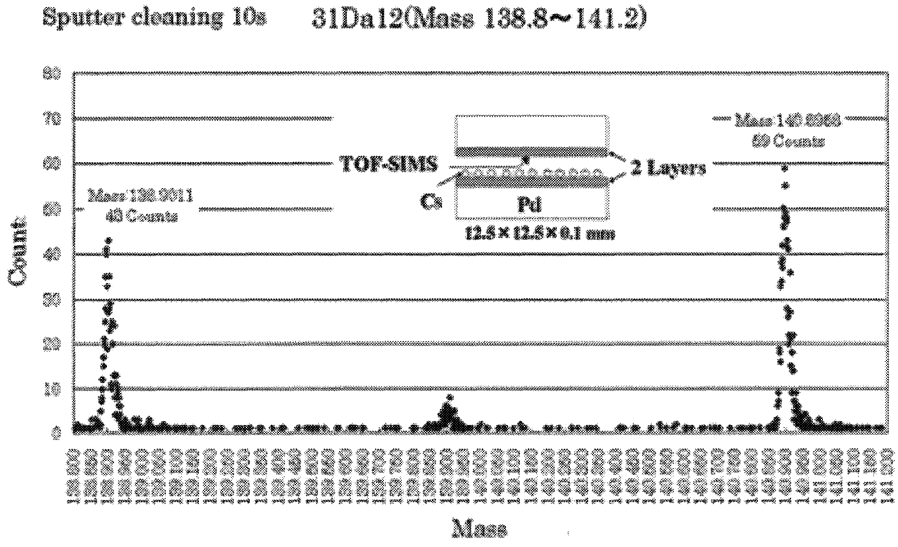

Fig. 4 TOF-SIMS spectrum of mass number range 139-141 for a combined Pd sample with a single Pd/CaO layer on each Pd sheet after deuterium permeation.

Fig. 2. However, there existed a peak of extremely low count intensity at 139 u. Consequently, the contribution of $^{106}PdOCH_3$ to form the peak at 137 u is thought to be negligible. Further, no marked peak appeared at 136 u, which corresponds to the mass of $^{105}PdCOH_3$. In addition, the peak deviation of 15.9 mu for $^{106}PdOCH_3$ in Table 2 is fairly larger than the error range of 3 mu. This consideration yields that the compounds of ^{106}Pd cannot account for the marked count at 137 u in Fig 2. That is, the molecule $^{106}PdOCH_3$ is out of the candidate substance.

Similarly, on the basis of Ba natural isotopic abundance, the element of ^{137}Ba contaminant can be excluded from the candidate as is explained in the following. The natural isotopic abundance of ^{137}Ba and ^{138}Ba are 11 and 72%, respectively. Thus, the element of ^{137}Ba contaminant can be possible candidate only when considerably large count intensity was observed at 138 u. To the contrary, we have not recognized such a large peak at 138 u as seen in Fig. 2, where only an extremely low peak probably due to Ga_2 is seen. This implies that the substance of mass 137 must not be ^{137}Ba contaminant but the newly produced ^{137}Ba, if the substance corresponding to the peak at 137 u is ascribed to ^{137}Ba.

Thus, the substance of mass number 137 observed only after deuterium permeation with Cs deposition is unlikely to be contaminants but would be newly produced elements of ^{137}Ba, ^{137}La, or ^{137}Cs. Among these three possible candidates, ^{137}La might be the most likely candidate, because ^{137}La is the only nuclide that could be formed from ^{133}Cs by simple addition of two deuterons. Besides those listed in Table 2, there are ten candidate elements with mass number of 137 in the atomic number range from 52 (^{137}Te) to 64 (^{137}Gd). However, these elements have relatively short lifetimes ranging from seconds to hours. Accordingly, we have excluded these ten elements from the possible candidates.

A TOF-SIMS spectrum of mass range 139-141 after sputter cleaning for a combined sample with a single-fold Pd/CaO layer is shown in Fig. 4. It is interesting to note that the count intensity at 141 u is often slightly higher than that at 139 u as seen in Fig. 4, even though both intensities are relatively low. There is a tendency that the count intensity at 141 u becomes higher coincidentally with that at 137 u. The calibrated mass obtained by the TOF-SIMS for the substance with mass number 141 and the real mass of ^{141}Pr are 140.8957 and 140.9076 u, respectively. Although the difference of 11.9 mu between the two masses is relatively large, there remains a possibility that the substance is ^{141}Pr. Taking account of the results of experiment by Iwamura et al. [1], all the results obtained in the present study suggest an important role of alpha cluster in the transmutation process with mass number increase by 4, 8 and 12.

4. Conclusion

The substance with mass number 137 was effectively produced between the double multi-layered Pd samples. The result suggests production of an element with mass 137 which would be transmuted from ^{133}Cs. The substance with the mass 137 could be ^{137}La, ^{137}Ba or ^{137}Cs produced during deuterium permeation by some nuclear transmutation occurring on/in the uppermost layer of multi-layered Pd sample. The Pd/CaO thin layers on Pd base foil might contribute to induce a low energy nuclear reaction producing an element with mass number 137.

Acknowledgment

The authors acknowledge the support of TEET (The Thermal and Electric Energy Technology Foundation).

References

1) Y. Iwamura, T. Itoh and, M. Sakano, Jpn. J. Appl. Phys., 41, 4642 (2002).
2) A. Kitamura, R. Nishio, H. Iwai, R. Sato, A. Tanike and Y. Furuyama, Proc. 12th International Conference on Cold Fusion, p. 272 (2006).
3) H. Yamada, S. Narita, S. Taniguchi, T. Ushirozawa, S. Kurihara, M. Higashizawa, H. Sawada and M. Itagaki,

Proc. 12th International Conference on Cold Fusion, p. 196 (2006).
4) H. Yamada, S. Narita, S. Taniguchi, T. Ushirozawa, S. Kurihara, M. Higashizawa and M. Itagaki, Proc. 7th Meeting of Japan CF Research Society, p. 28 (2006).
5) H. Yamada, S. Narita, D. Sato, T. Ushirozawa, S. Kurihara, M. Higashizawa, K. Iida, H. Ohata and H. Nanao, Proc. 8th Meeting of Japan CF Research Society, p. 26 (2007).

Proceedings of JCF9, March 28-29, 2009, Shizuoka-ken Sangyo Keizai Kaikan, Shizuoka, Japan

Investigation of the Cold Fusion Phenomenon in the Surface Region of Hydrogen Non-occlusive Metal Catalysts; W, Pt, and Au[†]

Hideo Kozima[*] and Tadahiko Mizuno[**]

[*]Cold Fusion Research Laboratory, 597-16 Yatsu, Aoi, Shizuoka, 421-1202, Japan.

[**]Division of Energy Environment, Graduate School of Engineering, Hokkaido University, Kita-ku Kita 13 Nishi 8, Sapporo 060-8628, Japan.

[†]The summary of this paper is presented at *March Meeting of the American Physical Society, Session B16: Cold Fusion* (March 16, 2009, Pittsburg, Philadelphia, USA).

Abstract

Experimental data sets of the cold fusion phenomenon (CFP) obtained in the contact catalysts W, Pt and Au are investigated from our point of view using the TNCF model common to whole data of the CFP in various systems performed in almost twenty years after its discovery. These metals do not occlude hydrogen isotopes in contrast to main systems where observed the CFP, transition-metal hydrides and deuterides, which occlude hydrogen isotopes. The contact catalysts shed light on atomic processes necessary to form a matter in the surface regions responsible for the CFP (the cf-matter) and also on nuclear processes to realize the nuclear transmutation (NT) accompanying huge excess energy production. The former may have a close relation with the mechanism of catalysis. Furthermore, experimental data sets in these metals have shown existence of two-steps in nuclear transmutations (NT) from lattice nuclei ${}^{A}_{Z}X$ to new nuclides: (1) Violent step with large changes ΔA of the mass number A and (2) Calm step with $\Delta A = 1$. The NT in the step 1 obeys the stability law.

1. Introduction

In the experimental data sets obtained in the cold fusion phenomenon (CFP) in these 20 years, there are various curious and wonderful facts difficult to understand from common sense of physics of nuclei and solids [1 – 3]. The materials (CF materials) where observed the CFP have been mainly the deuterides/hydrides of transition metals which can occlude hydrogen isotopes by the occlusion ratio η, defined as a number of H or D vs. host atoms, up to $\eta = 1$ for Pd and Ni and to $\eta = 2$ for Ti. There is a fact that shows an existence of a minimum value η_{min} for the occurrence of the CFP. In the case of PdD_x, the minimum value was about 0.8; $\eta_{min} \approx 0.8$.

Therefore, it is generally supposed that the higher the ratio η we make, the easier the CFP occurs. From this experience, we are apt to consider that the occurrence of the CFP in such hydrogen non-occlusive metals as W, Pt and Au is almost out of the question. However, from chemical point of view, very many transition metals, both hydrogen occluding and non-occluding metals altogether, have been used as catalysts for chemical (atomic) reactions for many years. A few trials have been performed by electrochemists to check the possibility to obtain positive results of the CFP with the hydrogen non-occluding metal catalysts. The works on the W [4], Pt [5] and Au [6] were some of them which have shown the occurrence of the nuclear

transmutation. We discuss its implication in this paper using knowledge obtained in science of catalysis and our models (TNCF and ND models) which has been successfully applied for analyses of the CFP in the hydrogen occluding transition-metal hydrides/ deuterides [1, 7]. The trapped neutron catalyzed fusion (TNCF) model assumes existence of quasi-stable neutrons in CF materials which catalyze nuclear reactions in them. The neutron drop (ND) model is an extended model of the TNCF model where assumed existence of a high-density neutron matter and neutron drop composed of Z protons and (A-Z) neutrons.

2. Experimental Data Sets obtained by Ohmori et al. and Mizuno et al. with Cathodes W, Pt and Au

In the electrolysis experiments with these metals as electrodes and with electrolytic solutions of several electrolytes in light or heavy water, the transmuted nuclides were observed in the surface layer of electrodes. The generated nuclides were localized in areas with a diameter of around a few μm in the surface layer of a width less than 1 μm. Typical nuclides observed in the host metals, W [4], Pt [5] and Au [6], are shown as follows.

In the case of the W cathode, electrolytes used are K_2CO_3, Na_2SO_4, Rb_2CO_3, Cs_2CO_3, $Ba(ClO_4)_2$. There occurred two types of nuclear transmutation (NT); Type I and Type II. The generated elements were Fe, Cr and Ni in the case of Type I, and Fe, Ti and Ca in the case of Type II. Typical amount of generated elements in the Type I case is 67.4, 16.9 and 7.9 at.%, respectively. Isotopic ratios of typical nuclides of Fe had shown shifts from natural ones in parentheses; ^{56}Fe 91.0 at.% (91.66) and ^{57}Fe 2.9 at.% (2.19).

In the case of the Pt cathode, electrolytes used are LiOH, NaOH, KOH, $NaHCO_3$ and H_2SO_4. The generated elements were Fe, Ni, Cu, Mn, K and Cl. The amounts of Fe and Ni were outstanding.

In the case of the Au cathode, electrolytes used are Na_2SO_4, K_2SO_4, K_2CO_3 and KOH. The generated elements were Mg, Si, K, C, Ti and Fe. In this case, isotopic ratios of nuclides of these elements had also shown shifts from natural ones as shown in Table 1 (Table III of [6]).

Table 1. Isotopic content of several elements by SIMS analysis in experiments with Au cathodes in H_2O solution (Table III of [6])

Isotopic Content of Several Elements by SIMS Analysis

Element	Mass Number	Signal Intensity[a] (count)	Atomic Content (%) Scan Number 1	2	3	Natural Isotopic Abundance (%)
Magnesium	24	854	77.1	80.5	80.5	78.70
	25	135	12.2	8.9	9.2	10.13
	26	119	10.7	10.6	10.3	11.17
Silicon	28	1001	90.8	89.4	89.3	92.21
	29	62	5.6	5.9	5.5	4.68
	30	40	3.6	4.7	5.2	3.09
Potassium	39	3720	93.9	92.0	94.1	92.21
	41	240	6.1	8.0	5.9	6.88
Calcium	40	2746	94.7	95.5	95.9	96.97
	42	24	0.8	0.8	0.8	0.64
	44	131	4.5	3.7	3.3	2.06
Titanium	46	463	14.4	12.6	10.4	7.93
	47	203	6.3	7.2	7.0	7.28
	48	2173	67.6	69.2	73.1	73.94
	49	180	5.6	5.3	5.1	5.51
	50	197	6.1	5.6	4.4	5.34
Iron	54	163	7.0	4.5	3.6	5.82
	56	1816	77.4	74.3	73.2	91.66
	57	333	14.2	20.1	21.8	2.19
	58	33	1.4[b]	1.1[b]	1.4[b]	0.33

[a]Data of first scan.
[b]Contains ^{58}Ni.

On the other hand, it is clear that the catalysis of atomic (chemical) reactions occurs at surface region as the fact shows that the surface of platinum used as a catalyst becomes more and more spongy and porous as it is used. Thus, a phase of catalysis is described as formation of some sort of compound between the catalyst and hydrogen thereby providing a new reaction

path whose activation energy is very low. This phase of catalysis is in accordance with features obtained in the experiments of the CFP.

In the CFP, we have observed various transmuted nuclides with mass numbers ranging from A = 6 (Li) to 208 (Pb), outstanding examples of them obtained in W, Pt and Au by Mizuno et al. have been shown above, in the surface region of samples with depth of around 10^2–10^3 nm accompanying enormous excess energy. This fact shows that there are formed the cf-matter responsible for the CFP in the surface region of these hydrogen non-occluding metals. The formation of the cf-matter may be realized by two steps; (1) atomic processes providing formation of atomic arrangement necessary for the second step, and (2) nuclear processes to form the cf-matter responsible for the NT.

Therefore, it seems certain that there are common factors in the catalysis of atomic reactions and in the atomic processes for the CFP. Knowledge obtained in electrochemistry will help to understand the mechanism of nuclear transmutation in the CFP.

3. Stability Law of the Nuclear Transmutation in W, Pt and Au

Experimental data sets on the nuclear transmutation in these metals obtained by Ohmori et al. and Mizuno et al. [4 – 6] have confirmed the stability law in the generation of new nuclides discovered by us ([1] Fig. 2.11) with some characteristic modification by the experimental system. The amounts of transmuted nuclei are in accordance with the relative abundances of corresponding nuclei in the universe. This means that the more stable a nucleus, the more abundant the nucleus in the universe is, and therefore the more frequently the nucleus is observed in the nuclear transmutation in the CFP.

This fact shows that nuclear transmutations of the CFP occurring in the surface regions of metal catalysts are effected by many-body reactions similar to nuclear processes occurring in celestial bodies where the natural abundance of elements has been determined. The mechanism of the CFP proposed by us with the cf-matter formation at surface/boundary layers is in accordance with this fact.

Recent experiment on phenanthrene with platinum mesh as a substrate [8] may have close relation with experiments on these metals reported before.

4. Surface Hydrogen States and Possible Mechanisms of the NT in W, Pt and Au

As discussed in a paper [9] where the relation of non-local hydrogen wavefunctions and cf-matter formation is investigated, there are evidences showing existence of non-localized subsurface and also body hydrogens in metal catalysts of transition metals of both hydrogen occluding and non-occluding natures.

Christmann et al. [10] investigated chemisorbed hydrogens more or less delocalized along the surface. Mate et al. [11] discussed a delocalized, quantum description of adsorbed hydrogen ("hydrogen fog") to explain their experimental result on the high-resolution electron energy loss spectra (HREELS). Alefeld [12] discussed hydrogen diffusion in metals using a band structure in which the activation energy is the energy difference between the conduction band and the ground state.

Christmann [13] discussed that there exists another potential for hydrogen trapping between the chemisorbed and absorbed hydrogen, called the "subsurface hydrogen" to understand the hydrogen sorption on pure metal surfaces. Furthermore, Burch [14] discussed more variety of hydrogen states on and

in the surface region from the data for polycrystalline Pt as follows. There are seven or eight types of adsorbed hydrogen, half of which refer to hydrogen adsorbed on the external surface of the Pt, and the remainder refers to hydrogen incorporated in different forms at dislocations, grain boundaries, or inclusions.

It is interesting to notice that Gosar et al. [15] noticed ion energy band in relation to ice crystal prior to Chubb et al. [16] who used the concept to explain the CFP.

Thus, the non-localized hydrogen wavefunctions have been used to explain physical and chemical properties of transition-metal catalysts from the late 1070's. We have recently used the concept to explain the possible existence of the cf-matter which has given a consistent explanation of various events in the CFP [1, 2, 7, 9]. The TNCF and the ND models supported by these knowledge of non-local hydrogen wavefunctions can give a consistent explanation of the experimental data on W [17], Pt and Au. In this paper, we concentrate our efforts to the case of Pt and Au cathodes leaving the W case to the published paper [17].

The common characteristics of the both cases are production of several elements with small proton numbers (Z = 17 and 19 for Pt and 12 and 14 for Au) and large proton numbers (Z = 25 – 29 for Pt and 19 – 26 for Au). This feature reminds us the characteristic mass distributions obtained by several experiments as shown in Figs. 2.7 and 2.8 of [1].

In the case of the Pt cathode, as given in Section 2, the generated elements were Fe, Ni, Cu, Mn, K and Cl. The amounts of Fe and Ni were outstanding in accordance with the stability law as pointed out above.

An example of possible nuclear reactions mediated by the neutron drops ${}^{A}{}_{Z}\Delta$ in the cf-matter formed at around surface region are written down as follows (α = 190 – 198);

$$ {}^{\alpha}{}_{78}\mathrm{Pt} + {}^{A}{}_{Z}\Delta = {}^{56}{}_{26}\mathrm{Fe} + {}^{58}{}_{26}\mathrm{Fe} + {}^{58}{}_{28}\mathrm{Ni} + {}^{64}{}_{28}\mathrm{Ni} + {}^{55}{}_{25}\mathrm{Mn} + {}^{A'}{}_{Z'}\Delta \quad (1) $$

when $\alpha = 190$, $A = 101 + A'$, $Z = 55 + Z''$.

In the case of the Au cathode, electrolytes used are Na_2SO_4, K_2SO_4, K_2CO_3 and KOH in H_2O. The generated elements were Mg, Si, K, C, Ti and Fe. In this case, isotopic ratios of nuclides of these elements had also shown shifts from natural ones as shown in Table 1 (Table III of [6]). The production of new elements is explained by a similar equation to Eq. (1) of the case of Pt cathode using the neutron drop ${}^{A}{}_{Z}\Delta$ to feed necessary number of protons and neutrons

Another interesting point that the NT data [4 – 6] obtained in these catalysts show is the isotopic ratios of the generated nuclides. As we see in the data given above, e.g. ${}^{A}{}_{26}\mathrm{Fe}$ in the case of Au electrodes, the abundance of ${}^{56}{}_{26}\mathrm{Fe}$ is lower and that of ${}^{57}{}_{26}\mathrm{Fe}$ is higher than the corresponding natural abundances. This result may be an evidence that there are such secondary nuclear reactions assumed in the TNCF model as

$$ n + {}^{56}{}_{26}\mathrm{Fe} \rightarrow {}^{57}{}_{26}\mathrm{Fe} + Q. \ (\sigma_{n\mathrm{Fe}56} = 2.81 \text{ b}), \quad (2) $$

in addition to the first collective nuclear processes resulting in the generation of nuclides in the cf-matter in proportion to their stability.

Table 2. Natural abundance $x^{(0)}{}_{i}$ (%), average experimental abundance $(x_i)_{exp}$ (%), and cross section $\sigma_{n\mathrm{Fe}}$ (b) for the absorption of a thermal neutron by an iron isotope ${}^{A}{}_{26}\mathrm{Fe}$ (A = 54, 56 and 57 designated by i = 1, 2 and 3). x_i are calculated using the data given in Table 1.

i (isotope)	$x^{(0)}{}_{i}$ (%)	$(x_i)_{exp}$(%)	$\sigma_{n\mathrm{Fe}}(=\sigma_i)$ (b)
1 (${}^{54}{}_{26}\mathrm{Fe}$)	5.82	5.0	2.16
2 (${}^{56}{}_{26}\mathrm{Fe}$)	91.66	75.0	2.81
3 (${}^{57}{}_{26}\mathrm{Fe}$)	2.19	18.7	2.46

If we assume the generated nuclides by the primary process have the same isotope ratios to those of natural abundances $x^{(0)}_i$ (%), we can determine the density n_n of the trapped neutrons participating in the secondary process Eq. (2) and check the applicability of the TNCF model to the secondary process as follows using the observed abundances of $^{54}_{26}$Fe, $^{56}_{26}$Fe and $^{57}_{26}$Fe.

The change of abundances of isotopes according to the reactions similar to Eq. (2) is written down as follows [1, 2];

$$x_1 = x^{(0)}_1 - Cn_n\sigma_1 x^{(0)}_1 = (1 - Cn_n\sigma_1)\, x^{(0)}_1 \quad (3)$$

$$x_2 = x^{(0)}_2 - Cn_n\sigma_2 x^{(0)}_2 = (1 - Cn_n\sigma_2)\, x^{(0)}_2 \quad (4)$$

$$x_3 = x^{(0)}_3 - Cn_n\sigma_3 x^{(0)}_3 + Cn_n\sigma_2 x^{(0)}_2 = (1 - Cn_n\sigma_3)\, x^{(0)}_3 + Cn_n\sigma_2 x^{(0)}_2, \quad (5)$$

where $C = 0.35 n_n v_n \tau$, and n_n and v_n are the density and the thermal velocity of the trapped neutrons in the model. The parameter τ is the elapsed time between the first experiment where occurred the generation of $^{A}_{26}$Fe in accordance with the stability law and the second experiment where the abundances tabulated in Table 1 were observed. The value of v_n at room temperature is given as $v_n = 2.2\times10^5$ cm/s.

We can determine n_n from Eq. (3) using the experimental value of x_1; $(x_1)_{exp}$ = 5.0 %, if we know the elapsed time τ. Then, we can calculate theoretical values $(x_2)_{th}$ and $(x_3)_{th}$ of x_2 and x_3 using the determined value of n_n to compare to their experimental values $(x_2)_{exp}$ and $(x_3)_{exp}$.

If we take τ = 1 day = 8.64×10^4 s, we obtain C = 6.65×10^9 cm, and

$$n_n = 1.0\times10^{13}\ \text{cm}^{-3}. \quad (6)$$

This value is compared with the values of n_n of about 10^8–10^{12} cm^{-3} determined for various data sets and tabulated in Tables in our books [1, 2].

Using the value of n_n in Eq. (6) or the value C n_n = 6.5×10^{22} cm^2 into Eqs. (4) and (5), we obtain $(x_2)_{th}$ and $(x_3)_{th}$ as follows;

$$(x_2)_{th} = 75.1\ \%, \quad (7)$$

$$(x_3)_{th} = 18.3\ \%. \quad (8)$$

These values are compared with their corresponding experimental values tabulated in the column 3 of Table 2;

$$(x_2)_{exp} = 75.0\ \%, \quad (9)$$

$$(x_3)_{exp} = 18.7\ \%. \quad (10)$$

The coincidence of these values of $(x_i)_{th}$ and $(x_i)_{exp}$ (i = 2, 3) is excellently good. We may take this result as showing the validity of our interpretation of the experimental results by the two-step process: (i) The *violent transmutation* of nuclides producing various nuclides in accordance with the stability law from the host nuclides mediated by the cf-matter by such a reaction Eq.(1) and (ii) the rather *calm transmutation* of nuclides according to such a single neutron absorption as expressed by Eq. (2).

This analysis could be extended to analysis of other elements obtained in the experiments. As an illustration, we take up the case of titanium. The data for isotopes of Ti with A = 47 and 48 are compiled as shown in Table 3.

The change of abundance of $^{48}_{22}$Ti is expressed as follows corresponding to Eq. (5):

$$x_2 = x^{(0)}_2 - Cn_n\sigma_2 x^{(0)}_2 + Cn_n\sigma_1 x^{(0)}_1 = (1 - Cn_n\sigma_2)\, x^{(0)}_2 + Cn_n\sigma_1 x^{(0)}_1. \quad (11)$$

Table 3. Data for Ti isotopes corresponding to Table 2 for Fe isotopes.

i (isotope)	$x^{(0)}_i$(%)	$(x_i)_{exp}$(%)	$\sigma_{nTi}(=\sigma_i)$ (b)
1 ($^{47}_{22}$Ti)	7.28	5.0	1.70
2 ($^{48}_{22}$Ti)	73.94	70.0	7.84

Using the value $C\,n_n = 6.5\times10^{22}$ cm^2 determined by the

analysis of data for Fe into Eq. (11), we obtain theoretical value of isotopic abundance $(x_2)_{th}$ of $^{48}_{22}Ti$ as follows;

$$(x_2)_{th} = 37.0\ \%, \quad (12)$$

to compare with the average experimental value;

$$(x_2)_{exp} = (67.6 + 69.2 + 73.1)/3\ \% = 70.0\ \%, \quad (13)$$

The coincidence of values in Eq. (12) and Eq. (13) is qualitatively satisfactory if we consider the comparison is between different elements which show different sensitivity for SIMS (secondary ion mass spectrometry). Thus, the surprisingly good coincidences of the values in Eqs. (7) – (10) and satisfactory coincidence of the values in Eqs. (12) and (13) should be taken as qualitative evidence of validity of our interpretation.

5. Discussions

As we have shown above, the experimental data sets of the CFP obtained in those hydrogen non-occlusive metals, W, Pt and Au, should be related to essential physical processes in the surface region of cathodes.

First of all, experimental data qualitatively exhibit the stability law in the nuclear transmutation, the more stable a nuclide the more often the nuclides generated, showing that the CFP is a many-particle process explained for instance by the ND model assuming existence of a neutron drop $^{A}_{Z}\Delta$, a cluster of neutrons and protons. A possible formation of the cf-matter in which the neutron drops can be easily formed is discussed quantum mechanically in previous papers and books [1, 9, 18, 19]

Second, the isotope distribution of iron is successfully analyzed by the TNCF model showing existence of a single-neutron process. The abundance ratio of iron isotopes estimated by the TNCF model agreed very well with experimentally obtained values as shown in Eqs. (7) – (10).

Thus, the implication of two models, the TNCF and ND models, proposed by us to explain experimental data sets showing nuclear transmutations with small changes of mass numbers and simultaneous production of many elements with large changes of mass numbers, respectively, is interpreted as one corresponding to calm absorption of a neutron and succeeding intranuclear stabilization as shown in Eq. (2), and another to a violent reaction of host nuclides with neutron drops to produce several nuclides with large changes of mass numbers as shown in Eq. (1).

The knowledge of catalysts science supported the quantal approach to show validity of premises assumed in the TNCF and the ND models which have been effective to explain the experimental data of nuclear transmutations obtained in W, Pt and Au. The quantal bases of these models might be useful to investigate physical processes of catalysis which are not necessarily fully elucidated yet.

Acknowledgement

The authors would like to express their thanks to John Dash of Portland State University where main part of this work was performed while one of the authors (H.K.) stayed there by his courtesy. This work is partially supported by a grant from the New York Community Trust.

References

1. H. Kozima, *The Science of the Cold Fusion Phenomenon*, Elsevier Science, 2006. ISBN-10: 0-08-045110-1.

2. H. Kozima, *Discovery of the Cold Fusion Phenomenon*, Ohtake Shuppan, Tokyo, 1998. ISBN: 4-87186-044-2.

3. E. Storms, *Science of Low Energy Nuclear Reaction*, World Scientific Publishing Co., 2007. ISBN 10-981-270-620-8.

4. T. Ohmori and T. Mizuno, "Nuclear Transmutation Reaction Caused by Light Water Electrolysis on Tungsten Cathode under Incandescent Conditions," *Infinite Energy* **27**, pp. 34 – 39 (1999) (W).

5. T. Mizuno, T. Ohmori and T. Akimoto, "Detection of Radiation Emission, Heat Generation and Elements from a Pt Electrode Induced by Electrolytic Discharge in Alkaline Solutions," *Proc. ICCF7*, pp. 253 – 258 (1998).

6. T. Ohmori, T. Mizuno, Y. Nodasaka and M. Enyo, "Transmutation in the Electrolysis of Light Water – Excess Energy and Iron Production in a Gold Electrode," *Fusion Technology*, **33**, pp. 367 – 382 (1998)

7. H. Kozima, "Methodology of the Cold Fusion Research," in *ACS Sourcebook* J. Marwan and S. Krivit Eds., Oxford Univ. Press, 2009 (to be published).

8. T. Mizuno and H. Kozima, "Anomalous heat generation during hydrogenation of phenanthrene" *Proc. ICCF14* (to be published).

9. H. Kozima, "Non-localized Proton/Deuteron Wavefunctions and Neutron Bands in Transition-metal Hydrides/Deuterides," *Proc. JCF9* (to be published).

10. K. Christmann, R.J. Behm, G. Ertl, M.A. Van Hove, and W.H. Weinberg, "Chemisorption geometry of hydrogen on Ni(111): Order and disorder" *J. Chem. Phys.*, **70**, 4168 – 4184 (1979).

11. C.M. Mate and G.A. Somorjai, "Delocalized quantum nature of hydrogen adsorbed on the Rh(111) crystal surface" *Phys. Rev.* **B34**, 7417 – 7420 (1986).

12. Alefeld, "Hydrogen Diffusion in Metals" in A. Seeger, D. Schumacher, W. Shilling and J. Diehl Eds., *Vacancies and Interstitials in Metals*, North-Holland Pub. Co., Amsterdam, 1970. SBN 7204-0154-2

13. K.R. Christmann, "Hydrogen Sorption on Pure Metal Surface" in Z. Paal and P.G. Menon Ed. *Hydrogen Effects in Catalysis*, Marcel Dekker Inc., N.Y., 1988. ISBN 0-8247-7774-3.

14. R. Burch, "The Adsorption and Absorption of Hydrogen by Metals" in M.W. Roberts and J. M. Thomas Eds., *Chemical Physics of Solids and their Surfaces*, **8**, Royal Society of Chemistry, 1978. ISBN 0-85186-740-5

15. P. Gosar and M. Pintar, "H_3O^+ Ion Energy Bands in Ice Crystals" *phys. stat. sol.* **4**, pp. 675- 683 (1964)

16. T.A. Chubb and S. Chubb, "Cold Fusion as an Interaction between Ion Band States' *Fusion Technology*, **20**, 93 (1991).

17. H. Kozima, M. Fujii, K. Arai, H. Kudoh and K. Yoshimoto, "Analysis of Nuclear Transmutation in Micro-craters and Excess Heat Data in *W/H/Na(K) Systems" Reports of CFRL* (Cold Fusion Research Laboratory) **1-3**, 1 – 10 (March, 2004).

18. H. Kozima, "Quantum Physics of Cold Fusion Phenomenon," in *Developments in Quantum Physics*, ed. V. Krasnoholovets and F. Columbus, Nova Science, N.Y., 2004. ISBN: 1-59454-003-9. And also H. Kozima, *Rep. Fac. Science, Shizuoka Univ.* **39**, 21 – 90 (2005).

19. H. Kozima, "Anomalous Nuclear Reaction and Atomic Processes in Transition-Metal Hydrides and Deuterides" *Reports of CFRL* (*Cold Fusion Research Laboratory*), **4-1**, 1 – 18 (2005).

Proceedings of JCF9, March 28-29, 2009, Shizuoka-ken Sangyo Keizai Kaikan,
Shizuoka, Japan

Simulation of Transmutation Products on Palladium Cathodes

Norman D. Cook
Department of Informatics
Kansai University
Osaka, Japan

Abstract

A lattice model of nuclear structure that is isomorphic with the standard IPM has previously been shown to predict the asymmetrical fission fragments produced by the thermal fission of uranium. The same model can be used to predict the transmutation products found on palladium cathodes following electrolysis, as reported by Mizuno [1]. It is shown that the macroscopic structure of the lattice is virtually identical to the structure of the liquid-drop mode (LDM), since both models assume a strong, local (<3 fm) nucleon-nucleon interaction. Although the IPM assumes a weak "effective" nuclear force, the quantal states of the IPM are reproduced in the lattice model, which is based on a realistic strong force. I conclude that the local substructure provided by the lattice is a necessary addition to conventional nuclear structure theory in order to explain the nuclear transmutations in both thermal fission and low-energy nuclear reactions.

Introduction

The transmutation of nuclear species was discovered in 1938, and soon understood to be due to the fission of Uranium isotopes into much smaller fragments. Already by 1939, Bohr and Wheeler had developed a model to explain the energy release associated with fission: the liquid-drop model (LDM). That model is still in use 70 years later, but the LDM has proved ***incapable*** of explaining the transmutation process itself, specifically, the overwhelming tendency for the actinides that undergo thermal fission to break into asymmetrical (3:2) mass fragments. ("The most significant failure of the [liquid-drop] theory is the failure to account for asymmetric mass distributions." Vandenbosch & Huizenga [2]). It is worth recalling that the asymmetrical fission of U^{235} is the phenomenon that underlies virtually all of modern nuclear technology and is the main reason why nuclear physics, unlike astrophysics, is of more than academic interest.

Because of the conceptual simplicity and quantitative successes of the LDM, many researchers since the 1940s have attempted to retain the energy-properties of the LDM, by introducing ***ad hoc*** parameters that imply asymmetrical fragments. Such parameters are included (i) to produce asymmetrical dumb-bell shape distortions of the liquid-drop that will scission asymmetrically, (ii) to allow for the asymmetrical elongation of the "neck" region at the moment of fission, (iii) to distort the nuclear surface for asymmetrical break-up, or (iv) to favor the selection of fission channels that produce asymmetrical fragments. Unfortunately, all such parameters are derived from the experimental data, and are not intrinsic to the LDM itself. In other words, the ***empirical*** fragment asymmetry is used to "predict" the asymmetry. At best, such theoretical models are consistent with empirical facts, but they remain inconclusive insofar as adjustable parameters are required to make the models work.

An alternative approach is to use a nuclear model whose inherent properties allow for predictions about fission fragments ***without*** empirical input concerning the phenomena to be explained. The model used here is the fcc lattice model [3-5]. It is unconventional insofar as it is a "frozen liquid-drop" (a lattice of nucleons), but, importantly, it retains both the macroscopic properties of the LDM ***and*** the conventional quantal properties of the well-established independent-particle model (IPM). That is, LDM-like properties are found in the lattice because both models rely fundamentally on a local, short-range (<3 fm) nuclear force acting only among nearest-neighbor nucleons. The constant core density of nuclei, the dependence of R on the number of nucleons, and the total nuclear binding energies are easily explained in ***both*** models using a realistic strong force, and there is no need to postulate an unrealistic "effective force," such as that which has caused decades of problems for the IPM approach to nuclear structure.

Importantly, however, the lattice model reproduces the central strength of the IPM, i.e., the quantal description of the individual nucleons and their summation to give nuclear properties. Specifically, there is precise agreement between the lattice model and the IPM, because each nucleon in the lattice model has a fixed set of quantum numbers (***n, j, m, s, i***) that are dependent on the lattice coordinates of the nucleon (see below). As such, the lattice retains many of the characteristic strengths of the LDM, but is formally isomorphic with the IPM (where each nucleon is in a unique quantal state, as described in the Schrodinger equation using its

quantum numbers). In this regard, the fcc lattice model is a unique combination of the LDM and the IPM.

The present study was undertaken to examine the use of the lattice model for explaining the transmutation products that are known from both thermal fission and the transmutation products reported in LENR experiments. Notably, Mizuno [1] found not only deviations from the natural abundance of Pd isotopes on Pd cathodes, but also deposits of various elements on the cathode surface. Those results are undisputed as empirical studies and have been partially replicated by Miley, Iwamura and others, but questions remain concerning the physical mechanisms. Here I apply the same lattice-fission technique that explains the asymmetrical fission of uranium [4, 5] to the break-up of the Pd isotopes, again ***without*** the use of model parameters to produce the results.

The Lattice Model

Central to an understanding of the lattice model itself are two points: (i) the nuclear texture in the lattice is essentially identical to that in the conventional LDM, because both models rely on a realistic, short-range nuclear force. Moreover, (ii) there is a mathematical identity between the quantum mechanical description of nuclear quantum states (summarized by the quantum numbers, ***n, j, m, s, i***) and a specific lattice structure [3-5]. In the conventional IPM description of nuclear structure, each nucleon is presumed to be in an energetic state specified by its unique set of quantum numbers. Nucleon states are analogous to the quantum mechanical states of the electrons in electron orbitals and described by similar quantum numbers. The lattice structure that reproduces all of the nucleon states of the IPM (~shell model) is an antiferromagnetic face-centered-cubic (fcc) lattice with isospin layering. That lattice has been independently shown to be the lowest-energy condensed state of nuclear matter (N=Z), possibly present in so-called neutron stars [6]. The identity between the fcc lattice and quantum mechanics means that, if the conventional IPM structure of a nucleus is known, then the 3D lattice positions of all its nucleons can be deduced directly from Eqs. 6~8 (and, vice versa, starting with lattice sites, its IPM state can be deduced, Eqs. 1~5).

$n = (|x| + |y| + |z| - 3) / 2$ Eq. 1
$j = (|x| + |y| - 1) / 2$ Eq. 2
$m = |x| / 2$ Eq. 3
$s = ((-1)^{(x-1)}) / 2$ Eq. 4
$i = ((-1)^{(z-1)}) / 2$ Eq. 5
$x = |2m|(-1)(m+1/2)$ Eq. 6
$y = (2j+1-|x|)^{(i+j+m+1/2)}$ Eq. 7
$z = (2n+3-|x|-|y|)^{(i+n-j-1)}$ Eq. 8

where x, y and z are all odd-integers defining fcc lattice coordinates. Full details of the lattice model are available elsewhere [5]. Suffice it to say that the ***n***-shells of the harmonic oscillator are literally shells in the lattice (Eq. 1, Fig. 1), and all of the ***j***-, ***m***-, ***s***- and ***i***-subshells of the IPM model are defined in terms of lattice symmetries. It is worth emphasizing that the occupancies of ***all*** of the shells and subshells in the lattice model are identical to those in the IPM model – from which the highly-successful shell model is derived. In other words, the fcc lattice is a representation of ***conventional*** nuclear theory – essentially, a geometrical analog of the quantal regularities of the Schrodinger equation. It therefore provides a natural approach to questions concerning nuclear substructure ***without*** the need for ***ad hoc*** postulates concerning the manipulation of the nuclear potential well (i.e., model parameters that are not derived directly from QM).

Despite the seemingly "simple" geometry of the lattice model, the model is fully quantum mechanical (unlike the LDM) and implies a description of nucleon states that is identical to the IPM. Given the known validity of the IPM (~shell model) structure of nuclei, a unique lattice structure for any combination of N and Z is implied. Using the fcc structures for individual isotopes, the dynamics of lattice fragmentation can be examined without further empirical input.

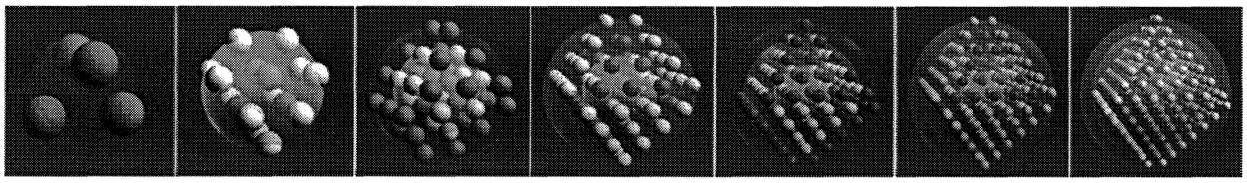

Figure 1: The ***n***-shells in the lattice built from a central tetrahedron show the same occupancy as the harmonic oscillator [3, 5]: $_2He^4$, $_8O^{16}$, $_{20}Ca^{40}$, $_{40}Zr^{80}$, $_{70}Yt^{140}$, $_{112}Xx^{224}$, $_{168}Xx^{336}$. The occupancies of all of the n-shells (illustrated here), j-subshells, and m-subshells of the harmonic oscillator are reproduced precisely in the lattice [5].

Fission of the Actinides

The break-up of a mini-lattice (A~240) is favored along those lattice planes where the number of interfragment

2-body interactions is low and simultaneously the interfragment Coulomb effect is high. Note that these are competing tendencies: ***asymmetrical*** fission is favored by the small number of nucleon-nucleon interactions binding small fragments to the larger parent nucleus, whereas the ***symmetrical*** (~1:1) split of the parent nucleus is energetically favored when equal numbers of proton charges are in both daughter fragments. Details of the simulation technique have been published elsewhere [4], but the basic idea is simply to calculate the strength of the attraction between the fission fragments (bonds) and the Coulomb repulsion at work along every possible plane through the lattice structure for each nucleus. The fission event that shows the lowest fission threshold per nucleus is then selected:

Fission threshold $\propto$ bonds – Coulomb repulsion Eq. 9

The Coulomb repulsion is a classical calculation, and the nature of the nuclear force underlying the nearest-neighbor bonds need not concern us. It is noteworthy that the prediction of ***symmetrical*** fission fragments is the classic deficiency of the LDM explanation of thermal fission. Without an "asymmetry parameter" – introduced explicitly to enhance asymmetrical fragmentation, the presumed liquid-like interior of large nuclei in the LDM inevitably predicts ***symmetrical*** fission – contrary to all findings on low-energy fission of the actinides. Shell model theorists have sought to introduce nuclear substructure (i.e., asymmetry) via the stability of "magic" numbers of protons and neutrons – and that view is the qualitative explanation of asymmetrical fission in most textbooks today. To the contrary, however, Strutinsky et al., who worked explicitly on this problem, have explicitly stated that the manipulations of the nuclear potential well needed to produce asymmetric fission have "little to do with the magicity of spherical fragments" [7] and the occasional presence of magic numbers 28 and 50 among the final fragments do not explain, qualitatively or quantitatively, the fragment asymmetries. (See [5] for a discussion of the non-role of magic numbers in fission.)

In contrast, the lattice model contains substructure inherent to the lattice itself. Using the default (~IPM) fcc structures for the actinides, calculation of the interfragment binding along lattice planes, together with interfragment Coulomb effects, already shows the predominance of ***asymmetrical*** fission fragments (3:2) (Figure 2). The fragment asymmetry is a direct result of the low fission barrier for lattice structures that are scissioned along oblique lattice planes. Vertical and horizontal cuts through the same structures produce symmetrical fragments, but demand breaking of many more 2-body bonds between the fragments.

In order to obtain a more precise fit between the empirical data and the model, parameters concerning the nuclear force can of course be added to the basic model, but the approximate asymmetry of 3:2 is obtained without the use of any fission-related parameters in the model. This fact can be verified using the Nuclear Visualization Software (NVS) that is freely available at: http://www.res.kutc.kansai-u.ac.jp/~cook.

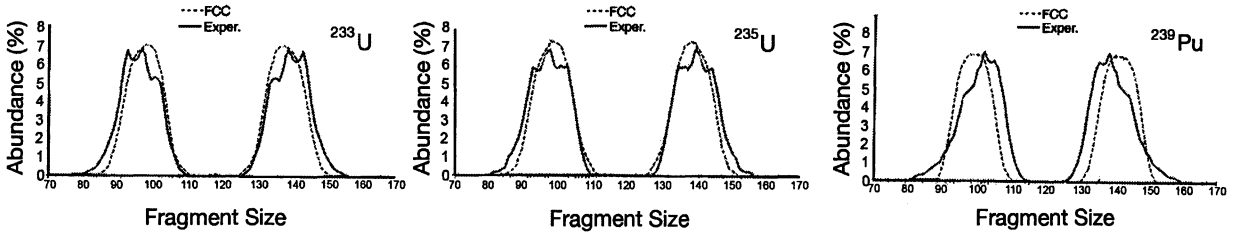

Figure 2: The parameter-less prediction of asymmetrical fragments in the thermal fission of the actinides using the lattice model [4, 5]. The experimental data are shown by the solid lines (experimental error lies within the width of the solid lines, i.e., there is ***real*** substructure in the experimental curve that survives the fission process). The approximate size of the fission fragments is well-reproduced in the lattice model. The slight discrepancy between theory and the experimental data is presumably due to the technique used to randomize nucleon localization on the surface of the lattice. This problem is currently under study.

Transmutation of Palladium

Among the most dramatic LENR results are those reported by Mizuno [1] on the transmutation of deuterium-loaded palladium. He and others have found not only changes in the abundance of various Pd isotopes, but also the deposition of various light- and medium-sized elements on the surface of the Pd cathodes. Specifically, Mizuno has reported that:

(i) Prior to the experiment, the measured abundances of Pd isotopes were virtually identical to the known natural abundances (Table 1, Column B).

(ii) Subsequent to electrolysis, there were significant changes in the relative abundances (Column C), suggestive of transmutation of the Pd nuclei at the surface of the electrode, with

(iii) gradually smaller changes in the natural abundances as measurements proceeded from the surface into the depth of the cathode.

Table 1: Experimental and Theoretical Changes in Palladium Isotopes Following Electrolysis

	EXPERIMENT			SIMULATION				
Isotope	% Abundance	Mizuno Data	% Change	Initial No.	Loss	Final No.	% Loss	% Abundance
Pd^{102}	1.0%	3.6%	+2.6%	1,020	658	362	65%	3.6%
Pd^{104}	11.1%	17.3%	+6.2%	11,140	9,408	1,732	84%	17.3%
Pd^{105}	22.3%	20.4%	-1.9%	22,330	20,288	2,042	91%	20.4%
Pd^{106}	27.3%	20.3%	-7.0%	27,330	25,298	2,032	93%	20.3%
Pd^{108}	26.5%	20.6%	-5.9%	26,460	24,398	2,062	92%	20.6%
Pd^{110}	11.7%	17.7%	+6.0%	11,720	9,948	1,772	85%	17.7%
Total	100.0%	100%		100,000	89,998	10,002	90%	100.0%
A	B	C	D	E	F	G	H	I

The percentage changes in the abundance of Pd isotopes (Column D) do not suggest any obvious regularity in the transmutation process, but a straight-forward simulation indicates that essentially all of the Pd isotopes were equally involved in the transmutation process. That is, assuming that measurements of the cathode surface were made on, say, 100,000 Pd nuclei (Column E), the "loss" of the various isotopes shown in Column F results in percentages (Column I) identical to those reported by Mizuno (Column C). What is of interest about these values is that they indicate that (with the possible exception of Pd^{102}, that accounts for only 1% of the natural abundance) ***all*** of the Pd isotopes were involved in nuclear reactions at approximately equal rates (~90%, Column H). In other words, if transmutation of Pd is the source of heat energy in these cold fusion experiments, then it is ***not*** the case that one or a few unusual isotopes are responsible for the effects, in so far as similar percentage decreases of all isotopes were involved. Clearly, this simulation does not indicate what the transmutation mechanism might be [8, 9], but it does show that, if some such mechanism is at work, the seemingly irregular changes in Pd isotopic abundances (Column D) are a consequence of similar percentage ***depletions*** in all isotopes (Column H). This is the main result obtained from the simulation of Pd transmutation, and has not apparently been commented on in the LENR literature.

Remarkable about the simulation is the fact that the solution that reproduces the Mizuno data is ***unique*** (±1%) provided only that we stipulate that there are no "negative losses" in Column F. If negative losses (i.e., increases in specific Palladium isotopes) were also allowed (e.g., transmutation of Pd^{106} into Pd^{110} by the addition of 4 neutrons), then there would be an infinite number of solutions, with both increases and decreases in Palladium isotopes (positive and negative "% Losses" in Column H). By restricting the simulation to the more realistic case of "losses only", only one solution within the bounds of error in the experimental data (±1%) is possible (essentially a unique solution to a simultaneous equations problem).

It is also noteworthy that the changes in isotopic percentages in the depth of the cathode, as reported by Mizuno, are reproduced in the simulation (Figure 3). The agreement between the Mizuno data and the simulation results clearly indicates the self-consistency of the experimental data and the likelihood that all of the Palladium isotopes are equally involved in transmutation.

If a constant percentage of surface Pd isotopes are transmuted in LENR experiments, the next question is: what are they transmuted to?

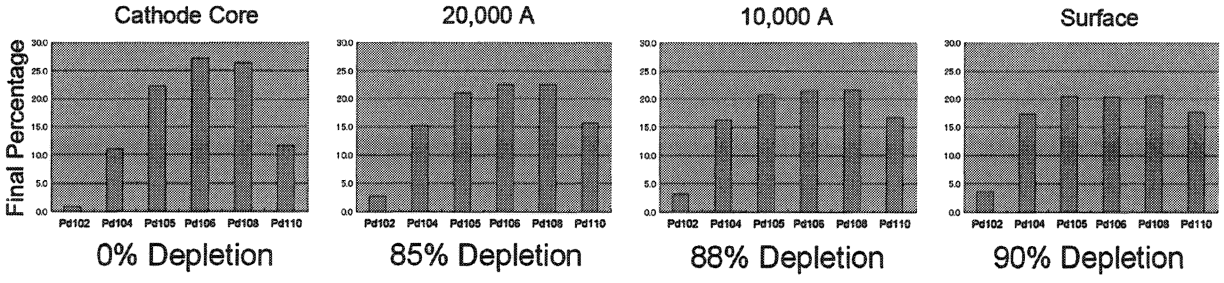

Figure 3: The simulation at 85%, 88% and 90% depletion of the surface isotopes reproduces the experimental data (±1%) on the percentage changes with increasing depth into the Palladium isotopes [1] – again suggesting that all isotopes undergo transmutation.

Palladium Fission Fragments

Simulation of the fission of Palladium was carried out on each of the six stable Pd isotopes using the lattice model [3-5]. The nucleon build-up process is that known from the standard IPM and the lattice coordinates of each nucleon are given by Eqs. 1~8. The lattice positions of equivalent nucleons (i.e., nucleons whose *j*-value are not empirically known) are determined by the maximization of nearest-neighbor interactions, while minimizing Coulomb repulsion. In other words, 46 protons and 56~64 neutrons were placed at fcc lattice sites, such that the final structure has (i) maximal nearest-neighbor binding, (ii) minimal Coulomb repulsion, and (iii) a total *J*-value (calculated from the sum of nucleon *j*-values) as experimentally known. Scission of the Z=46, N=56~64 system was then simulated along 17 principal lattice planes cutting through or parallel to the origin of the coordinate system, and statistics collected (Figure 4).

For each scission plane, the total number of 2-nucleon "bonds" crossing the scission-plane was counted and the total Coulomb repulsion between the fragments was calculated. Assuming an average nearest-neighbor binding energy of ~2.73 MeV (ignoring spin and isospin effects) (thus giving total binding energies of the Pd isotopes within 0.1% of experimental values) and subtracting the Coulomb effect between the fragments, the fission barriers for 17 fission events per isotope were calculated. The simulation was then repeated for different (but equivalent) occupancy of surface neutron sites. Finally the data on fission fragments per Pd isotope were collated. The entire procedure for simulating the fission of Palladium is similar to that already reported concerning the actinides [4], and can be easily reproduced using the same software (NVS) that demonstrates the asymmetrical fission of Uranium and Plutonium. Examples of fission planes for Pd^{104} are shown in Figure 4.

It is worth noting that the rigid crystal structures shown in Figure 4 are merely snapshots of a highly-dynamic quantum lattice, in which meson exchanges change the isospin assignment of lattice sites, and all valence positions are repeatedly occupied and vacated, as the system settles into an energetically favored state. In this regard the quasi-classical crystal structures shown in Figure 4 are somewhat misleading. The individual nucleons are localized to lattice positions only within the limitations of the uncertainty principle, and the rigid "bonds" connecting nearest-neighbor nucleons change dynamically with collective nuclear transformations.

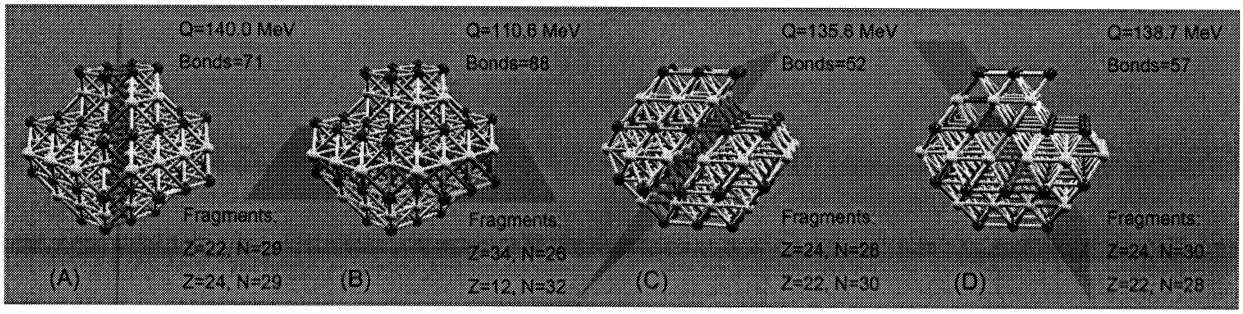

Figure 4: Examples of high fission-barrier (A, B) and low fission-barrier (C, D) lattice scission planes for Pd^{104}. Note that the fcc lattice structures represent individual nuclei (protons are light spheres, neutrons are dark spheres), unrelated to the fcc (atomic) structure of the Palladium cathode itself. Most of the low fission-barrier fragments are stable or rapidly decay to stability.

Results

By calculating the total binding energy across each scission plane minus the Coulomb repulsion between the protons in each fragment, the energy required to induce fission was found to be 1.57~11.73 MeV, depending on the specific isotope and lattice plane. The fragments produced by splitting the Pd isotope along the low-energy planes contained 48~60 nucleons and 22~24 protons. Specifically, the lowest energy fission products per isotope were: Pd^{102} (2.44 MeV) → Cr^{48} & Ti^{54}; Pd^{104} (2.25 MeV) → Cr^{50} & Ti^{54}; Pd^{105} (7.30 MeV) → Cr^{50} & Ti^{55}; Pd^{106} (1.95 MeV) → Cr^{52} & Ti^{54}; Pd^{108} (1.57 MeV) → Cr^{52} & Ti^{56}; and Pd^{110} (11.73 MeV) → Cr^{54} & Ti^{56}. Most fragments are stable, with a predominance of Cr and Ti, sometimes decaying to Mn, Fe, etc. In other words, the fission of Palladium was essentially symmetrical with two daughter fragments of

approximately the same mass. Generally, only a few scission planes per isotope had fission barriers below 10 MeV, but a higher fission barrier produces fragments with atomic number 14~32 and mass number 34~72. Qualitatively, the spectrum of deposits on Pd as reported by Mizuno [1] was reproduced by the lattice model. A quantitative study is in progress and will be reported at ICCF15 in Rome..

Conclusion

The asymmetrical fragmentation of U^{235} and all of the other semi-stable actinides that undergo thermal fission is one of the oldest, unsolved problems in conventional nuclear physics. Despite the success of the LDM in explaining the energetic basis of fission, extremely precise structural data are available and have remained, since 1938, totally ***unexplained*** using the conventional models of nuclear structure theory. In the realm of LENR, a similar dilemma exists. Since 1989, heat generation that cannot be explained on a chemical basis and precise data on isotopic changes have been demonstrated experimentally many times, but structural mechanisms concerning the transmutation of nuclear species have remained elusive. I suggest that both of these "transmutation" puzzles have straight-forward answers if the geometrical analog of the independent-particle model (i.e., the fcc model) is considered.

Understandably, conventional nuclear structure theorists are reluctant to postulate new physical mechanisms to account for the transmutation results in either the thermal fission of the actinides or the much newer LENR phenomena. Indeed, the extremely hostile reaction to the early reports of "cold fusion" is arguably the only possible response from ***theorists*** insofar as conventional quantum theory was being directly challenged. On the other hand, nuclear structure theory itself (as distinct from quantum theory) remains a highly dis-unified field in which many (>30!) mutually-contradictory models are used to predict nuclear phenomena [8]. Clearly, there is much unfinished business in terms of the nuclear force, the nuclear equation-of-state and the phase-state of nuclear matter before a truly unified theory of the nucleus will be attained.

What I suggest is that the isomorphism between the conventional IPM and the fcc lattice model indicates a way forward in understanding not only the manifest disarray of modern nuclear structure theory, but also the LENR findings of nuclear transmutations. By viewing the well-established quantal symmetries of the IPM as reflecting an underlying fcc geometry, there is quite simply no need to overhaul conventional nuclear structure physics. In this regard, the identity between the fcc model and the IPM is less revolutionary in terms of nuclear structure theory than it may at first appear to be.

The IPM is demonstrably correct in its predictions of a vast number of nuclear J-values. Similarly, the LDM is correct in its explanation of various macroscopic nuclear properties based upon a realistic, short-range nuclear force. But both of these properties of the incompatible gaseous-phase IPM and the liquid-phase LDM are reproduced in the fcc model. The fact – and it is a verifiable, geometric fact; please check this using the NVS freeware – that the symmetries of the standard IPM have a precise geometrical analog in the fcc lattice suggests that conventional theory may suffice to explain at least the transmutation data reported by Mizuno, Miley, Iwamura and others.

Both the mystery of the asymmetric fission of uranium and the mystery of transmutation of Pd have apparent solutions if the nucleus itself is regarded as a quantum lattice that reproduces the shell/subshell structure inherent to the IPM. Assuming a yet-uncertain energetic mechanism for inducing the fission of Pd nuclei [9, 10], the substructure implicit to the fcc lattice representation of nuclear symmetries can explain transmutation results essentially without any modification to the conventional independent-particle (~shell) model of nuclear structure.

References

[1] Mizuno, T. (1998) ***Nuclear Transmutation***, Infinite Energy Press, Concord, NH.

[2] Vandenbosch, R. & Huizenga, J.R. (1973) ***Nuclear Fission***, Academic, NY, p. 273.

[3] Cook, N.D., & Dallacasa, V. (1987) ***Physical Review C***36, 1883-1891

[4] Cook, N.D. (1999) ***Proceedings of the St. Andrews Conference on Fission***, pp. 217-226.

[5] Cook, N.D. (2006) ***Models of the Atomic Nucleus***, Springer, Berlin.

[6] Canuto, V., & Chitre, S.M. (1974) ***Inter. Astr. Astroph. Union Symp.*** 53, 133.

[7] Brack, M., Strutinsky, V., et al. (1972) ***Reviews of Modern Physics*** 44, 320.

[8] Greiner, W. & Maruhn, J.A. (1996) ***Nuclear Models***, Springer.

[9] Takahashi, A., et al. (1999) ***Physics Letters A*** 255, 89.

[10] Takahashi, A., et al. (2001) ***Japanese Journal of Applied Physics*** 40, 7031.

Proceedings of JCF9, March 28-29, 2009, Shizuoka-ken Sangyo Keizai Kaikan, Shizuoka, Japan

Speculation on the Relation between Condensation of Hydrogen or Deuterium in Metal by Formation of Vacancy-Hydrogen Cluster or Vacancy-Deuterium Cluster

Hidemi Miura

1-27-6 Tsurugaoka, Izumi-ku, Sendai. 981-3109, Japan

Abstract: It has been shown that the thermal equilibrium concentration of vacancy-hydrogen clusters increases rapidly as the hydrogen concentration in a metal increases to some extent, and then the diffusion rate of impurity atoms in the metal also increases. And other studies have shown us that the potential bottom of the interstitial site in which hydrogen is self-trapping moves in the direction of the next one, and then hydrogen occupies it. Considering these phenomena, this paper attempts to modify the scenario about the condensation of hydrogen or deuterium in the metal.

Keywords: vacancy-hydrogen or vacancy-deuterium cluster, diffusion, alkali or alkaline-earth metal ion, condensation

1. Introduction

Nuclear reactions in condensed matter such as nuclear fusion and nuclear transmutation have been reported in the experiments of the electrolysis of heavy water using the cathode of face-centered cubic (fcc) lattice metals such as Pd, the penetration of D_2 gas using thin films and the absorption of D_2 gas using nano-particles. Moreover, the nuclear transmutation has also reported in the electrolysis of light water. Those occur near the surface in the host metal.

In some theories trying to explain the condensed matter nuclear reactions, Takahashi's cluster nuclear reaction theories are interesting.[1,2] In the theories of not only Takahashi's but also many other ones, since nuclear reactions occur within condensed matter such as metals, it is required for more than one hydrogen or deuterium to gather and condense in the narrow domain of the host metal.

However, it has not seemed to be clear what kinds of mechanisms arise, then we have tried modeling of the mechanisms.[3,4] This time, we tried to modify the scenario about the condensation of hydrogen or deuterium in the metal to cause the nuclear reactions.

2. Formation of Vacancy-Hydrogen Clusters or Vacancy-Deuterium Clusters and Diffusion of Metal Ions, etc.

2.1 Formation of Vacancy-Hydrogen clusters or Vacancy-Deuterium Clusters within the Host Metal

H/D atom permeates into metals as an ion with the voltage of electrolysis, the gas pressure of gas penetration, etc. H^+/D^+ ions which permeated into the fcc lattice metals such as Pd enter O sites at room temperature, and then self-trap in it.

Other studies on the interaction between hydrogen and vacancies within various metals have been established systematically in relation to wall materials of thermonuclear fusion reactors, and following results are shown.[5]

- A vacancy traps more than one H atoms (a maximum of six atoms).
- Binding energies of trapped atoms are quite large.

Especially, those for two of the beginnings are large and those for three or more atoms become smaller a little.

- The H atoms trapped around the vacancy are slightly shifted to it from the usual interstitial position.
- When vacancies trap H atoms, generation energy of them falls, and many vacancy-hydrogen clusters are formed, then the thermal equilibrium concentration of vacancies increases.
- Vacancy-hydrogen clusters are made from the surface of the host metal or voids in it. They are promptly spread and uniformly distributed in it by the latter.

These should be realized not only to hydrogen but also to deuterium. Then, vacancy-hydrogen clusters or vacancy-deuterium clusters are formed from voids etc. in those host metals with H/D atoms permeated in it.

Usually, the diffusion of impurity atoms within the host metal takes place through vacancies. Then, since the diffusion under existence of interstitial hydrogen will take place through vacancy-hydrogen clusters, the diffusion of impurity atoms will be promoted, and this has been confirmed also in experiments.[5)]

Therefore, when vacancies are formed as vacancy-hydrogen clusters or vacancy-deuterium clusters in the host metal such as Pd, and they are spread and distributed in it, not only H^+/D^+ ions which can diffuse through the interstitial sites of the host metal but also alkali or alkaline-earth metal ions such as Li^+, Ca^{2+} ions which has permeated into the host metal with the action of electrolytic voltage or penetration gas pressure, further also helium etc. generated by nuclear reactions in it, could raise their diffusion rate.

In addition, the positive formation energy of vacancy-hydrogen clusters and nearly-zero dissolution energy of hydrogen are reported by the first principle molecular dynamics calculation for Pd.[6)]

These suggest that the vacancy-hydrogen clusters or vacancy-deuterium clusters are formed in Pd by external energy and H^+/D^+ ions are taken in it as intermediate states, then they can be efficiently supplied to the next condensation process.

2.2 Change of Lattice Potential

When H^+/D^+ ions or alkali / alkaline-earth metal ions etc. diffuse and move in the host metal, the surrounding lattices in which H^+/D^+ ions are self-trapping would be distorted, and then the repulsion potential barrier of the metal lattice would be affected.

The following studies how impurity atoms inside metals move when external force is applied to it have been established relating to the body-centered cubic (bcc) lattice metal such as Fe.[5)]

- Movement simulation of the self-trap potential:

The potential bottom of the interstitial site in which a H atom is self-trapping moves to the next one (from a T site to an O site in bcc lattice) by the tensile stress, and the potential bottoms of both interstitial sites become wide and combined, then finally the H atom changes the interstitial site which it occupies. The situation of such a potential change is shown in Fig. 1.

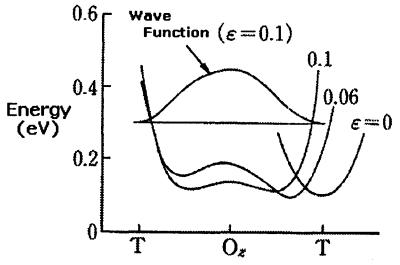

This shows a situation that a self-trap state moves to an O site thorough displaced T site from a T site by extending one axis of a bcc lattice. The extension rate is denoted by ε. [H. Sugimoto: J. Phys. Soc. Japan, 53 (1984), 2592]

Fig. 1: Situation of potential change

[Fukai, Tanaka and Uchida, Metal and Hydrogen]

This should be realized not only to hydrogen but also to deuterium, and further also to the interstitial sites of the fcc lattice metal such as Pd or vacancy-hydrogen clusters or vacancy-deuterium clusters. Further it would be possible to replace the tensile stress with the reduction of internal pressure. Then, when a H^+/D^+ ion or an alkali / alkaline-earth metal ion hops-into a interstitial T site or a vacancy of the host metal such as Pd and hops-out again, since the internal pressure which has acted inside of it then falls, and the surrounding energy of it decreases (reduction of the energy by a Wallis model).

This suggests that the potential bottoms of the O sites in which surrounding H^+/D^+ ions are self-trapping would move in the direction of the T site or the vacancy, and these cluster H^+/D^+ ions of the vertexes of the regular tetrahedron or the regular octahedron move and condense into it, respectively.

3. Distortion of the Host Metal Lattice and Condensation of H^+/D^+ Ions by the Hopping-out of Metal Ion etc..

3.1 Regular Tetrahedrons of the Host Metal Atoms and Surrounding Vacancy-Hydrogen Clusters or Vacancy-Deuterium Clusters

In the metal of fcc lattice structure, such as Pd, if there is a vacancy per one crystal unit and H^+/D^+ ions fill all O sites, the composition of the lattice atoms is shown as M_3VacH_4/D_4 (M: atom of the metal with fcc lattice structure; Vac: vacancy). By the calculation about Pd, it is reported that the composition energy of Pd_3VacH_4 (a ratio of vacancy: 1/4) becomes lower than that of 1 hydrogenate, PdH.[5] Although this composition can have a regular cyclic structure, the regular tetrahedron of the host metal atoms, in which H^+/D^+ ions would condense, cannot exist.

Fig. 2 shows the regular tetrahedron of the host metal atoms such as Pd and the somewhat large regular tetrahedron circumscribed to it. The host metal of fcc lattice, such as Pd, in which the cluster H^+/D^+ ions should condense into a T site or a vacancy to cause nuclear reactions, would compose the structure in which vacancy-hydrogen clusters or vacancy-deuterium clusters are located in the surrounding lattice of the regular tetrahedron of the host metal atoms centering the T site. One of those crystal structures is the periodic pattern of the basic structure that has a vacancy replaced with one of the vertexes of the triangle section of octahedron which are cut off four vertex portions of the somewhat large regular tetrahedron circumscribed with the regular tetrahedron of the host metal atoms. This basic structure has 1.5 × 1.5 × 1.5 lattice units as shown in Fig. 2. The composition of this lattice atoms is $Pd_{3.5}Vac_{0.5}H_4$ (a partial ratio of vacancies: 0.5/4), and the regularity of it decreases than the case of the structure of Pd_3VacH_4.

Moreover, another crystal structure in which the concentration of vacancies is higher than it, would be the periodic pattern of the aforementioned large regular tetrahedrons mutually overlapping except the small regular tetrahedron (a ratio of vacancies: ~0.944/4).

These crystal structures have half or slightly few vacancies in the ratio compared with the case of Pd_3VacH_4/D_4 (a ratio of vacancies: 1/4) which is probably more stable than PdH/D.

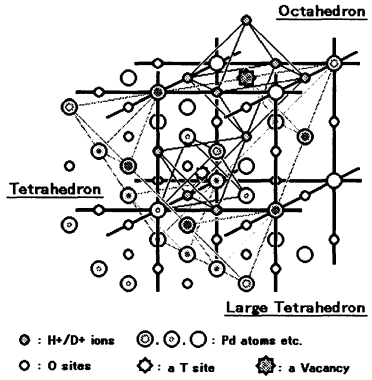

Fig. 2: Regular tetrahedron of Pd etc. and
Large regular tetrahedron circumscribed to it

3.2 Condensation of Cluster H^+/D^+ Ions

In the host metal such as Pd, when H^+/D^+ ion or alkali / alkaline-earth metal ion hops-into a T site or a vacancy and hops-out again, the potential bottoms of O sites in which H^+/D^+ ions are weakly bound as a vacancy-hydrogen cluster or a vacancy-deuterium cluster should move in the direction of the T site or the vacancy, and then these cluster H^+/D^+ ions located at the vertexes of the regular tetrahedron or regular octahedron should condense, respectively. Fig. 3 shows these condensation processes of H^+/D^+ ions to the T site in simpler scheme:

① Self-trapping of H^+/D^+ ions,

② Formation of vacancy-hydrogen clusters or vacancy- deuterium clusters,

③ Hopping-into the T site of an ion such as H^+/D^+ ion or alkali / alkaline-earth metal ion,

④ Hopping-out the T site or vacancy of the ion causing distortion of surrounding lattices,

⑤ Movement of the surrounding H^+/D^+ ions of it in the direction of the T site,

⑥ Condensation of the H^+/D^+ ions. (To shield the Coulomb repulsion force is the next problem.)

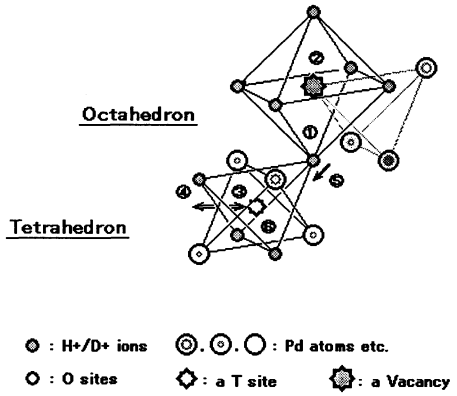

Fig. 3: Condensation processes of H^+/D^+ ions

In order to evaluate these processes correctly, it is necessary to perform computer simulations that will become our next works. At that time, we will check the fundamental processes of the proton/deuteron movement in the tetrahedron or octahedron covered with non-crystal matter, namely vacancies, of nano-particles and glassy alloyes[7,8].

4. Conclusion

We considered the model about the condensation of H^+/D^+ ions that cause nuclear reactions within the host metal of fcc lattice, such as Pd, although it is still an early stage. We speculated that the formation of vacancy-hydrogen clusters or vacancy-deuterium clusters promotes the diffusion of H^+/D^+ ions or alkali / alkaline-earth metal ions in the regular tetrahedron or regular octahedron of the host metal lattice to cause the nuclear reactions.

The main considerations in this work are based on the analogy from the study on the H in the metals of bcc lattice, such as Fe, in relation to thermonuclear fusion reactor material, then it is necessary to establish the study on the H/D in the metals of fcc lattice, such as Pd, to clear the mechanisms of nuclear fusion and nuclear transmutation within them.

Acknowledgements

The author wishes to thank Professor Takahashi of Osaka University and Professor Fukuhara of Tohoku University for valuable information and advice.

References

1) A. Takahashi, Deuteron cluster fusion and related nuclear reaction in metal-deuterium/hydrogen systems, Recent Res. Devel. Phys. 6, 1-28 (2005).
2) A. Takahashi, Chronicle of Condensed Cluster Fusion Models, Proc. of 8th Meeting of Japan CF Research Society, p. 51 (2007).
3) H. Miura, Study on Formation of Tetrahedral or Octahedral Symmetric Condensation by Hopping of Alkali or Alkaline-earth Metal Ion, Proc. of 12th International Conference on Cold Fusion, p. 536 (2005).
4) H. Miura, Formation of Tetrahedral, Octahedral or Hexahedral Symmetric Condensation by Hopping of Alkali or Alkaline-earth Metal Ion, Proc. of 7th Meeting of Japan CF Research Society, p. 79 (2006).
5) Y. Fukai, K. Tanaka and H. Uchida, Hydrogen and Metal (Uchida Roukakuho).
6) D. Kato, First Principle Molecular Dynamical Approach to the Behavior of Hydrogen Multi-Trapped to Metal Vacancies, Annual Meeting of Atomic Energy Society of Japan, (autumn 2007), http://dpc.nifs.ac.jp/amdrc/J/dkato_genshigaku070929web.pdf.
7) M. Fukuhara, New Approach to the Theory of Cold Nuclear Transmutation, Proc. of 8th Meeting of Japan CF Research Society, p. 36 (2007).
8) M. Fukuhara and A. Inoue, Room temperature Coulomb oscillation of a proton dot in Ni-Nb-Zr-H glassy alloy with nanofarad capacitance, J. Applied Physics, p. 1 (2009).

Proceedings of JCF9, March 28-29, 2009, Shizuoka-ken Sangyo Keizai Kaikan, Shizuoka, Japan

Neutron Spectra in CMNS
- Back to the Past –

Akito Takahashi
Technova Inc.: akito@sutv.zaq.ne.jp

The recent SPAWAR claim on $^{12}C(n,n')3\alpha$ detection due to 14 MeV neutrons by D-T reaction in D_2O/Pd co-deposition cell reminds our old discussion on observed neutron spectra from CMNS/CF cells in the past. Structure or shape of neutron spectra should give important (decisive) evidences on underlying physical mechanisms on possible deuteron-related nuclear fusions in PdDx systems. This paper discusses plausible neutron spectra as consequences of major theoretical model predictions to be compared with our past neutron emission data from CF cells.

1. Introduction

The recent SPAWAR claim[1] on $^{12}C(n,n')3\alpha$ detection due to 14 MeV neutrons by D-T reaction in D_2O/Pd co-deposition cell reminds our old discussion on observed neutron spectra from CMNS/CF cells in the past. In our past experimental data[2-6], neutron emission rates were negligibly small (on the order of 10^{-10} or less) compared to excess heat events as regarded as nuclear origin, but observed neutron spectra having two components provided us important information on underlying physical mechanisms of condensed matter nuclear effects (often called as cold fusion, CF).

Theoretical models of CMNS/CF mechanisms shall assert their own nuclear reactions as consequences of physical consistencies to predict possible specific forms of energy spectra of emitted neutrons, which would be primary or secondary reactions. Therefore, to identify emitted neutron energies from CMNS/CF cells by experiments can verify which theoretical models are in consistent with experimental facts.

2. The SPAWAR claim

Mosier-Boss et al. have observed triplet tracks in CR39 detectors used in their co-deposition Pd/D_2O electrolysis type CMNS/CF experiments[1]. They claimed the triplet tracks should be due to forward-peaked emission of three alpha-particles from $^{12}C(n,n')3\alpha$ reactions by D+T fusion reactions as byproducts of D+D reactions in the co-deposition experiments. The $^{12}C(n,n')3\alpha$ reaction has however threshold at 7.8MeV of incident neutron energy[7]. And the threshold for the first α emission is 6.2MeV of neutron energy. We need careful study of α emission.

The author conceives that the explanation by secondary d+t reactions after d+d fusions is not plausible, because the yield of d+t reactions by one 1MeV triton slowing down in PdDx matter is very small on the order of 10^{-5},

$d + d \rightarrow p(3.015MeV) + t\ (1.005MeV) + 4.02MeV$

for conventional fusion.

Estimation using available neutron cross sections (JEDL3 for instance)[7], one $^{12}C(n, n')3\alpha$ event needs about 100 fluence of 14MeV neutrons getting into the used CR39 track detector by SPAWAR.

This should correspond to 10^7 neutrons of 2.45MeV by d+d reactions. If we had 10^7 neutrons emitted from CF cells, we could detect very easily significant counting events and their recoil-proton-tracks of 2.45MeV

neutrons. This can easily be detected, but has never been observed with so high 2.45 MeV neutron yield.

The author concerns that the conclusion of secondary D+T fusion by SPAWAR for triplet tracks is not plausible.

3. Model Prediction Case-1

[Case-1]: Some theoretical models[8-11] conceiving the d+d to ^{4}He + lattice energy (23.8MeV) processes have been thought as possible explanation for the CMNS/CF phenomena since 1989, in spite of very negative view from the nuclear physics point of view[12].

If the "Dream" of the **"d+d to ^{4}He + lattice energy (23.8MeV)"** [8-12] were taking place, the doping tritons make "d+t to ^{5}He + lattice energy" reactions, in the same path and we shall have neutron emission by,

- ^{5}He → n(0.716MeV) + ^{4}He(0.179MeV)

14 MeV neutrons are not major products in consequence of this theoretical model, but **low energy neutrons (0.716 MeV)** should be detected with the tritium doping of micro-Curie/cc-DTO; doping in experimental CMNS/CF cells. These "low" energy neutrons could not be detected by CR39 because recoil-proton energies are too small to cause enough large ionization tracks. We shall use special neutron spectroscopy system which is recommended in the later section.

4. Model Prediction Case-2

[Case-2]: Our **4D/TSC fusion model**[13-15] predicts 23.8MeV/^{4}He energy deposit in PdDx lattice as major product by the major channel 4D → ^{4}He + ^{4}He + 47.6MeV reactions. Minor branch products of triton and higher energy neutrons from 4D fusion are predicted as,

- ^{8}Be*(47.6MeV) → t(En<16.2MeV) + ^{5}Li(Ex) + (28.7MeV – Ex)
- ^{8}Be*(47.6MeV) → **n(En<25.1MeV)** + ^{7}Be*(Ex) + (28.7MeV – Ex)

If we make a doping of tritium (on the level of micro Curie) in the process, (3D+T)/TSC makes ^{9}Be*(43.01MeV) intermediate compound state to break up as,

- ^{9}Be*(43.01MeV) → ^{4}He(22.53MeV) + ^{5}He(18.01MeV)
- ^{5}He → n + ^{4}He + 0.895MeV (for ^{5}He at rest)

Neutron energy appears in 0.41 to 6.79 MeV (emitted from the break up of moving ^{5}He of 18.01MeV kinetic energy, as calculated by kinematics).

Other minor high energy component will come from,

- ^{9}Be*(43.01MeV) → n + ^{8}Be*(Ex) + (41.36MeV- Ex)

This process emits neutrons in 0-36.75 MeV region.

We may predict the broad higher energy spectrum in 0.4 to 7MeV region as major component (minor component in much higher energy region) by the tritium doping into on-going CMNS/CF cell experiments. This is the consequence of TSC model[13-15].

Obviously we can verify which theoretical model, Case-1 or Case-2 matches the observed phenomena of neutron emission in CMNS/CF experiments.

5. Our Past Data of Neutron Emission

We refer now our past measurements[2-6] of neutron spectra from CF-electrolysis experiments to be discussed under the above predictions.

A typical result of measured neutron spectra from Pd/D_2O electrolysis cell[2] is copied in Fig.1. Fast neutron spectroscopy was done by measuring

recoil-proton pulse height distribution of NE213 liquid scintillator with n-gamma pulse shape separation technique[4]. The background spectrum has "near-exponentially decreasing" recoil-proton pulse height distribution which was of spallation neutrons of cosmic-ray-origin showing similar spectrum as fission-neutrons to have near Maxwellian distribution with nuclear temperature 1.4MeV. High energy protons by cosmic rays induce spallation reactions in matter surrounding the detector. The near Maxwellian spectrum has therefore high energy tail in En>10MeV.

The excess neutrons observed has two components in its energy spectrum: one is of 2.45 MeV neutrons, very probably by the D+D fusion reactions. The other broad component in the 3-7 MeV region (and we might expect higher energy- more than 7 MeV- tail to observe if statistics of experiment is improved) is unidentified origin (See Fig.1).

In our past papers[2,3,16], we speculated that the higher energy component was the product of secondary high energy d+d reactions after the primary d+d+d three body fusion in PdDx-lattice;

$$D+D+D \rightarrow d(15.9MeV) + {}^4He(7.9MeV)$$

In the slowing down process of 15.9MeV deuterons, d+d reactions in PdDx produce higher energy component of neutrons seen in the 3-10MeV region.

Now, we have to reconsider this explanation by referring our other past results shown in Fig.2.

In our reconsideration, the higher energy neutron component might have been the 0.4-7MeV neutron emission by the (3D+T)/TSC 4-body fusion reaction in PdDx lattice dynamics (Case-2), because we had seen the significant accumulation of tritium atoms in the electrolyte (curve c) in Fig.2): This was already a kind of T-doped experiment which happened by chance.

4D fusion may emit much higher energy neutrons than 7 MeV, from minor out-going channels, as already pointed out.

6. Recommendation for Neutron Measurements

Identification of emitted neutron energy in CMNS/CF experiments is very important to have hints on underlying physical mechanism of excess heat generation with ^4He major ash, although neutron emission channel is conceived to be very much minor channels. For identifying emitted neutron energies, the following techniques may be recommended.

A) For 14 MeV, and 1-10 MeV and higher energetic neutron emission

- Use NE213 Xylene-based liquid scintillator with n-gamma pulse shape separation
- Measure recoil proton pulse height distribution and unfold to neutron-spectrum

B) For 0.716MeV or less-energetic neutron emission

- Recoil proton proportional counter to measure pulse height distribution to unfold to neutron spectrum
- He-3 counter with Cd filter (about 1mm thick) and without moderator to measure pulse height peak at (762+716keV)
- Cross check between NE213 counting and He-3 counting with moderator will be also useful. If we do have low energy (<0.8MeV) neutron emission only, we should have counts only for He-3 counter.

However, we have to be careful for high energy tail (En>8MeV) of spallation neutrons in natural background which may also cause triplet tracks in CR39 detection.

Acknowledgment: The author thanks for discussions via internet (cmns-google group), especially Mr.

Horace Heffner.

References:

1) P. Mosier-Boss, S. Szpak, F. Gordon, L. Forsley: Naturwissenschaften, 96(2009)135-142
2) A. Takahashi, T.Takeuchi, T. Iida, M. Watanabe: J. Nuclear Science and Technology, 27 (1990)663-666
3) A. Takahashi, T. Takeuchi, T. Iida, M. Watanabe: AIP Conf. Proc. 228 (1990)323-340
4) A. Takahashi, T. Iida, F. Maekawa, H. Sugimoto, S. Yoshida: Fusion Technology, 19(1991)380-390
5) A. Takahashi, T. Iida, T. Takeuchi, A. Mega: Int. J. Appl. Electromagnetics in Materials, 3(1992)221-230
6) A. Takahashi, H. Fukuoka, K. Yasuda, M. Taniguchi: Int. J. Soc. Material Eng. For Resources, 6(1998)4-13
7) K. Kondo, I. Murata, K..Ochiai, N. Kubota, H. Miyamaru, C. Konno, T. Nishitani: J. Nucl. Sci. Technol., 45(2008)103-115
8) G. Preparata: Trans. Fusion Technology, 26(1994)397-407
9) P. Hagelstein: Condensed Matter Nuclear Science, ICCF12, World Scientific, pp.441-453 (2006)
10) S. Chubb: ibid., pp.646-664
11) M. Swartz: Fusion Technology, 31(1997)228-236
12) A. Takahashi, N. Yabuuchi: Condensed Matter Nuclear Science, ICCF13, Moscow, ISBN=978-5-93271-428-7, pp.569-578 (2008)
13) A. Takahashi, N. Yabuuchi: LENR Source Book, American Chemical Soc., ACS Symp. Series 998, pp.57-83 (2008)
14) A. Takahashi: "Basics of Deuteron Cluster Dynamics by Langevin Equation", LENR Source Book 2, American Chemical Society, to be appeared in 2009
15) A. Takahashi: "Cold Fusion 2008- Mechanism of Condensed Cluster Fusion", (in Japanese), Kogakusha, Tokyo, ISBN=978-4-7775-1361-1 (2008)
16) A. Takahashi, T. Iida, T. Takeuchi, A. Mega, S. Yoshida, M. Watanabe: The Science of Cold Fusion (ed.; T. Bressani, E.D. Giudice, G. Preparata), Proc. ACCF2, Italian Physical Soc., pp.93-97 (1991)

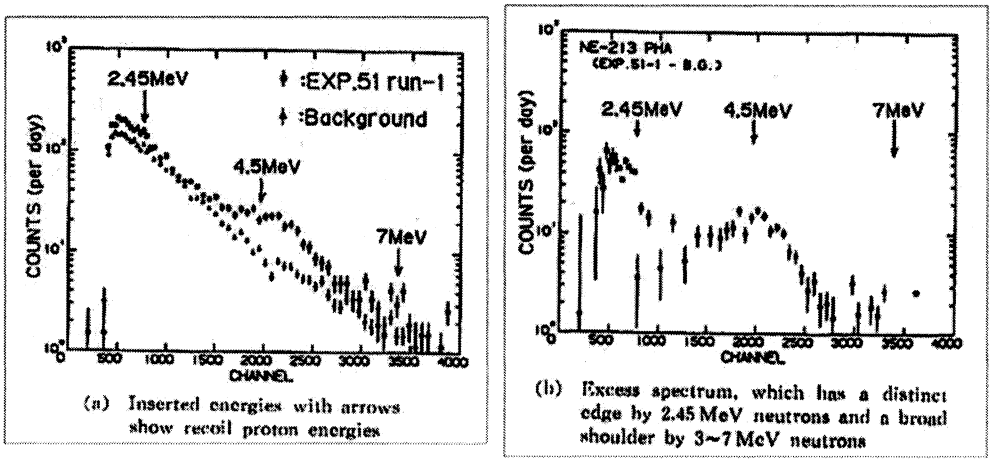

Two components: 2.45MeV peak and 3-7 MeV Higher Energy Group

Fig.1: Two component neutron spectra observed by the past Pd/D_2O electrolysis experiments, copied from published paper[2)]

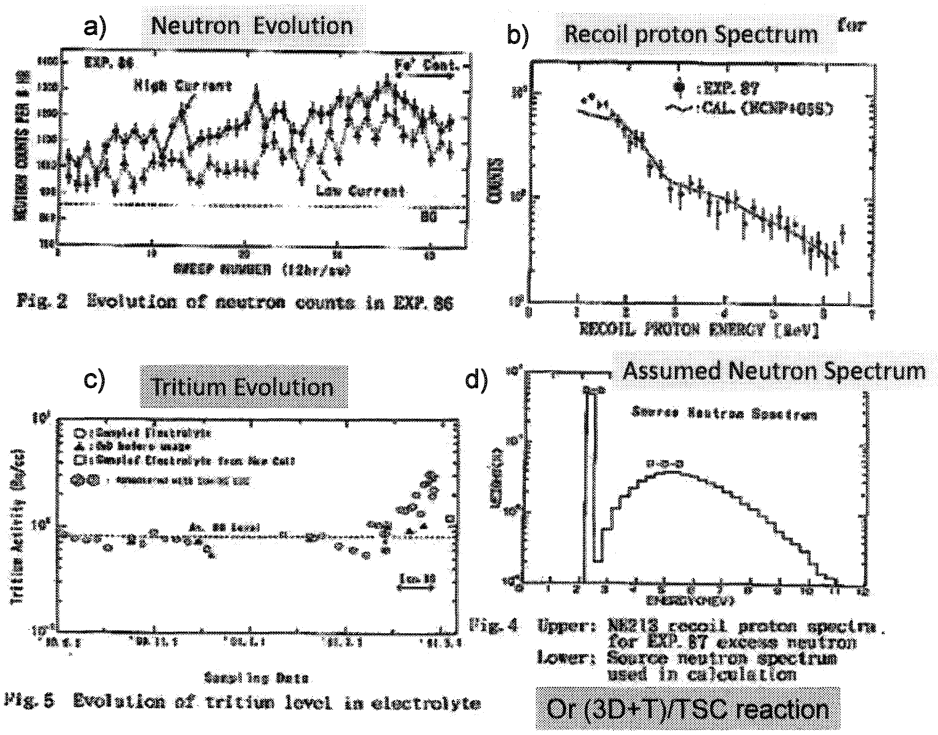

Fig. 2 Evolution of neutron counts in EXP. 86

Fig. 4 Upper: NE213 recoil proton spectra for EXP. 87 excess neutron
Lower: Source neutron spectrum used in calculation

Fig. 5 Evolution of tritium level in electrolyte

Fig.2: Our past data, copied from published prints[3,16], of neutron emission and evolution of tritium concentration in Pd/D_2O pulsed electrolysis experiments; a) evolution of excess neutron counts, b) recoil-proton pulse height spectra for excess neutrons, c) evolution of tritium concentration measured by LSC with sample electrolyte and d) assumed two component neutron spectrum for folding calculation of model.

Proceedings of JCF9, March 28-29, 2009, Shizuoka-ken Sangyo Keizai Kaikan, Shizuoka, Japan

Numerical simulation of vortex pattern appeared on electrode surface after long term electrolysis of well annealed thick Pd rod in 0.1M LiOD: Open boundary condition

H. NUMATA: numata.h.aa@m.titech.ac.jp
Tokyo Institute of Technology, 2-12-1, O-okayama, Meguro Tokyo 152-8552 Japan
M. BAN: ban.masanobu@hikaku.metro.tokyo.jp
Tokyo Metropolitan Leather Technology Center, 3-13-14, Higashi Sumida, Sumida Tokyo 131-0042 Japan

Abstract: During long term electrolysis for well annealed thick Pd rod (9.0 mm dia.) in 0.1M LiOD vortex patterns were observed. This vortex pattern was proved that the hypothetical particles mass flow coincidently through the electrode surface/electrolyte interface using Lattice Gas Cellular Automata (LGCA) numerical simulation method. During this experimental series PC computational power was improved. On the other hand, three boundary conditions for the Outflow boundary were examined numerically in a 2D flow using LGCA method. The results showed that a vortex behind a flat plate (t = 10000 step) was obtained in the downstream. Only Sommerfelt's radiation condition for BC can be applied resulting in reasonable flow. This simulation revealed that this BC is effective for rendering the harmful behaviors masked.

Keyword: Computational fluid dynamics, Lattice gas cellular automata, Pd, Nuclear reaction cycle model, Vortex, Cold fusion, Boundary condition

1 Introduction

During long-term electrolysis for well annealed thick Pd rod (9.0 mmϕ) in 0.1M LiOD vortex pattern was observed [1-2]. The morphology of the postelectrolysis electrodes revealed that there were appeared two long faults but without any cracking on the surface. The original work of the modified cellular automata (numerical simulation) method had been first applied by Numata et al. to the study of the cold fusion and related phenomena.[3-5] Our research goal is to give an atomistic understanding of the process that the vortex occurred on a Pd electrode surface after long-term electrolysis in 0.1 M LiOD. This vortex pattern was successfully formed by FHP-III model of LGCA method. Then it was proved that the hypothetical particles mass flows coincidently through the electrode surface/electrolyte interface under the influence of heterogeneous induced magnetic field in the vicinity of the electrode surface area.

The LGCA methods have been developed to simulate microscopic fluid flow and estimate macroscopic properties of homogenous single phase media placing an obstacle, such as a plate in a 2D-test region[6]. Instead of the Quantum mechanical realization of cold fusion process, the work has found the microscopic mechanism: how the hypothetical particles mass having significant kinetic energy moved and has left the vortices on the sample surface[3]. However there is still remained ambiguous with respect to the pattern of the fluid flow past a solid plate, which directly determines the results of the simulation. The coding of boundary conditions (BC) is known as an essential part of LGCA method. Especially, Outflow BC is seemed to be difficult concern for application of macroscopic values obtained by hydrodynamic simulation to real fluid flow characteristics.

In this paper recent development of PC computational power (Linux platform and vectorization) is reported. Further three open boundary conditions as Outflow one are compared numerically in a 2D fluid flow using LGCA method.

2 Experimental

2.1 Improved Simulator performance for numerical simulation

As an integrated CA simulator, we have made LGCA programs run on Linux platform. The CentOS5 software is used and the code is written in C. As GUI we installed "Gnuplot" graphics library for Linux that can be obtained as the archives file from web site.

First, the benchmark: Himeno benchmark was run under different ordinary PC speculations to evaluate the speed of the incompressive fluid analysis code. This code (calculation size fixed at S) is very simple to measure speed of computation in MFLOPS. (Table1) The test results show that the larger the CPU clock, somewhat accompanied with the memory size, the faster the computational speed. In this experimental series, CA simulation environment, Windows was at first implemented. As shown in Table 1 we have obtained satisfactorily level of CA simulator on Linux exhibiting rank 1 (1325.42 MFLOPS) through vectorization and parallelization (not yet).

The implementation of CA simulation program: LGROTATE designed for Linux has been conducted; source code written in C will be also converted to Java because of its advantages: compatible with NET environment and complete graphical library for users. In the CA calculation each cell on the lattice is simultaneously renewed based on a single update rule, therefore, some approaches with parallel systems can be expected for more efficient computation.

2.2 Basics of LGCA simulation model

The following more details notes can be skipped in a first reading. Lattice gas cellular automata are discrete models of fluids. A fluid is modeled by identical moving particles (essentially fluid elements consisting macroscopic fluid) set regularly in lattice whose time evolutions are represented by a discrete time step. This simulation method for fluids was proved to be identical to the kinetic equation: Navier-Stokes equation.

1. The model is FHP-III model of lattice gas automata.
2. Type of simulation model is two-dimensional of a single-phase flow in homogeneous media.
3. Boundary conditions are no-slip boundary conditions for wall and constant pressure boundary conditions for Outflow and Inflow boundaries in some case.
4. The direction of the particles movement started from the source of the initial flow (left sides (Inflow) to the right sides (Outflow) as shown in Fig.4) and follows the collision rules.
5. Evolution of particles for each time step consists of propagation and collision steps.
6. Mass and momentum are conserved.
7. Simulation results are displayed in window environment.

Flowchart of the computer programme is shown in Fig.1.

2.3 Coding of BC in 2D incommpresive fluid flow simulation

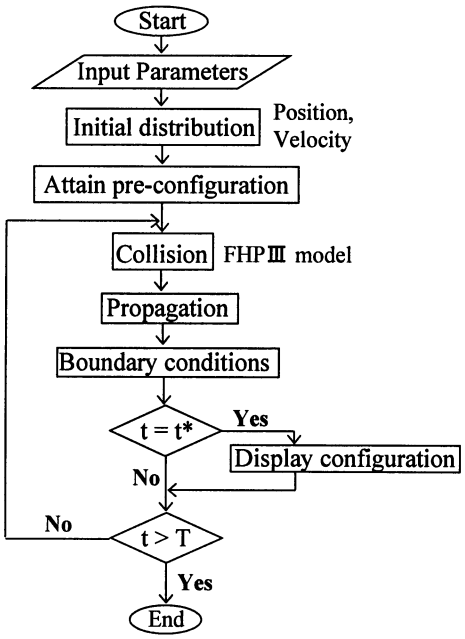

Fig.1 Computational flow chart of fluid flow simulation in homogeneous single media using LGCA.

There are at least five different types of Boundary conditions (BC): Periodic, Inflow, Outflow, No-slip or rebounding and Slip BC. The coding of a given model first adopts either or both of two BC types: von Neumann and Dirichlet BC. Next we initially label certain lattice sites as boundaries. Thus a domain encompasses the boundary regions and an inner region, and on the boundaries renewed BC conditions are imposed to reflect next calculation result. (Fig.4) Whether the boundary sites are included within a routine calculation step or not is depended on the given model. In reality most appropriate BC could be derived from trial and error performance. Our Inflow and Outflow BC regions consist of ghost cells and those adjacent inner region where every calculation result is imposed to fix velocity or density of particles (also see Fig.1).

3 Results and Discussion

3.1 Nuclear reaction cycle model

So far, endeavors have been exerted on understanding the individual phenomenon accompanied with cold fusion reaction, which are a complicated phenomenon as a whole. Under such an idea, by considering phenomena as an energy engine, N-cycle model[1-3] was proposed from a point of view of its continuous operation (4 reciprocating cycle). It consists of 4 sequential processes: in-taking and compression--triggering--reaction--scavenging, taking into account of the correspondence to long-term electrolysis of a thick rod Pd. (Fig.2) The following two key points are beneficially realized: (1) enhanced reproducibility of the experiments resides in continuation of the cycle (2) on systematic consideration the hindered factors might come to the surface.

Let the correspondence be examined with the model in question to the phenomena of the cold fusion experiment. In the absorption and compression processes of the reactants of the reaction (Fig.2), a barrier layer of deuterium migration by compression stress is formed as absorption in progress, resulting in formation of a

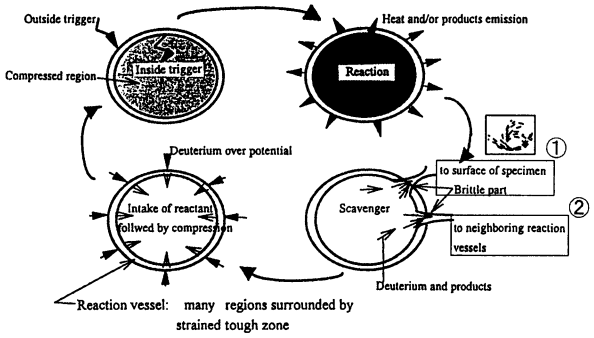

Fig.2 Schematics of nuclear reaction model.

vessel composed of the interior and blanket as the barrier layer. In the compression process, the interior appears to make expansion owing to the continued absorption, i.e., a part of the generated deuterium is contributed to further slow absorption. However, the compression pressure of the blanket brings an increase of the internal pressure (in otherwise an increase in stress) due to a kind of enhanced pinch effect. In the reaction process a reaction should be caused by an external trigger that is applied to the inside (i.e., injection of high energy particles from the outside) or by an internal trigger.[2, 7] Very many holes concentrated on both the sides of the fault found in the experiment[2] were discharge ports of the reaction products in the process of scavenging. At this stage, discharge is made with the products of the reaction together with unreacting deuterium[7-8].

The following details can make relationships clear between these individual processes and the experimental observations. The resulting ca. 6% expansion confirmed during 1st run (also see the left of Fig.3)[1-2, 9-10] suggests the occurrence of considerable internal pressure increase corresponding to the absorption/compression process of N-cycle model. Apart from the identification of the reaction vessels and emitted particles, the subsequent Outflow of the hypothetical particle mass (once these particles were defined as charged particles, deuterium or reaction products) might occur toward 360° radial direction as the scavenger process of N-cycle model (also see the right of Fig.3). Such motions of the particles mass might be realized from the geometry of the reaction vessel formed during the absorption/compression process shown in the left. That is, in a long prism crystal absorbed reaction products or deuterium under high pressure coincidently spout out with sufficient energy where the motion of the flows are expressed as 'simulate flow' vectors normal to the electrode interface as shown in the right. Furthermore all the flows synchronize with the occurrence of the reactions. It is known that nuclear reaction instantaneously occurs during which the hypothetical particles surrounding the site coincidently gain momentum converted by the energy of force evolved multiplied by time in an

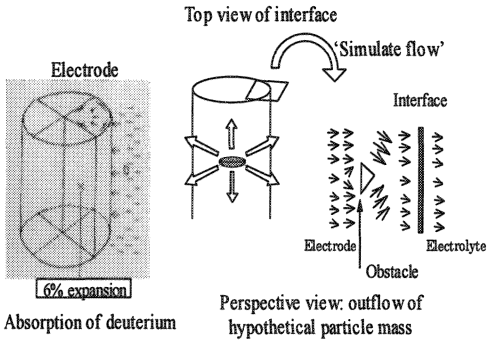

Fig.3 Absorption of deuterium and resultant Outflow of hypothetical particles mass.

adiabatic sense. In addition obstacles might be embedded under beneath the surface due to inhomogeneity. Thus, N-cycle model predicts that the flows occur coincidently through the electrode/electrolyte interface (above shown in Fig.2 as the motion of reaction products and deuterium to neighboring vessels: ② and/or surface of the electrode: ①), however, phenomenological evidence has not yet been shown, which is substantiated next by numerical simulation of the fluid flow.

3.2 Numerical simulation for hypothetical particles mass motion BC: particle generation and disappearance

Ever since N-cycle model predicted the hypothetical particles mass explosively spouted out from the deuterated Pd surface after long-term deuterium evolution, it is required to simulate the vortex pattern on the Pd surface by computer simulation. In Scavenger process of Fig.2 there appeared alternative two mechanisms of the hypothetical particles mass motions. First, ① indicated in the figure togetherwith the insertion showing the vortex pattern means the fluid of these particles mass occasionally had left the locus on the Pd surface, named as vortex. Previous report[3] mainly concerned with the morphological identification of the vortex comparing between the vortex pattern observed and that formed by 2D LGCA simulation. Further consideration had led to the physical view that the motion was fully understood by the influence of the electromagnetic interaction at the electrode/electrolyte interface. The more detailed interaction between the motion of the hypothetical particles mass and the interface magnetic field is skipped in this context[3].

As is shown in Fig.4 a 2D incompressive fluid lattice gas cellular automata is constructed on a simulating space (a rectangular domain) where

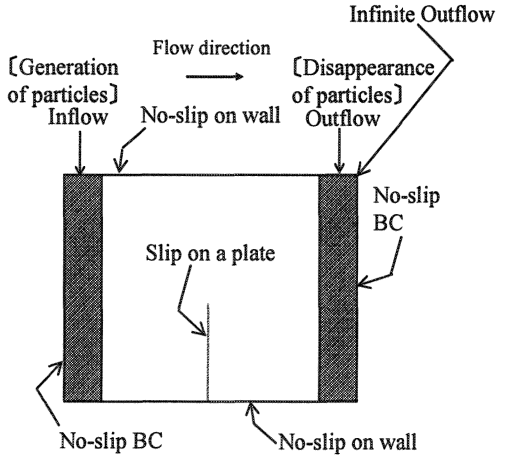

Fig.4 Schematic model of a rectangular domain with Inflow and Outflow boundaries. Obstacle is located at the center.

regular triangular lattices with unit link length are mapped and discredited on the whole. These configuration and the boundaries are essentially identical to those reported previously except that the lattice size and time step of computation are totally increased this time. Figure 5 shows a simulated fluid flow past an obstacle (flat plate) at t = 10000 by using FHP III model in the rectangular domain. The parameters used are listed in Table2. The stationary flow from left to right is given by the pressure difference of the Inflow and Outflow boundary regions. (refer Ref. 11 for boundary conditions) This simulation shows that the flow creates a vortex behind a flat plate as shown in the area pointed with an arrow. In this case the flat plate is considered as an obstacle for a first approximation. Although finer simulation is needed to fully describe the phenomenon, it is shown that a vortex exists in the downstream as shown in Fig.5.

On the other hand, inspecting the fluid flow vectors in the downstream there obtained the counter flow generated at the Outflow boundary region. When simulation time was prolonged, the front line due to this unusual fluid motion tended to diminish away. It seemed that advection force prevailed over the upward fluid motion.

3.3 Hydrodynamics of incompressive fluid flow

In modeling the given experimental system, the motion of particles (e.g., proton, electron or deuteron) was simulated as a 2D incompressive fluid composed of identical particles (correspond to fluid elements in the fluid), which time evolutions were calculated under the law of hydrodynamics. Here, a fluid was composed of fluid elements.

In the current LGCA method macroscopic hydrodynamic parameters, such as ν the kinematic share viscosity, d the density and v the velocity have been derived by ensemble averaging 2D configurations to give mass and momentum densities. Further these parameters have been shown to correspond to those of a real fluid. Thus taking Navier-Stokes equation with multi-scale analysis, important parameter: Re the Reynolds number is defined by

Time steps	10000
Lattice size	4640 x 1152
Coarse graining	32 x 32
Position of plate	center of domain
height	128
Inflow pres.	$p = 3/7 \cdot \rho$
Density	$\rho = 0.444594$
Outflow pres.	$p = 3/7 \cdot \rho$
Density	$\rho = 0.430252$

Table 2 Parameters for LGCA simulation. BC: Particle generation and disappearance conditions.

$$\mathrm{Re} = U \cdot L / \nu \qquad (1)$$

where U is a characteristic flow velocity (usually the flow velocity far upstream of the obstacle), L is a characteristic spatial scale of the obstacle (for an obstacle in the form of a plate, for example, L is the length). From experiments the flow is laminar or eddies formed with Re ranging less than 100 while a so-called von Karman vortex street will build up with Re $\approx$ 100. Our conditions lie within the region of eddies formed behind the obstacle.

Apart from rigorous derivation incompressive Navier-Stokes equation with multi-scale analysis is

Navier-Stokes equation

$$\partial v / \partial t + (v \cdot \nabla) v = -\nabla p + 1/\mathrm{Re} \nabla^2 v$$

Continuity equation

$$\nabla \cdot v = 0$$

where p is the kinematic pressure; ∇ is the nabla operator. The first term of left hand side denotes unsteady velocity; the second term the nonlinear advection term; the first term of right hand side the pressure term; the second term the viscous term. The viscous term of the equation was derived in different way (density constant) to evaluate this term in the velocity v. Figure 6 shows the time evolution of the velocity distribution, i.e., particles possessing higher velocity exhibits spread over with lateral symmetry. It is also shown that above three terms exhibit their characteristic time scales, i.e., relaxation or recovery time constant at perturbation. Whereas the relaxation (mass and momentum density) to local equilibrium

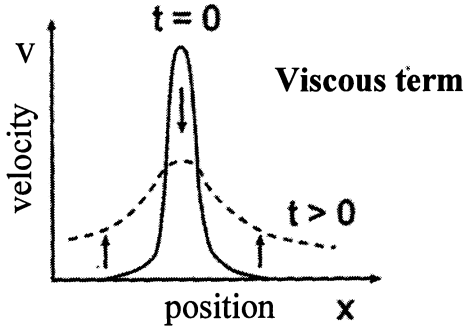

Fig.6 Time evolution of velocity distribution. Only viscous term is extracted neglecting nonlinear term and with given const. viscosity.

distribution after perturbation is several time steps, sound waves and advection proceed with time scale: c.a. 100 and diffusion shows time scale: 10000. Although the detailed description is not here, numerical simulation revealed that the initial conditions set by limited high or low density area in the inner region were relaxed very slowly and in lateral symmetrical way, therefore the above observed upward wave from the Outflow boundary region is attributable to the viscous term. Hence much improved BC at the Outflow boundary region is needed to attain well functioned simulation.

3.5 Optimum BC at Outflow boundary region

In the meantime to survey several BC the appropriate BC: so-called Sommerfelt's radiation condition was found, which works better than those BC provided[12]. The tried BC are listed

- Free Outflow BC: $\partial u/\partial x = \partial v/\partial x = 0$, $\partial p/\partial x = 0$
- Particle generation and disappearance model at Inflow and Outflow boundaries
- Sommerfelt's radiation condition

1. $\partial\Phi/\partial t + C\cdot(\partial\Phi/\partial x) = 0 : \Phi = v$ (neglect velocity in y-axis as a first approximation)

2. Apply forward discretization and addition of downward advection velocity: C at Outflow boundary sites

It is not easy to conclude the first two BC as improper ones because we are not confident of inspection of them. At present, however it is possible to accept Sommerfelt's radiation condition taking into account the disappearance of undesirable upward wave in FHP-III model. (see Fig.7)

4 Conclusion

We reproduced vortex pattern using LGCA numerical simulation method. The results showed that the unusual upward wave appeared in the downward flow stream which was generated at the Outflow boundary region. By applying Sommerfelt's radiation condition there obtained smooth flow which vectors were parallel to the channel. The vortex pattern was observed past a plate in the downward stream.

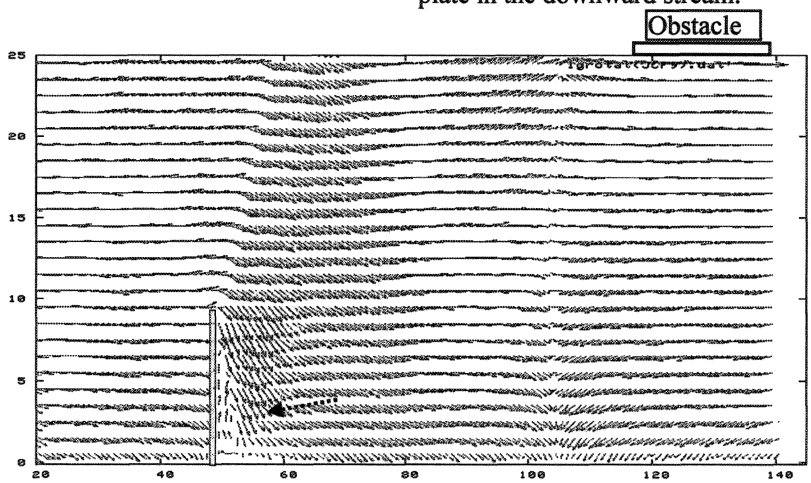

Fig.5 LGCA simulation results of vortex evolved past a plate on 4640x1152 grids at t =10000. BC: Particle generation and disappearance conditions.

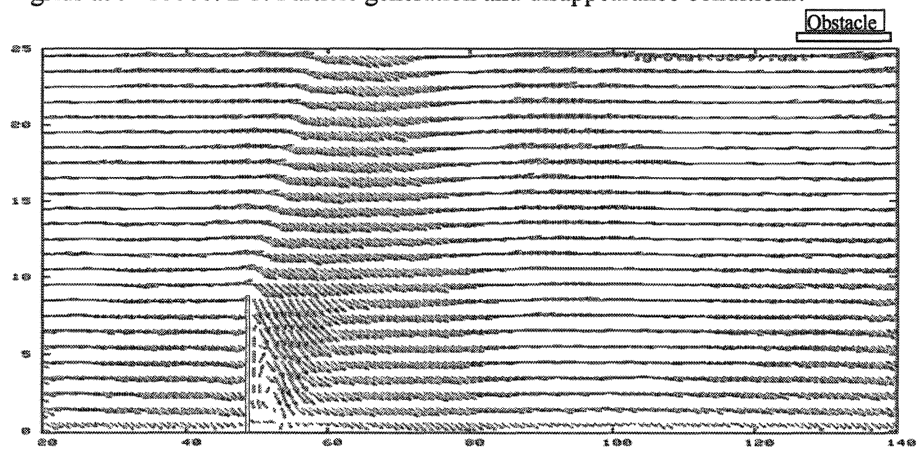

Fig.7 LGCA simulation results of vortex evolved past a plate on 4640x1152 grids at t =10000. BC: Sommerfelt's radiation condition.

References

1) H. Numata et al.: Proc. Conf. Science of Cold Fusion, Vol.33, pp.71, T.BRESSANI et al. eds., SIF, Bologna, Italy (1991)
2) R. Takagi et al.: Fusion Technol., **19** (1991)2135
3) H. Numata and M. Ban: Proc. ICCF12, Yokohama, pp.411-420 (2005)
4) H. Numata and M. Ban: Proc. JCF6, pp.32 (2005)
5) H. Numata and M. Ban: Proc. JCF8, pp.67 (2008)
6) D. d'Humières: Complex Syst. **1** (1987)599
7) H. Numata: in book "Cyber X" No.11, pp.37 (1999) Kougakusha.
8) A. Takahashi et al.: "Nuclear Reaction Study In Condensed Matter No.1", Chapter 4, pp.124, 1999 Kougakusha.
9) H. Numata and I. Ohno: Fusion Technol., **38** (2000)206
10) H. Numata and I. Ohno: ICCF6, Toya Japan, vol.**1**, pp.213(1997)
11) Y.Matsukuma and R.Takahashi: Trans.JSME, **61-588, B,** 2826(1995)
12) Yoshida et al.: Trans. JSME, **61-588, B,** 2887(1995)

Table 1 Comparison of measured speed at constant calculation size S(128x64x64)

順位 Rank	実測速度 Measured speed (MFLOPS)	CPU数 CPU number	メーカー Manufacture	機種 Model	CPU	クロック Clock	コンパイラー Compiler	オプション Option	備考 Misc.info	計算サイズ Size
	4705.05	1	NEC	SX-5	10GFLOPS	312.5MHz		"Chopt"		S(128x64x64)
1	1325.42	2	HP	Compac 8510w	Intel Core™ 2 Duo	2.4GHz		Vectorization	CentOS 5 Mem.4GB	S(128x64x64)
2	224.44	2	Home made		Intel Core™ 2 Duo	1.86GHz			WinXP Mem. 2GB	S(128x64x64)
3 (学実)	82.29	1	DELL	OptiPlex 743	Pentium Ⅳ	3GHz			WinXP Mem. 512MB	S(128x64x64)
4	**42.80**	**1**	**Authentic AMD**	**AMD Duron ™**		**707MHz**			**VineLinux 4.1 Mem. 124MB**	**S(128x64x64)**
5	34.41	1	IBM	Aptiva	Pentium Ⅳ	1.4GHz			WinMe Mem. 1.5GB	S(128x64x64)

Proceedings of JCF9, March 28-29, 2009, Shizuoka-ken Sangyo Keizai Kaikan, Shizuoka, Japan

A theoretical study on the possible change of the phonon dispersion relation due to the nuclear reaction in solid

Ken-ichi TSUCHIYA

Department of Chemical Science and Engineering, Tokyo National College of Technology, 1220-2 Kunugida, Hachioji, Tokyo 193-0997, Japan
e-mail: tsuchiya@tokyo-ct.ac.jp

Abstract: The phonon dispersion relation depends on the structure of the solid and the interaction between the ions in the solid. Therefore, if the structure and interactions are changed, the dispersion curves should be changed accordingly. In this study, the phonon dispersion relation of the palladium deuteride was analyzed from the one-dimensional lattice with two ions per primitive cell. In this model, heavy ions and light ions are distributed alternatively along a line and harmonic interactions between the neighboring ions are assumed. Well known solutions of this problem are given in the textbooks. It is a very simple model but it can give suggestive results for the replacements of the light ions. In this case heavy and light ions correspond to Pd ion and deuteron, respectively. And replacements mean nuclear reactions. We can apply this discussion to the Raman observation of the palladium deuterides.

1. Introduction

In solid state physics, phonon dispersion relation is one of the most important information, because it includes not only the geometric and electronic structure of the crystal but also interaction between ions or electrons. For example, it is well known that superconductivity is completely explained by using electron-phonon interaction [1]. Also in the studies of nuclear reaction in solids, A.Takahashi [2] and many other researchers pointed out the role of phonon. In this study, the possible changes of the phonon dispersion relation due to the nuclear reaction in solid were discussed. One-dimensional model was used for simplification, but it can be applied to the discussion for the real cases.

2. Phonon dispersion relation of solids

The theories of phonon dispersion relation of solids are introduced in many textbooks of solid state physics [3,4]. In this section, they are introduced briefly. The equilibrium positions of ions in crystalline solids are written as

$$\mathbf{R}_{nm} = \mathbf{r}_n + \mathbf{k}_m, \tag{1}$$

where $\mathbf{r}_n$ and $\mathbf{k}_m$ mean position of the n-th primitive cell and position of the k-th ion in the cell, respectively. The total kinetic and potential energies are defined using displacement vector $\mathbf{u}_{nm}$ from $\mathbf{R}_{nm}$ as

$$K = \frac{1}{2}\sum_{nmj} M_m \left(\dot{u}^j_{nm}\right)^2 \tag{2}$$

and

$$V = V_0 + \sum_{nmj}\left[\frac{\partial V}{\partial u^j_{nm}}\right]_0 u^j_{nm} + \frac{1}{2}\sum_{nmj}\sum_{n'm'j'}\left[\frac{\partial^2 V}{\partial u^j_{nm}\partial u^{j'}_{n'm'}}\right]_0 u^j_{nm}u^{j'}_{n'm'} + \cdots \tag{3}$$

where M_m is the mass of the m-th ion in the primitive cell and the summation for j is done over Cartesian coordinate x, y and z. In eq.(3), the second term should be omitted, because the force acting on the ions at equilibrium poison equals zero. Therefore, the total potential is written in the 2nd order approximation as

$$V = V_0 + \frac{1}{2}\sum_{nmj}\sum_{n'm'j'} C^{jj'}_{nmn'm'} u^j_{nm} u^{j'}_{n'm'} \tag{4}$$

where C is the second order partial derivative of V with respect to the displacement. The Lagrangian $L = K - V$ satisfies well known Lagrange's equation

$$\frac{d}{dt}\frac{\partial L}{\partial \dot{u}^j_{nm}} = \frac{\partial L}{\partial u^j_{nm}} . \tag{5}$$

This gives the equation of motion for each ions

which is written as

$$M_m \ddot{u}^j_{nm} = -\sum_{n'm'j'} C^{jj'}_{nmn'm'} u^{j'}_{n'm'} \ . \qquad (6)$$

In this equation, displacement u satisfy Bloch theorem

$$u^j_{nm} = e^{i\mathbf{q}\cdot\mathbf{r}_n} u^j_{0m} \qquad (7)$$

and coefficient C has a symmetry

$$C^{jj'}_{nmn'm'} \longrightarrow C^{jj'}_{mm'}(\mathbf{h}) \qquad (\mathbf{h} = \mathbf{r}_{n'} - \mathbf{r}_n) \ . \quad (8)$$

Defining the Fourier transformed formula as

$$\sum_{\mathbf{h}} C^{jj'}_{mm'}(\mathbf{h}) e^{i\mathbf{q}\cdot\mathbf{h}} \equiv G^{jj'}_{mm'}(\mathbf{q}) \qquad (9)$$

and assuming the oscillatory solution as

$$u^j_{nm}(t) = e^{-i\omega t} u^j_{nm}(0) \ , \qquad (10)$$

we obtain the relation between the angular frequency ω and the wave number vector $\mathbf{q}$. It is called phonon dispersion relation and written as

$$\sum_{m'=1}^{M} \sum_{j'=1}^{3} G^{jj'}_{mm'}(\mathbf{q}) u^{j'}_{0m'}(0) = \omega^2 u^j_{0m}(0) \qquad (11)$$

where M is the number of ions including in a primitive cell. This equation is rewritten as an eigenvalue problem using $3M \times 3M$ type matrix. Solving the problems for each value of $\mathbf{q}$, we can get eigenvalue ω. In the practical calculation of G, the Born-von Karman's periodic boundary condition is used.

Firstly, we consider monatomic one-dimensional lattice vibrating in the three-dimensional space. In this case, only one ion is included in a primitive cell and eq.(11) is rewritten as

$$\begin{pmatrix} G^{11} & G^{12} & G^{13} \\ G^{21} & G^{22} & G^{23} \\ G^{31} & G^{32} & G^{33} \end{pmatrix} \begin{pmatrix} u^1 \\ u^2 \\ u^3 \end{pmatrix} = \omega^2 \begin{pmatrix} u^1 \\ u^2 \\ u^3 \end{pmatrix} \qquad (12)$$

where matrix element G depends on the absolute value of the wave number vector $\mathbf{q}$, because the phonon wave propagates only along the lattice direction z. This equation gives three solutions. Two of them are doubly-degenerated, because x and y transverse directions are isotropic. The typical solutions are sketched in Fig.1.

Secondly, we consider diatomic one-dimensional lattice vibrating in the three-dimensional space. A heavy ion and a light ion are alternatively arrayed along the lattice line. In this case, two ions are included in a primitive cell and eq.(11) is rewritten as

$$\begin{pmatrix} G^{11}_{11} & G^{12}_{11} & G^{13}_{11} & G^{11}_{12} & G^{12}_{12} & G^{13}_{12} \\ G^{21}_{11} & G^{22}_{11} & G^{23}_{11} & G^{21}_{12} & G^{22}_{12} & G^{23}_{12} \\ G^{31}_{11} & G^{32}_{11} & G^{33}_{11} & G^{31}_{12} & G^{32}_{12} & G^{33}_{12} \\ G^{11}_{21} & G^{12}_{21} & G^{13}_{21} & G^{11}_{33} & G^{12}_{33} & G^{13}_{33} \\ G^{21}_{21} & G^{22}_{21} & G^{23}_{21} & G^{21}_{33} & G^{22}_{33} & G^{23}_{33} \\ G^{31}_{21} & G^{32}_{21} & G^{33}_{21} & G^{31}_{33} & G^{32}_{33} & G^{33}_{33} \end{pmatrix} \begin{pmatrix} u^1_1 \\ u^2_1 \\ u^3_1 \\ u^1_2 \\ u^2_2 \\ u^3_2 \end{pmatrix} = \omega^2 \begin{pmatrix} u^1_1 \\ u^2_1 \\ u^3_1 \\ u^1_2 \\ u^2_2 \\ u^3_2 \end{pmatrix} \qquad (13)$$

The typical solutions are sketched in Fig.2.

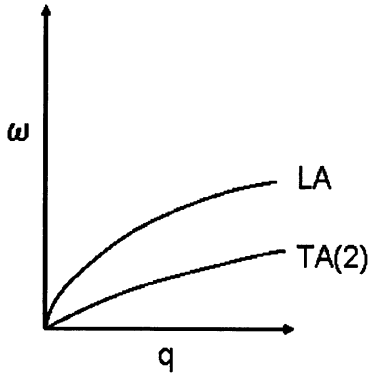

Fig. 1. Phonon dispersion relation of monatomic one-dimensional lattice vibrating in the three dimensional space. Characters LA and TA(2) mean longitudinal acoustic and doubly-degenerate transverse acoustic modes, respectively.

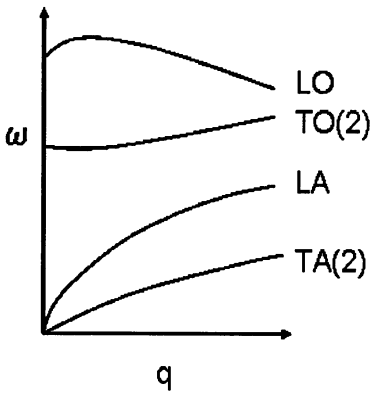

Fig. 2. Phonon dispersion relation of diatomic one-dimensional lattice vibrating in the three dimensional space. Characters LA and TA(2) mean longitudinal acoustic and doubly-degenerate transverse acoustic modes, respectively. Characters LO and TO(2) mean longitudinal optical and doubly-degenerate transverse optical modes, respectively.

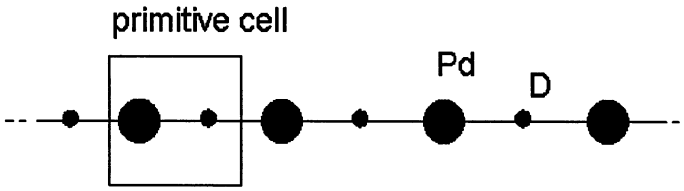

Fig. 3. One-dimensional PdD lattice

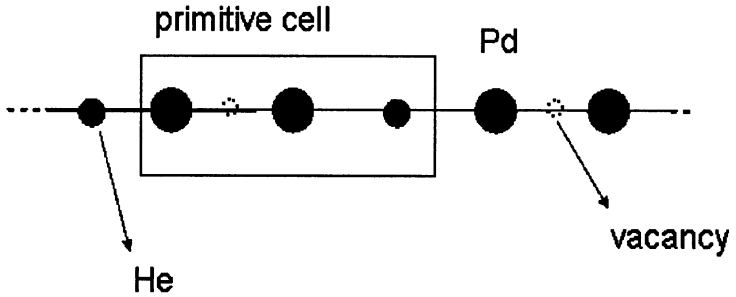

Fig. 4. A model of structure changed one-dimensional PdD lattice due to nuclear reaction

For the case of three-dimensional lattice, we can calculate phonon dispersion relation by using same method described above. However, direction of the wave propagation is not only one, so ω depends not only on the absolute value but also on the direction of vector **q**. Therefore, some results along the symmetric directions are plotted in the textbooks [3,4].

3. Change of the phonon dispersion relation due to the nuclear reaction

We discuss the phonon dispersion relation of palladium deuteride using the one-dimensional PdD lattice vibrating in a three-dimensional space. It is a very simple model which is illustrated in Fig.3. The solution is easily obtained by using eq.(10). And the typical dispersion curves are similar to Fig.2.

If some nuclear reactions change the structure of the lattice in Fig.3, they will also change phonon dispersion relation. For example as illustrated in Fig.4, if deuterons are disappeared and He's are produced, a primitive cell contains two palladiums, one He and one vacancy. At this time, the dimension of the matrix in eq.(10) will be changed into 9×9 with 9 solutions. This means that some unknown phonon dispersion branches are created at the reaction. If we measure the phonon dispersion relation of palladium deuteride and find unknown extra dispersion branches, they may be evidences of nuclear reactions.

If we see the change of the lattice structure from Fig.3 to Fig.4, it might suggest the reaction

$$D + D \longrightarrow He + Energy. \qquad (14)$$

It is a model with oversimplification. In real case, more complicated and local reactions should be considered. For example, multi-body fusion or more complicated reaction [5] should be considered. However, the structure changes due to the nuclear reaction always tend to increase dispersion branches. In near future, we will calculate dispersion relation for same simple cases. This may find the evideces of nuclear reactions in the experimental results for phonon dispersion relation [6] or Raman observation [7,8] of palladium deuterides.

4. Conclusions

(i) After the nuclear reaction in solids, the number of the ions in a primitive cell is increased.
(ii) Even if the structure change due to the reaction is spatially nonuniform, the tendency in conclusion (i) is unaltered.
(iii) The tendency in conclusion (i) increases the dimension of eigenvalue problem and this causes the increment of dispersion branches.
(iv) If we measure the phonon dispersion relation of palladium deuteride and find un-

known extra dispersion branches, they may be evidences of nuclear reactions.

(v) These discussions can be applied to our Raman observation of the palladium deuterides [7,8].

Acknowledgements

The author wishes to thank Professor S.Sasabe of Tokyo Metropolitan University and Professor M.Ozaki of Tokyo University of Agriculture for helpful discussions and encouragements at monthly seminar.

References

[1] J.Bardeen, N.Cooper and R.Schrieffer, Phys.Rev. **108**(1957)1175

[2] A.Takahashi, et al., Fusion Technology, **19**(1991)380

[3] C.Kittel, *Introduction to Solid State Physics*, John Wiley and Sons, Chapter 5.

[4] N.W.Ashcroft and N.D.Mermin, *Solid State Physics*, Holt-Saunders, Chapter 22.

[5] A.Takahashi, proceedings of JCF8, p51(2007)

[6] J.M.Rowe, J.J.Rush, H.G.Smith, M.Mostoller and H.E.Flotow, Phys. Rev. Letts., **33**(1974)1297

[7] R.Sherman, H.K.Birnbaum, J.A.Holy and M.V.Klein, Phys. Lett., **62A**(1977)353

[8] K.Tsuchiya, A .Watanabe, M.Ozaki and S.Sasabe, "Observation of optical phonon in palladium hydrides using Raman spectroscopy", proceedings of ICCF14 (Aug. 2008, Washington DC), to be published.

Proceedings of JCF9, March 28-29, 2009, Shizuoka-ken Sangyo Keizai Kaikan, Shizuoka, Japan

Non-localized Proton/Deuteron Wavefunctions and Neutron Bands in Transition-metal Hydrides/Deuterides

Hideo Kozima

Cold Fusion Research Laboratory, 597-16 Yatsu, Aoi, Shizuoka, 421-1202, Japan

Abstract

Using knowledge about hydrogen/deuterium wave functions in transition metals obtained in solid-state physics and in chemistry of catalysis, we discuss quantal bases of the neutron band introduced in the phenomenological explanation of the cold fusion phenomenon (CFP). The non-local wavefunctions of protons/deuterons have been used to understand diffusion characteristics in transition metals in the body and also effects of hydrogen to catalytic behavior of transition metals on the surface and in the subsurface region. These characteristics of hydrogen isotopes on the surface, in the subsurface and in the body seems to have a close relation with the CFP that occurs in the localized region at surface regions of diameters several μm and depths also several μm. It is shown that the non-local wavefunctions of the proton/deuteron in the transition metals are favorable for the concept of the neutron band introduced to explain premises of the phenomenological models (TNCF and ND models). The CFP observed in the hydrogen non-occlusive metals, W, Pt, and Au, has given evidence that the TNCF model is applicable to nuclear transmutations (NT) with the change ΔA of mass number equals 1 and the ND model is to NT with $\Delta A > 1$ where the generated nuclides suffice the stability law.

1. Introduction

The cold fusion phenomenon (CFP), a part of which was discovered by Fleischmann, Pons and Hawkins (F-P-H) in 1989 [1], is a phenomenon consists of various events caused by nuclear reactions in room temperature solids consisting of periodic arrays of such specific nuclei as carbon (C), titanium (Ti), nickel (Ni), palladium (Pd), and other several transition metals interlaced with also periodic arrays of hydrogen isotopes (H and/or D (H/D)) dipped in ambient thermal neutrons.

The observables of the events in the CFP are new nuclei generated by nuclear transmutations (NT's) ranging from lightest neutron n to heaviest Pb on the periodic table of elements, their isotopic ratios shifting sometimes from natural ones, accompanying huge excess energy inexplicable by atomic (chemical) reactions conceivable in the systems.

This situation appeared in the so-called Cold Fusion (CF) or condensed matter nuclear science (CMNS) is out of range of understanding from common sense in the established branches of modern science of nuclear physics and solid-state physics. Therefore, the CFP it self is left out of research fields of established sciences for more than twenty years. These characteristics of the CFP ask us to use a phenomenological approach as successfully performed by our models [2 – 3] with trials of quantal verification of assumptions made in the models [2, 4, 5].

Looking into experimental data sets obtained in this field of the CF research minutely in relation with knowledge obtained in established fields of modern

science, we notice that there are many regions in the established sciences which have not well developed until now. Several regions closely related to the events in the CFP are (1) neutron states at around the evaporation level, exotic nuclei with excess number of neutrons at medium nucleon numbers, and wavefunctions of neutrons in them in nuclear physics, and (2) microscopic difference of *bcc* and *fcc* transition-metal hydrides/deuterides and wavefunctions of protons/ deuterons adsorbed on and occluded in *fcc* transition-metal crystals in solid-state physics and surface chemistry.

Another riddle of the materials where occurs the CFP (the CF materials) is their relation to the catalytic power of them; almost all CF materials are good catalysts for some chemical reactions. This fact was already noticed by many electrochemists who tried to figure out the relation experimentally without remarkable success until now depending on, perhaps, complicated mechanism of the CFP related to atomic and nuclear processes compared with that of the catalysis related only to atomic processes which is, even so, complicated to be cleared out completely.

Therefore, it is necessary to extend our point of view out of that initiated by F-P-H in the first paper [1] that the cold fusion might be a phenomenon induced by the *d–d* fusion reactions assisted by some quantum field effects in the transition metal environment.

In this paper, we survey the natures of the CFP and of catalysis seemingly having close interrelation with each other from our point of view to promote investigation of the science of the former and give an answer to the question why the good catalysts are the good materials for the CFP.

2. Wavefunctions of Protons/Deuterons Occluded in Metals

The diffusion of hydrogen isotopes in transition metals has attracted attention due to its largeness and characteristics. There are many attempts to explain them by using proton/deuteron bands [6 – 8].

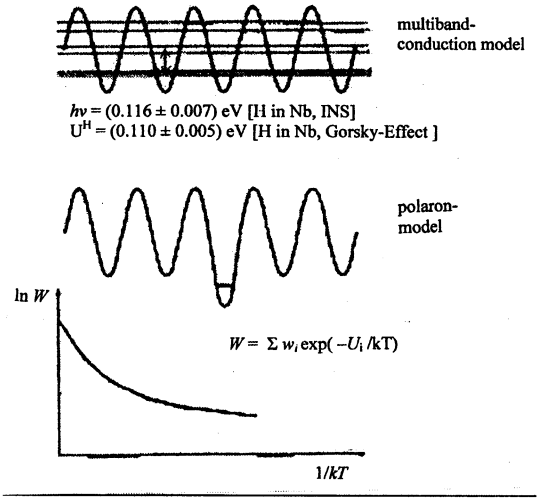

Fig.1 Hydrogen diffusion models ([7], Fig. 5).

Fig. 1 shows a simplified proton band scheme [7]. The probability W for transition from one site to another is given by probability w_i in a certain band times the occupation of this band exp $(-U_i$ /kT). Therefore,

$$W = \Sigma w_i \exp(-U_i/kT) \qquad (2\text{-}1)$$

The transition probability w_i is small for the lowest band and increases from band to band.

The idea of the proton/deuteron bands explained by Alefeld [7] was more concretely taken into calculation of the diffusion properties of proton/deuteron in Nb by Sussmann and Weissman [8].

Bloch functions and Wannier functions

If $q_{\mathbf{k}}(x)$ designates a Bloch function with wave vector $\boldsymbol{k}$ of a given band, the corresponding Wannier function $w_0(\boldsymbol{x}-\boldsymbol{x}_n)$ will be defined as

$$w_0(\boldsymbol{x}-\boldsymbol{x}_n) = N^{-1/2} \sum_{\mathbf{k}} \exp(-i\boldsymbol{k}\boldsymbol{x}_n)\, q_{\mathbf{k}}(\boldsymbol{x}) \qquad (2\text{-}2)$$

and conversely

$$q_k(x) = N^{-1/2} \sum_n \exp(ikx_n)\, w_0(x - x_n). \quad (2\text{-}3)$$

If time dependence is introduced, the expression (2-2) becomes

$$w(x - x_n, t) = N^{-1/2} \sum_k \exp(-ikx_n + i\omega_k t)\, q_k(x) \quad (2\text{-}4)$$

or, in the limit of a very long crystal,

$$w_{xn=0}(x,t) = (1/2\pi) \sum_m w_0(x - x_m) \times \int_{-\pi/\ell}^{+\pi/\ell} \exp(-ikx_m + i\omega_k t)\, dk \quad (2\text{-}5)$$

where we have N sites at a distance ℓ from each other. In the tight-binding approximation we get for the spectrum

$$\omega_k = (\delta/h) \sin^2(k\ell/2). \quad (2\text{-}6)$$

We can now evaluate the integral in (2-5):

$$\int_{-\pi/\ell}^{+\pi/\ell} \exp i(kn\ell - \delta t/h \sin^2(k\ell/2))\, dk = \ell^{-1} \int_{-\pi}^{+\pi} \exp i(nu - \delta t/h \sin^2(u/2))\, du = \ell^{-1} \exp(i\delta t/h)\, i^n J_n(\pi\delta t/h), \quad (2\text{-}7)$$

where J_n is the nth order Bessel function. Since

$$J_n(0) = 0 \quad \text{for } n \neq 0, \quad (2\text{-}8)$$

We see that at $t = 0$ the wave packet is localized at the origin, and expands later on, as was expected.

We shall now describe the migration process as an excitation of the particle from a localized ground state to an excited Wannier state, followed by its decay into either the ground state at any other site. As the excited state (Wannier function) is not a stationary one, the decay rate into any given state is time-dependent. Because the probability for decay is much larger than the probability for excitation, we are justified in integrating over time in order to obtain the decay fraction into any given site. If we neglect transitions between a ground state in site n and an excited localized state $w(x - x_m)$ in other site ($m \neq n$), the transition probability between the tight-binding approximation Wannier function (originally centered at $x = 0$) and a ground state in site n will be proportional to $J_n^2(\pi\delta t/h)$. Typical behavior of the Wannier functions is presented in Fig. 2.

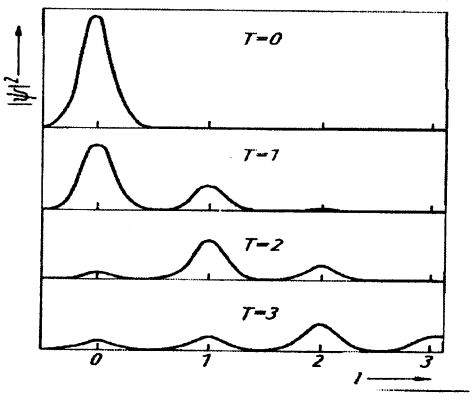

Fig. 2 Time evolution of tight-binding Wannier functions (Fig.1 of [8]). Plot of

$$|\psi(x)|^2 = \sum_m J_n^2(T) G(x - m\ell),$$

where $G(x - x_m)$ is Gaussian for several times.

Thus, as Fig. 2 shows concretely, wavefunctions of protons/deuterons in transition metals, especially *fcc* ones, should be considered not localized in an interstitial but extended over at least several sites from experimental facts of solid-state physics. This property of the wavefunctions of protons/deuterons in *fcc* transition metals is favorable for the neutron band formalism developed in Section 4.

The famous riddle of the compatibility between a host metal and a hydrogen isotope, Pd-D and Ni-H, in the CFP may be closely related to *the inverse isotope effect* of their diffusion coefficients in palladium. The ratios of diffusion coefficients of isotopes of hydrogen in nickel and palladium show normal and inverse isotope effect, respectively, as shown in Figs. 3 and 4 [9].

If we can assume that the diffusivity is positively related to non-localized property of the wavefunctions of the hydrogen isotopes, our treatment of the neutron band given in Section 4 shows that a model for the data in the CFP (Pd-D is favorable than Pd-H) in accordance

with the data of diffusion in solid-state physics (inverse isotope effect).

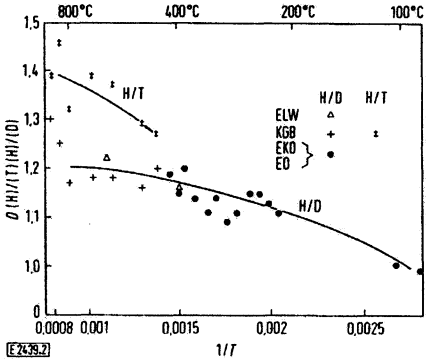

Fig. 3 Ratios of diffusion coefficients of isotopes of hydrogen in nickel [9].

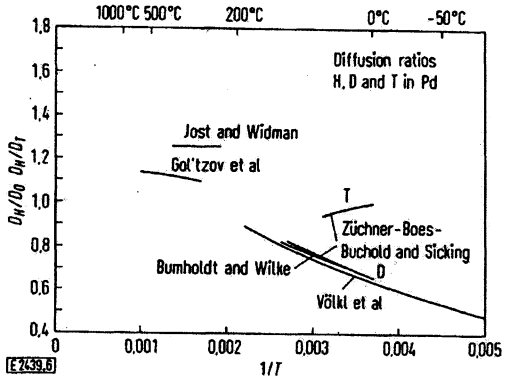

Fig.4 Ratios of diffusion coefficients of isotopes of hydrogen in palladium [9].

3. Wavefunctions of Protons/Deuterons Adsorbed on Metal Catalysts

The science of the catalysis has a long history more than a hundred years with a plenty of applications to benefit our daily life. Despite of strong interest by chemists and physicists to know exactly what the catalysis is, the nature of catalysis itself is not completely elucidated yet. For instance, the effects of hydrogen in catalysis were a theme of a symposium just 20 years ago [10].

The nature of the wavefunctions of hydrogen/deuterium, or rather proton/deuteron, on the surface region of metal catalysts is therefore investigated recently in relation to the action of catalysis. It is known now that the proton on the surface of metal catalysts is not localized at a specific lattice point and also not confined on the surface but penetrated into the metal by at least one lattice distance [11, 12]. It is used even a concept "subsurface hydrogen" to express this penetration [12].

Furthermore, they use a concept of the proton band to describe the nonlocal nature of these protons [11, 12] and use a concept "hydrogen fog" in analogy to the electron gas for the nearly free electrons in simple metals [11].

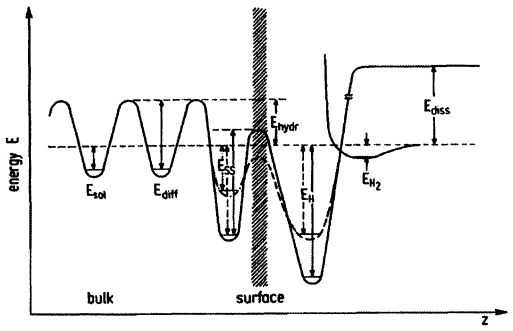

Fig. 5 Potential energy diagram for adsorption, "sorption" into so-called "subsurface sites," and bulk absorption for Pd (110) (Fig. 24 of [12]).

Fig. 5 shows a model of potential energy diagram at surface of Pd for a hydrogen atom. The symbols have the following meaning: E_{SOL}, heat of solution; E_{diff}, activation energy for bulk diffusion; E_{SS}, activation energy for desorption from the H subsurface sites; E_{hydr}, activation energy for hydrogenation; E_H, activation energy for desorption from the chemisorbed state; E_{H2}, adsorption energy of the physisorbed H_2; E_{diss}, heat of

dissociation of the H_2 molecule. The dashed line indicates the potential energy situation after the surface has been reconstructed by 1.5 monolayers of hydrogen. Clearly, the activation barrier for population of the subsurface sites is removed by reconstruction.

The characteristics of the adsorbed protium/deuterium on the catalysts clarified in these about 20 years show clearly the same nature to those investigated in transition-metal hydrides/deuterides explained in Section 2. Thus, the CFP observed in the latter is expected to occur in the former according to the speculation given in Section 2.

This knowledge of the hydrogen isotopes (at present they are mainly of hydrogen) gives us an indirect but a strong support to develop our investigation along the line of quantal calculation of the neutron band mediated by protons /deuterons already put in the previous papers [2, 4, 5]. The knowledge of proton/ deuteron wavefunctions is so far limited to that of adsorbed ones but we can infer similar nature of the wavefunctions of them in host materials.

Thus, we can give a unified perspective of the CFP in various CF materials from the transition-metal hydrides/deuterides, proton conductors, some hydrocarbons to biological bodies.

4. Neutron Bands in Transition-Metal Hydrides/Deuterides Mediated by Occluded Protons/Deuterons

The CFP investigated for more than 20 years includes very many various events from the nuclear transmutations to the production of enormous excess energy in deuterides and hydrides of several transition metals and hydrocarbons. To explain these complicated events from a unified point of view, we proposed a phenomenological model, the TNCF model, with an adjustable parameter n_n on the experimental facts. The model was successful to give several qualitative and sometimes semi-quantitative explanations for experimental data sets [2, 3].

The TNCF model has evolved into the neutron drop (ND) model to explain nuclear transmutations with large changes of mass number A [2].

To support the basis of the premises of the models, we have developed quantal investigation of the microscopic state of the CF materials and found existence of several unknown properties of nuclei and solids seemingly closely related with the CFP. We have used rather arbitrarily nature of neutron wavefunctions in host nuclei and occluded proton/deuteron wavefunctions in *fcc* transition metals to calculate the neutron band which is the key concept to support the basis of the premises of the TNCF and ND models [4].

The realization of the neutron band is governed by the value of the integral

$$\langle np;\mathrm{ij}|V|n'p';\mathrm{ij}\rangle$$

$$= \iint d\boldsymbol{r}d\boldsymbol{R}_j \psi^*_{\{n\}}(\boldsymbol{r}-\boldsymbol{a}_i)\,\varphi^*_{\{p\}}(\boldsymbol{R}_j-\boldsymbol{b}_j)$$

$$\times V_s\,(\boldsymbol{r}-\boldsymbol{R}_j)\;\psi_{\{n'\}}(\boldsymbol{r}-\boldsymbol{a}_i)\,\varphi_{\{p'\}}(\boldsymbol{R}_j-\boldsymbol{b}_j), \qquad (4\text{-}1)$$

where $\boldsymbol{a}_i$ and $\boldsymbol{a}_{i'}$ are nearest neighbor of an interstice $\boldsymbol{b}_j$ and the integral is governed by the overlapping of the proton/deuteron wave function $\varphi_{\{p\}}(\boldsymbol{R}_j-\boldsymbol{b}_j)$ on an interstice at $\boldsymbol{b}_j$ with a nucleon (neutron) wave function $\psi_{\{n\}}(\boldsymbol{r}-\boldsymbol{a}_i)$ on an adjacent lattice nucleus at $\boldsymbol{a}_i$ resulting in a proton-neutron interaction through the nuclear force (cf. Fig. 6) [2, 4, 5]. The potential V_s is given, for instance, as follows;

$$V_s(\boldsymbol{r}-\boldsymbol{R}) = -V^{(s)}_0, \qquad (|\boldsymbol{r}-\boldsymbol{R}| < b)$$
$$= 0, \qquad (|\boldsymbol{r}-\boldsymbol{R}| > b)$$

where $V^{(s)}_0 \simeq 3.5$ MeV and $b \simeq 2.2\times10^{-13}$ cm [Blatt 1952].

The effective interaction potential $v_{np}(ii'j)$ between two

neutrons mediated by a proton/deuteron at b_j (*super-nuclear interaction*) is described as a summation of the matrix element (4-1) over j as follows (Eq. (3.7-4) of [2]);

$$v_{np}(ii'j) = \sum_{\{p'\}\neq\{p\}} P\int dE\, \rho_n(E) \times$$
$$(\langle np;ij|V|n'p';ij\rangle\langle n'p';i'j|V|np;i'j\rangle)/(E+\varepsilon_{p'p}), \quad (4\text{-}2)$$

where $\rho_n(E)$ is a density of states for neutron quantum states (cf. Subsection 3.7.2(a) of [2]) and

$$\varepsilon_{p'p} \equiv \varepsilon_{p'} - \varepsilon_p, \text{ and } E \equiv E_{\{n'\}} - E_{\{n\}}.$$

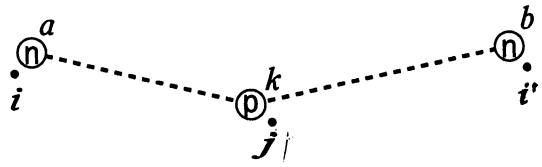

Fig. 6 Super-nuclear interaction between two neutrons a (at a_i) and b (at $a_{i'}$) in lattice nuclei i and i' mediated by a proton (or a deuteron) k at an adjacent interstitial site b_j.

Therefore, one of the key factors to realize the neutron band is the non-localized property of the proton/deuteron wavefunction in the CF material which is not well determined in the physics of metal hydrides yet. A part of the difficulty of the determination of the required wavefunction should be related with its close relation with the proton/deuteron–nucleon interaction which has not noticed by the solid-state physicists.

There are, however, several trials to figure out the wavefunctions of the protons/deuterons participating in diffusion in *fcc* transition metals as shown in Section 2 and also playing an important role in catalysis on the surface of metal catalysts having *fcc* lattice as shown in Section 3.

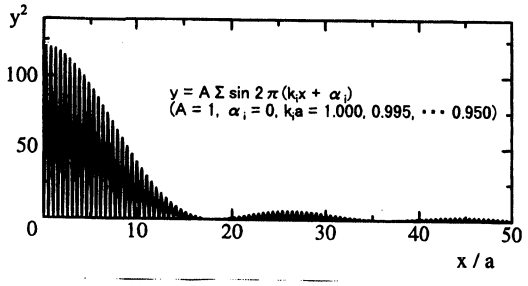

Fig. 7 Neutron density accumulation of 11 neutrons reflected coherently at boundary. Abscissa is the distance in a unit of lattice constant a from the boundary where the neutron waves reflected. When a wave is reflected, the profile is a straight line at a height 1 parallel to the abscissa ([2] Fig. 3.4).

When there is a neutron valence band in a crystal, accumulation of neutrons at surface/boundary regions occurs by coherent reflection of neutron Bloch wave at these region as shown in Fig. 7 [2].

When there is a neutron liquid with densities more than 10^{35} cm^{-3}, there appears a so-called *Coulomb lattice* of "clusters of neutrons, protons and compensating electrons" (*neutron drops*), with a definite lattice constant a as a stable state as shown in Fig. 8 [13].

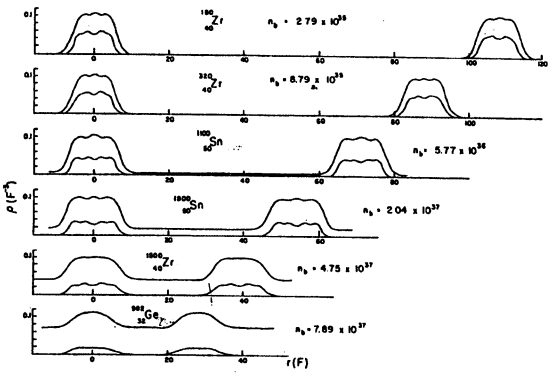

Fig. 8 Formation of cf-matter composed of neutron drops and background neutrons [13].

There is evidence to show the existence of such exotic nuclei as $^{10}_{2}$He, $^{11}_{3}$Li, $^{32}_{11}$Na [14]. These exotic

nuclei might be an evidence of rather strong and long-range attraction between neutron and proton (*n-p*) than proton-proton (*p-p*) and neutron-neutron (*n-n*) interactions.

This property of nuclear interactions between nucleons and also the Coulomb lattice in neutron star matter suggest us to assume existence of small *neutron-proton/deuteron clusters* ${}^{A}_{Z}\delta$ and finally neutron drops ${}^{A}_{Z}\Delta$ (clusters of $(A - Z)$ neutrons containing Z protons in it) in CF materials when the density of neutrons becomes high enough at surface/boundary regions.

Using the TNCF model, we can explain nuclear transmutations (NT) with a change ΔA of mass number is one with an emission of phonon(s) φ's but a photon γ in free space;

$$n + {}^{A}_{Z}X \rightarrow {}^{A+1}_{Z}X^{*} \rightarrow {}^{A+1}_{Z}X + \varphi\text{'s} \qquad (4\text{-}3)$$

For the NT with $\Delta A > 1$, we can use the ND model as follows;

$${}^{A}_{Z}\Delta + {}^{A'}_{Z'}X \rightarrow {}^{A-a}_{Z-z}\Delta + {}^{A'+a}_{Z'+z}X'^{*},$$

$$\rightarrow {}^{A-a}_{Z-z}\Delta + {}^{A'+a-a'}_{Z'+z-z'}X'' + {}^{a'}_{z'}X''', \qquad (4\text{-}4)$$

$${}^{A'}_{Z'}\Delta + {}^{A+1}_{Z}X^{*} \rightarrow {}^{A'}_{Z'}\Delta^{*} + {}^{A+1}_{Z}X \rightarrow {}^{A'}_{Z'}\Delta + {}^{A+1}_{Z}X + x, \qquad (4\text{-}5)$$

$${}^{A'}_{Z'}\delta + {}^{A}_{Z}X \rightarrow {}^{A+A'}_{Z+Z'}X^{*} \rightarrow {}^{A+A'}_{Z+Z'}X + x. \qquad (4\text{-}6)$$

where the symbol x means not a γ photon in the free space but another particle (a neutron or a neutron-proton cluster) in cf-matter. The neutron-proton cluster ${}^{A}_{Z}\delta$ is supposed to be a unit of nucleons absorbed simultaneously by a nuclide to form a new nuclide as in Eq. (4-6).

5. Unified Explanation of the CFP in Various Kinds of CF Materials

As have been worked out in previous papers [2–5], we could explain various features of the CFP not only in deuterides but also hydrides using the TNCF (trapped neutron catalyzed fusion) and ND (neutron drop) models supported by the quantal investigation of neutron band and cf-matter formation where appears the neutron drop composed of Z protons and $(A - Z)$ neutrons.

In the case of the CFP in transition-metal hydrides/deuterides, we have given several semi-quantitative explanations of experimental results [2–5]. One of the most spectacular results is the ratios of the numbers of events $(N_a/N_b)_{th}$ for events a and b which are in accordance with the experimental data $(N_a/N_b)_{ex}$ in a factor of about three;

$$(N_a/N_b)_{th} = C\,(N_a/N_b)_{ex},\ C \approx 3. \qquad (5\text{-}1)$$

Another noticeable result of the TNCF-ND model is the explanation of the inverse-power law of the frequency of an event vs. its intensity with the power index of about 1 [2, 15, 16]. To explain the characteristic of composite systems, it is necessary to consider the events (excess energy production and neutron emission, in this case) as those in a phenomenon induced in the CF materials by nonlinear interactions between agents (composing nuclei) in them. This point of view is supplied by the TNCF model which assumes multi-particle interaction in the CF material.

On the extended line of this investigation, we could explain such interesting features of the CFP as bifurcation of events (alternative occurrence of two branches with different intensity) and chaotic behavior of events (wide dispersion of intensity at the same experimental parameters) [15, 16].

The CFP in such metals as W, Pt, and Au which do not occlude hydrogen isotopes might be explained by the same mechanism as those in PdD_x and others in terms of the nature of the surface proton/deuterons shown by the investigation of the catalysis [17, 18].

The CFP in such hydrocarbons as cross-linked polyethylene (XLPE) are investigated on the same basis of other events in CF materials [19, 20] giving successful explanation of NT products.

The CFP, or NT (nuclear transmutations) in the case of carbon hydrides (phenanthrene and XLPE) has been investigated to explain experimental data satisfactorily using the TNCF model [15, 16]. The generation of new nuclides in the system without any transition metal is explained by neutron assisted nuclear reactions facilitated by formation of the neutron band, and therefore the cf-matter, due to the periodic arrays of carbon nuclei and protons.

5-1. TNCF model explanation

The nuclear transmutation of ^{12}C to ^{13}C in the phenanthrene is explained as follows;

$$^{12}_{6}C + n \rightarrow {}^{13}_{6}C^{*} \rightarrow {}^{13}_{6}C + \gamma \qquad (5\text{-}2)$$

with E_γ = 4.95 MeV. The photon γ emitted in this reaction will be measured or it should be replaced by phonons φ's emitted by such a mechanism proposed by us [2];

$$^{12}_{6}C + n \rightarrow {}^{13}_{6}C^{*} \rightarrow {}^{13}_{6}C + \varphi\text{'s}. \qquad (5\text{-}3)$$

The NT's in the case of XLPE [18, 19], the nuclear transmutations,

K → Ca,

$$(n + {}^{39}_{19}K \rightarrow {}^{40}_{20}K^{*} \rightarrow {}^{40}_{20}Ca + e^{-} + \underline{\nu}_e) \qquad (5\text{-}4)$$

Mg → Al,

$$(n + {}^{26}_{12}Mg \rightarrow {}^{27}_{12}Mg^{*} \rightarrow {}^{27}_{13}Al + e^{-} + \underline{\nu}_e) \qquad (5\text{-}5)$$

and

$$^{56}_{26}Fe \rightarrow {}^{57}_{26}Fe, \ (n + {}^{56}_{26}Fe \rightarrow {}^{57}_{26}Fe + Q) \qquad (5\text{-}6)$$

are explained by a single neutron absorption with or without a succeeding beta-decay to get final nuclides.

5-2. ND model explanations.

The NT's,

$$^{56}_{26}Fe \rightarrow {}^{64}_{30}Zn \ (^{56}_{26}Fe + {}^{8}_{4}\Delta \rightarrow {}^{64}_{30}Zn) \qquad (5\text{-}7)$$

and

$$^{56}_{26}Fe \rightarrow {}^{60}_{28}Ni, \ (^{56}_{26}Fe + {}^{4}_{2}\Delta \rightarrow {}^{60}_{28}Ni) \qquad (5\text{-}8)$$

are explained by an absorption of a neutron drop $^{8}_{4}\Delta$ and $^{4}_{2}\Delta$, respectively, in the cf-matter that was supposed to be formed at boundary regions of crystallites in the sample by the mechanism explained in Section 2..

On the line of extension of this investigation on nuclear transmutations in hydrocarbons, we may be able to understand the biotransmutation as had been given more than ten years ago in our old book [3].

5-3 NT in $Au/H_2O+Na_2SO_4/Pt$ system Explained by TNCF and ND models

It is interesting that the recent analysis of the data obtained in $Au/H_2O + Na_2SO_4/Pt$ system shows that (1) the elements generated by NT's with large changes of mass number A explained by the ND model obey the stability law and the isotopic ratios are the same to the natural ones while (2) the nuclides generated by NT's with changes ΔA of mass number = 1 and changes of isotope ratios are explained by the TNCF model [18]. This success of explanation of the data with both TNCF and ND models is consistent with the fundamental nature of the ND model with many-body interaction in a dense neutron matter as cf-matter like the neutron star matter and the fundamental single particle nature of the TNCF model.

6. Complexity in the CFP

The complex behavior of events in the CFP has been explained by analogy to bifurcation diagrams of the logistic difference equations as shown in Fig. 9 as shown in previous papers published in Proc. JCF8 [16, 21].

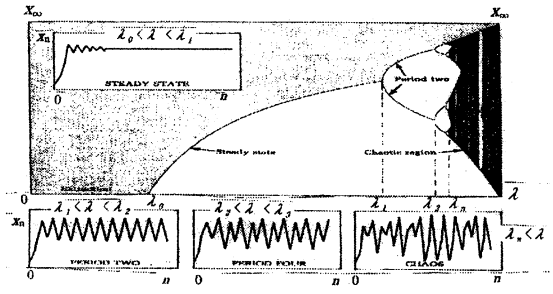

Fig. 9. Bifurcation diagram to show period- doubling and chaos [21].

7. Conclusions

Using a new knowledge about nonlocal wavefunctions of hydrogen isotopes adsorbed on the surface of the metal catalysts, we could extend our investigation of the CFP to all substances including from transition-metal hydrides/deuterides to hydrocarbons and biological bodies. The difficulty to induce nuclear reactions in room-temperature solids have been overcome by the use of neutrons which have no problem of the Coulomb barrier penetration and the question of the quantitative reproducibility by the characteristics of the CFP as a complexity. Complex features of the CFP have been understood by analogy to the bifurcation diagrams calculated for the logistic difference equation.

Acknowledgement

The author would like to express his heartfelt thanks to John Dash for his permission to stay in his laboratory which made possible to develop the investigation presented in this paper. This work is supported in part by a grant from the New York Community Trust.

References

1. M. Fleischmann, S. Pons and M. Hawkins, "Electrochemically induced Nuclear Fusion of Deuterium," *J. Electroanal. Chem.*, **261**, 301 – 308 (1989).

2. H. Kozima, *The Science of the Cold Fusion Phenomenon*, Elsevier Science, 2006. ISBN-10: 0-08-045110-1.

3. H. Kozima, *Discovery of the Cold Fusion Phenomenon*, Ohtake Shuppan, Tokyo, 1998. ISBN: 4-87186-044-2.

4. Kozima, H., "Quantum Physics of Cold Fusion Phenomenon," *Developments in Quantum Physics Researches – 2004,* pp. 167 – 196, ed. F. Columbus and V. Krasnoholovets, Nova Science Publishers, Inc., New York, 2004. ISBN 1-59454-003-9

5. H. Kozima, "Physics of the Cold Fusion Phenomenon" *Proc. ICCF13* , pp. 690 – 703 (2008). ISBN 978-5-93271-428-7

6. P. Gosar and M. Pintar, "H_3O^+ Ion Energy Bands in Ice Crystals," *phys. stat. sol.* **4**, pp. 675- 683 (1964).

7. Alefeld, "Hydrogen Diffusion in Metals," in A. Seeger, D. Schumacher, W. Shilling and J. Diehl Eds., *Vacancies and Interstitials in Metals*, North-Holland Pub. Co., Amsterdam, 1970. SBN 7204-0154-2

8. J.A. Sussmann and Weissman, "Diffusion of H and D in Niobium," *Phys. Stat. Solid,* 53, 419 (1972).

9. H.K. Birnbaum and .K. nd C.A. Wert, "Diffusion of Hydrogen in Metals," *Berichte der Bunsen-Gesell.* **76,** 806 – 816 (1972).

10. Z. Paal and P.G. Menon Eds., *Hydrogen Effects in Catalysis*, Marcel Dekker Inc., N.Y., 1988. ISBN 0-8247-7774-3.

11. C.M. Mate and G.A. Somorjai, "Delocalized quantum nature of hydrogen adsorbed on the Rh(111) crystal surface" *Phys. Rev.* **B34**, 7417 – 7420 (1986).

12. K.R. Christmann, "Hydrogen Sorption on Pure Metal Surface" in Z. Paal and P.G. Menon Eds. *Hydrogen Effects in Catalysis*, Marcel Dekker Inc.,

N.Y., 1988. ISBN 0-8247-7774-3.

13. J.W. Negele and D. Vautherin, "Neutron Star Matter at Sub-nuclear Densities," *Nuclear Physics*, **A207**, 298 - 320 (1973).

14. K. Riisager, "Neutron Halo States" *Rev. Mod. Phys.* **68**, 1106 – 1116 (1994).

15. H. Kozima, "Methodology of the Cold Fusion Research," in *ACS Sourcebook* J. Marwan and S. Krivit Eds., Oxford Univ. Press, 2009 (to be published).

16. H. Kozima, "The Cold Fusion Phenomenon as a Complexity (3) – Parameters Characterizing Cold Fusion Systems," *Proc. JCF8,* pp. 85 – 91 (2007).

17. H. Kozima and T. Mizuno, "Nuclear Transmutations in Polyethylene Films (XLPE) and Phenanthrene," *Reports of CFRL*, 8-4, 1 – 18 (2008).

18. H. Kozima and T. Mizuno, "Investigation of the Cold Fusion Phenomenon in the Surface Region of Hydrogen Non-occlusive Metal Catalysts; W, Pt, and Au," *Proc. JCF9* (to be published in this issue).

19. H. Kozima, "An Explanation of Nuclear Transmutation in XLPE (Crosslinked Polyethylene) Films with and without Water Trees," *Proc. JCF8,* pp. 44 – 50 (2007).

20. H. Kozima and H. Date, "Nuclear Transmutations in Polyethylene (XLPE) Films and Water Tree Generation in Them," *Proc. ICCF14*, (to be published).

21. H. Kozima, "The Cold Fusion Phenomenon as a Complexity (2) – Parameters Characterizing Cold Fusion Systems," *Proc. JCF8,* pp. 79 – 84 (2007).

Principle of Condensation for Nuclear Fusion

Norio YABUUCHI
High Scientific Research Laboratory
2nd Floor, Takano Building, 24-16 Marunouchi, Tsu, Mie 514-0033, JAPAN
E-mail: yabuuchi@kogakken.co.jp

Preface

A result of the nuclear reaction by ThePons-Fleischmann test tube experiment using hydrogen absorbing alloy has a big influence on an atomic nucleus, a numerator and astrophysics. Unification theory of the power of three; the nuclear force and the electromagnetic force,and gravity force, Einstein couldn't achieve, even does created expectation. The author can think the key is in spatial Pythagorean theorem in the Platonic Structure and dissipation theory of Nico squirrel and PURIGOJINU (Self-Organization in Nonequilibrium Systems) like Einstein, Kepler and Descartes.

The heavy electronic theory which got a hint from theory of Josephson's superconduction .

The author put emphasis on Bohr's correspondence this time and developed classical resembling dynamics by a principle of condensation fusion, and it was possible to get a more decisive and new conclusion. other words, so that carbon 60 may be produced in a vacuum indeed so that it may be insisted on by Prigogine. The author assumed that occluded deuteron and a heavy electron were arranged by hydrogen absorbing alloys in the Plato -nic structure in the bowels by Form and called Self - Organization by philosophy of Form.

Heat fusion is making a big error. In other words, we consider only the fusion which made the equation in Colomb barrier the premise.The equation of Colom barrier ($U=ZZ^{+}e^{+}e/r$)consists of only positive charge. Only repulsion functions between the positive charge of course. Fusion isn't made of this reason forever. But a law of Colomb's gravity($F= {}^{+}e^{-}e /4\pi\varepsilon r^2$, $F = {}^{+}e^{+}e/4\pi\varepsilon r^2$) which consists of the positive electric charge and the negative electric charge is also included in gravity as well as repulsion. Therefore. The author thought and announced fusion by combination with deuteron of the positive electric charge and an electron of the negative electric charge last time. The cube polyhedral structure was most suitable, so an author calculates the theory this time.

Discussion

1. Elucidation Based on Pythagorean Principles

In Fig1, positively charged deuterium nuclei (hereinafter termed deuterons, or D) and negatively
charged electrons are alternately arranged at the vertices of a cube by the action of self-organizationaccording to dissipation theory – that is to say,by form– so as to exist in the Platonic structure depicted.

Get a hint in the experimentation by Yoshiaki Arata and the author have added heavy electronic concept .

The author revealed that the four heavy electrons and four deuterons invade the gap space between the elements of the lattice of a hydrogen-occlusion alloy, it is understood that, similarly to superconductivity, the four deuterons

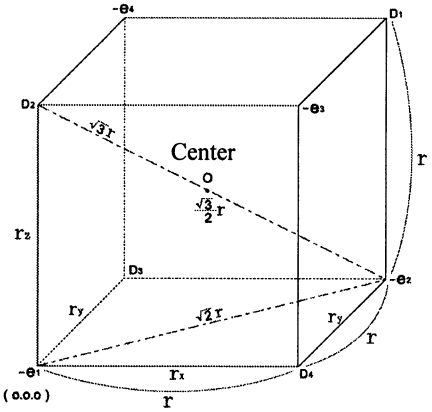

Figure 1 – Yabuuchi Model

Fig1,deuterons and electrons arranged at the vertices of a cube, a Platonic structure, and their relationship to the Pythagorean theorem

The distances between adjacent electrons and deuterons are all equal and form the 12 edges of a cube, and the distance of each is taken to be r.

$$r = 1 \qquad > 0 \qquad (1)$$

Next, the distance between e_1 and e_2 is taken to be r_{e1e2}. Similarly, the distances between e_1 and D_4 and between e_2 and D_4 are respectively taken to be $r_{e1D4}$and r_{e2D4}. Because of the Pythagorean theorem, the ratio to unit length r in r_{e1e2} is:

$$r_{e1e2} = \sqrt{2}r \qquad (2)$$

r_{e1D2} is:

$$r_{e1D1} = \sqrt{3}r \qquad (3)$$

The ratio to unit length r in re1,O is:

$$r_{e1,o} = \sqrt{3}/2 \cdot r \qquad (4)$$

This holds for all relationships between deuterons and electrons existing at vertices in regular polyhedra.
Pythagorean theorem is a great theory because of Plato's regular polyhedron is explained.
AINSHUTAIN calculated contract in space-time correctly by a Pythagorean theorem . For example.

$$c^2 t'^2 = c^2 t^2 + v^2 t'^2$$
$$(c^2 - v^2) t'^2 = c^2 t^2$$
$$t'^2 = (1/(1 - (v/c)^2)) t^2 \quad (5)$$

Next, there is a law of the probability of the transition of Cabbibo, Kobayashi, and Masukawa of the theory of elementary particle.
The probability that the up quark changes into the down quark is a^2 . The probability that the up quark changes into a strange quark is b^2 . The probability that the up changes into the down is L^2. Then, the relation between $a^2$and b^2 and L^2 : from Pythagorean theorem.

$$a^2+b^2=L^2 \quad (6)$$

The structure of the solar system was assumed to have the polyhedron structure according to Kepler and Descartes.
Recently, mathematician Jeffrey Weeks in the United States used Pythagorean theorem etc. , and the thory Kepler andDescartes was proven.
Length of Euclid there

$$\sqrt{a^2}+\sqrt{b^2}+\sqrt{c^2}+\sqrt{d^2} \quad (7)$$

is used and calculated.
The theorem of Pythagoras of the next expression is used to calculate the vector of the methane in the field of a molecular chemistry.

$$(1/\sqrt{3})^2+(1/\sqrt{3})^2+(1/\sqrt{3})^2=1 \quad (8)$$

Thus, the theorem of Pythagoras of the Euclidean geometry being applied to the calculation of the atomic nucleus structure and elementary particle, astrophysics, moleculechemistry, and our Platonic structure can have hope in the unified force theory of space. Especially, Euler's theorem is expected the most powerful union theorem. In other words, by the formula (V + F - E =2) of the oiler, it is unified with 2.

2. Deuterons, Electrons, and Coulomb's Law

Coulomb's law is as follows:

$$F=q1q2/4\pi\varepsilon r^2 \quad (1)$$

F is proportional to the charge regardless of proton and electron mass, and are inversely proportional to the distance r.
It's considered that 4 electrons and 4 protons invade space of a crystal lattice of a solid alloy by Aratas experimental hint of electron and deuteron was expanded.

In this case, as shown in Fig 1, four electrons and deuterons each are taken to be arranged in mutual alternation to form a cube, a Platonic polyhedron, by the action of the self-organizing force. The balanced condensation force F of the Coulomb attraction and repulsion acting between the mutual electron and deuteron pairs is investigated.
The distance between the apexes of a cube, r is 1.

$$r = 1 \quad (2)$$

Based on fig 1 calculate we calculate (1)
The total of Colomb attraction is

$$F(at) = (\sqrt{3}/9+1)\cdot 1/4\pi\varepsilon\cdot(rx+ry+rz)$$

The total of Colomb repulsion is

$$F(re)=-\sqrt{2}/2\cdot 1/4\pi\varepsilon\cdot(rx+ry+rz)$$

Condensation force as total F is next equation

$$F = 0.84F \quad (3)$$

F or F(con) expresses condensation force
F orF(re) expresses coulomb force(repulsion)
Based on this, the ratio of attraction and repulsion at e_1 is revealed to be attraction (F) 0.84 times greater than repulsion, thus accounting for the condensation toward the face center of the cube, and verifying that the same can be said for the values of e and D at the other vertices.

3. Distance and Other Factors at the Time of Collision Between an Electron and a Deuteron and Between Deuterons

Specifically, with respect to a collision between the electron and deuteron while moving from the vertices toward the body center O in the cube depicted in Fig 1, according to (3) of chapter 2, the Coulomb condensation force acting upon the condensation is

$$F = 0.84F \quad (1)$$

Deuteron radius: $r_D = 4.31\text{fm}$ (2)
Deuteron velocity: $V_{D0} = d\langle x\rangle/dt = (1/8)C$ (3)
C is velocity of light
The mass of the deuteron

$$m = 3.55 \times 10^{-27}\ [\text{kg}] \quad (4)$$

. The rate of the alpha particle was 1/16 of light speed C, so the mass of the deuteron requested 1/8 of C as the half.
Like Superconductivity, equally electron swarm of a group make the mass of 1 electron in it heavy, The heavy deuteron that 5, 400 times are heavier in three than one electron with which an electron is surrounded makes the mass of the electron heavy.
That is to say, for electron mass,

$$m_e = 300m_{e0} \text{ to } 1.000m_{e0}$$
$$m_{e0} = 9.11 \times 10^{-31}\ [\text{kg}], \quad (5)$$

and so electron velocity is pulled by the deuteron charge, this velocity is a necessary condition, and so it yields this

$$d<x>/dt = Ve = (1/8)C \quad (6)$$

The center, the electron, and the deuteron at the time of collision, based on Fig 2, are:

$$R_1 = 31.8 \text{ [fm]} \quad (7)$$

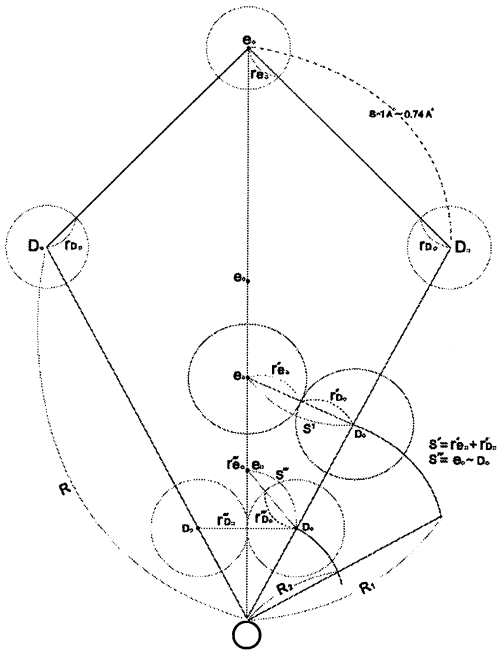

Fig 2
Fig2, depicting two deuterons and one electron ongoing condensation to the center of the Cube

After collision, the electron, according to the theory of observation, is in a state equivalent to that of having been observed at the site of collision by the large deuteron, and it is stripped of its wave packet and shrinks to a naked electron. the radius becomes $r = 2.50 \times 10^{-18}$ [m]. (8)
This distance of R_1=31.8 [fm] from the center.
next, distance R2 from the deuteron to the center O,

$$R_2 = \sqrt{3}/2 \cdot rs^{*} = 5.29 \text{ [fm]}. \quad (9)$$

This is the distance between the deuteron and the body center at the time of collision between mutual deuterons.

4. Coulomb Potential at the Bohr Radii of Electrons That are 300 Times Heavier and Deuterons

With regard to the Coulomb potential energy at the Bohr radii of the 300-times-heavier subnucleon electron and deuteron, within the alloy, as with electrons involved in superconductivity, the phenomenon of electrons 300 to 1,000 times heavier than normal electrons occurs, and so in this case as well, occurrence of a similar heavy-electron phenomenon is required.
Assuming the Coulomb potential Ue`` when the distance r between the electron and the deuteron is equal to B`` yield this:

$$Ue`` = 1.46 \cdot e^2/4\pi\varepsilon B`` = 1.11 \times 10^4 \text{ [eV]}$$

(1)
The Coulomb attraction of the electron heavy 300 times as of Bohr radius is expressed in the next equation

$$F = 3.91 \times 10^{16} \text{ [eV/m]} \quad (2)$$

Coulomb attraction is quite bigger than Coulomb potential.
But, in case of usual electronic weight nuclear fusion surely take place. Because an electronic wave packet is big in this case. Deuteron and an electron collide early.
It is the distance is (R_1=) 8410fm from Collision spot
to center of cube body. Because Bohr radius is the usual size. Energy of condensation for electron burst into Bohr radius is 4. 33×10^{11} [eV/m] .
Calculation after this will be development like a heavy electron.

5.Coulomb Attraction and MovementEnergy at the Time of Collision Between DeuteronsD

The Coulomb attraction applied to the electrons at this time of collision between deuterons is:

$$|F``| = 0.84 \cdot e^2/4\pi\varepsilon r^2 s`` = 32.4 \times 10^{18} \text{ [eV/m]} \quad (1)$$

The movement energy in the case of mutual collision between deuterons in this event is similarly calculated as follows:

$$E_D = 15.0 \times 10^6 \text{ [eV]} \quad (2)$$

which is sufficient collision movement energy for nuclear fusion.

6. Movement Energy of Electrons Passing the Bohr Radius of a Heavy Electron

First, when electron mass was 300 times greater , than according to the formula, the Bohr radius was

$$B = 4peh^2n^2/m_e \cdot e^2. \quad (1)$$

The size of the effective mass, $me`` = 300\ m_e$.
When the energy that the electron obtains by Coulomb attraction is taken to be ΔW_{e1},

The formula for work is $\Delta W_{e1} = -\int_{r1}^{r2} F dr$, (2)

$$\Delta W_{e1} = -\int_{0.64 \times 10^{-10}}^{1.52 \times 10^{-13}} (0.84 \cdot e^2/4\pi\varepsilon) r^{-2}\, dr = 7.94 \times 10^3 \text{ [eV]} \quad (3)$$

$$Ee_1 = 1/2 \cdot 300\, m_{e1} (1/8 \cdot C)^2. = 1.92 \cdot 10^{-13} \text{ [J]} \quad (4)$$

When movement energy at the Bohr radius B`` is taken to be $E``_{e1}$, equations (3) and (4) yield this:

$$E``_{e1} = E_{e1} + \Delta W_{e1} = 1.21 \times 10^6 \text{ [eV]} \quad (5)$$

In the same way, calculation of kinetic energy with an electron mass of 600 times greater at the location of B`` yield this:

$$* E_{e1} = 2.42 \times 10^6 \text{ [eV]} \quad (6)$$

Therefore, according to (5) and (6), bcause of energy of $1.21 \sim 2.42 \times 10^6$eV, the electron breaks through the base state at the Bohr radius and condensing force is exerted by the electron.

7 Secondary impact and nuclear fusion

The deuteron and between the deuteron collide with the first collision by quite high energy of kinetic energy of 15×10^6 [eV] is known. . Because of the principle of the condensation of (3) of second chapters . collective strength of Coulomb attraction is always bigger than collective strength of Coulomb repulsion, without needing a tunnel effect nuclear fusion by the collision between the deuteron beyond the top of the mountain of Coulomb repulsion is known.

We calculate whether the Be of the compound nucleus can be made nuclear fusion by the collision of Helium of the compound nucleus aspect each other next.

The mass of the deuteron is (m_D=) 3.35×10^{-27}[kg] and the speed of deuteron is (V=) 1/8・C, Like fig3, deuterons collide with aspect each other and makes nuclear fusion and become Helium of the compound nucleus.

Helium of a compound nuclei and helium of the compound nuclei which has advanced from the other side and has come cause nuclear fusion by the remains energy after impact, and become to beryllium of a compound nuclei. This expectation is calculated next.

The next expression is given from relations with (2)0f chapter 5. $1/2 \cdot mv^2 = 15.0 \times 10^6$ [eV]

According to fig 3,Kinetic energy P_1 of two deuterons before the collision

$$P_1 = 30 \times 10^6 \text{ [eV]} \quad (1)$$

$$mv\sin\theta + mv\sin\theta = mv' \sin 90^\circ + mv' \sin 90^\circ$$

$$\sin\theta = v' \quad (2)$$

$$P_2 = P_1(\cos^2\theta) = 20.1 \times 10^6 \text{ [eV]} \quad (3)$$

T as Consumption of the energy for two of deuteron tomake compound nuclei helium is as follows.

$$T = P_1 - P_2 = 9.9 \times 10^6 \text{ [eV]} \quad (4)$$

In other words, By collision of two deuteron consumed a collision energies of 9.9×10^6 [eV]

Accoding to equation (3) , Collision energies of two helium of compound nuclei make a compound Beryllium is (P_2=) 20.1×10^6 [eV]. This beryllium of an excited compound nuclei splits into 2 helium again .

This process is shown as follows.

$$^2D + ^2D + ^2D + ^2D \rightarrow ^4He_2 + ^4He_2$$

$$\rightarrow ^8Be^*_4 \rightarrow ^4He_2 + ^4He_2$$

$$= 47.6\,MeV \quad (5)$$

(where "*" indicates compound nuclei),

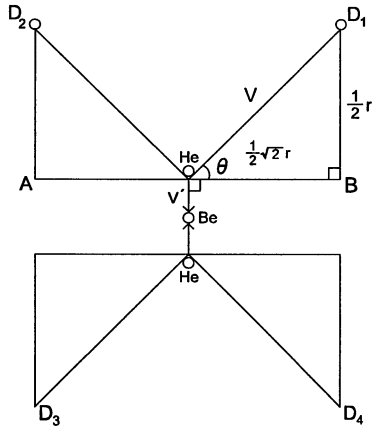

Figure 3
Development of D,He,Be,by two times of nuclear fusion

Accordingly, two deuterons must overcome the Coulomb barrier with movement energy of 15.0 10^6[eV],30.0MeV in total, colliding and experiencing fusion. This spot is 5.29fm from the center point. Deuteron two of kinetic energy 30.0MeV collide when I calculate and consume energy of 9.9MeV. Compound nucleus helium and the compound nucleus helium of the other side collide in kinetic energy 20.1 MeV of a composed collision at the center point and compose activated beryllium and return to helium again. The mass defect energy by this nuclear fusion process is 47.6MeV.

But the structure of the perfect cube can't be made with 4 electrons and 4 of deuteron in the solid, we don't get the big energy because of grazing collision.

By the way, four electrons normal not four heavy electrons made nuclear fusion with four deuterons, I calculated. The same result was given .

However, the different point was $R_1 = 8.41 = 10^{-12}$ [m] The calculation after the R_2 spot was the same.

A note without reviewing

An Explanation of Helium Concentration in Chupadera Mesa in New Mexico by Hydrogen-fusion

Hiroshi Yamamoto
3110-17, Tsuzuki, Mikkabi-Town, Kita-Ku, Hamamatsu-City, Shizuoka-Pref. Zip:431-1402, Japan
e-Mail: hughy@aqua.ocn.ne.jp

Abstract: Helium is contained in natural gases and its concentration varies from nearly zero to 8% (mole percent), but it is not clear why the helium concentration in some case is so high as 8%. It is commonly perceived that ^{4}He is generated by radiogenic decay of uranium and thorium and ^{3}He is mostly primordial and derived from the mantle. S. Jones proposed geo-fusion of deuterium in condensed matter within the earth [1]. The author proposed earthquakes are caused by hydrogen fusion whose outcomes are both ^{3}He and ^{4}He [2]. The helium isotope ratio (^{3}He/^{4}He) is a good tool to determine the origin of helium. The atmospheric isotope ratio, *Ra* is 1.4×10^{-6}. The helium isotope ratio of the most of natural gas wells in USA is under 0.08*Ra* but Chupadera Mesa in New Mexico has 0.515*Ra*, about 6 times higher [3]. It is reported that helium content increases with proximity to the faults [4]. This strongly suggests that dense helium was first made at the faults and then propagated. The coincident of the faults and high helium concentration in Chupadera Mesa in New Mexico indicates helium was made at the event of earthquakes by hydrogen fusion and high helium isotope ratio (^{3}He/^{4}He) of 0.515*Ra* is due to the unburned ^{3}He in the event of earthquakes.

Key words: helium concentration, helium isotope ratio, hydrogen fusion, geo-fusion, earthquake, faults

1. Introduction

Helium is contained in natural gases and its concentration varies from nearly zero to 8%(mole percent). Helium concentration of the most of natural gas wells in USA is below 0.3%, but some in New Mexico which are located on the dense fault zone contain as much as 8% of helium [3]. Interestingly, helium content increases with proximity to the faults [4]. It is commonly perceived that ^{4}He is generated by radiogenic decay of uranium and thorium and ^{3}He is mostly primordial and derived from the mantle. S. Jones proposed geo-fusion of deuterium in condensed matter within the earth [1]. In this case outcomes are tritium and ^{3}He (^{4}He is negligibly small). The author proposed earthquakes are caused by hydrogen fusion whose outcomes are both ^{3}He and ^{4}He [2]. If high content of helium in New Mexico natural gas wells could be explained by hydrogen fusion, this will reinforce the hypothesis that the cause of earthquakes is hydrogen fusion. The helium isotope ratio (^{3}He/^{4}He) is a good tool to determine the origin of helium. The atmospheric isotope ratio, *Ra* is 1.4×10^{-6}. The helium isotope ratio of the most of natural gas wells in USA is under 0.08*Ra* but Chupadera Mesa in New Mexico has 0.515*Ra*, about 6 times higher [3]. This suggests part of helium was derived from the mantle or geo-fusion or earthquakes caused by hydrogen fusion.

2. Earthquakes Induced by Water Injection

In 1961, a deep well was drilled at northeast of Denver Colorado U.S.A for disposal of nuclear waste fluids. Injection was commenced March 1962, and shortly after that, an unusual series of earthquakes erupted in the area. Injection had been discontinued and the number of quakes decreased dramatically. When the injection was resumed, quakes increased accordingly and the link between the fluid injection and earthquakes was established [5]. The most notable experience in this series of earthquakes is that many people heard extremely loud, explosive-like earth noises.

3. Fusion of Hydrogen Dissociated from Water under the Ground

R.L. Mills has reported that atomic hydrogen can generate energy somewhat between chemical reaction and nuclear reaction by lowering the electron orbit from the ground state to lower state [6]. According to Mills, hydrogen atoms can achieve lower states than ground state by a resonant collision with a nearby atom or combination of atoms having the capability to absorb the energy to effect the transition, namely, an integer multiple of the potential energy of the electron at atomic hydrogen, m*27.2 eV (m is an integer) . He named this shrunken hydrogen atom hydrino and claims that this hydrino can be a catalyst to shrink other hydrinos to further lower states. He named this reaction the BlackLight Process.

The Earth's crust is divided into several separate solid plates. Subduction occurs when two plates collide and the edge of one dives beneath the other. The crust contains water and when it contacts with metals such as iron, atomic hydrogen will be produced according to the following reaction.

$3Fe + 4H_2O = 8H + Fe_3O_4$, where H designates atomic hydrogen.

Once atomic hydrogen is produced and if there is no heat sink at the collision point, just a collision of atomic hydrogen, for instance, $H + H = H_2$ (molecular hydrogen) wouldn't take place but just elastically repulse each other. This suggests that high pressure atomic hydrogen gas will build up under the ground. Simultaneous collision of 3 atomic hydrogen is the BlackLight Process because the

ionization energy of hydrogen is 13.6eV and the sum of the ionization energy of 2 hydrogen is 27.2eV.

$H + H + H = [H_{n=1/2}] + 2p + 2e$

p designates proton and $[H_{n=1/2}]$ designates a hydrogen whose electron orbit is shrunken to 1/2 the radius of a normal one and these will be shrunken further to lower orbits as reaction continues. It can be postulated that if containing vessels are tight enough as is the case of the underground, well shrunken hydrinos which have a relatively small Coulomb barrier can fuse each other resulting in the generation of mainly ^4He and a fraction of ^3He.

Fig 1 illustrates the hydrogen fusion.

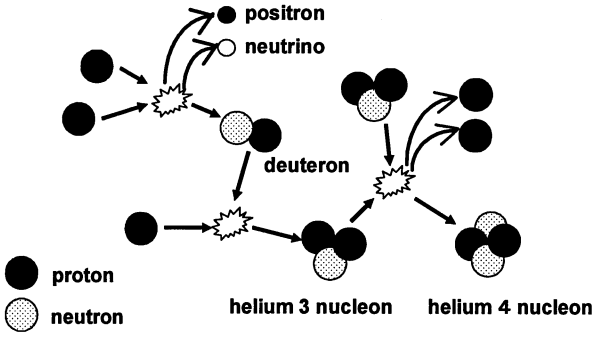

Fig. 1 Process of hydrogen fusion

5. Triggering of Hydrogen Fusion under the Ground

High pressure molecular hydrogen gas up to 70MPa is now being used for fuel cell cars but almost no technical information on the stability of high pressure atomic hydrogen gas is available because it's almost impossible to make such a gas here on the ground.

Only information available concerning the initiation of the BlackLight process is the one carried out by BLACKLIGHT POWER Inc., but these are limited at very low pressure. The Black-Light process is quite sensitive to the pressure and it can be expected that the same characteristic curve as is the case for the self ignition curve of the stoichiometric mixture of hydrogen and oxygen shown in Fig 2.

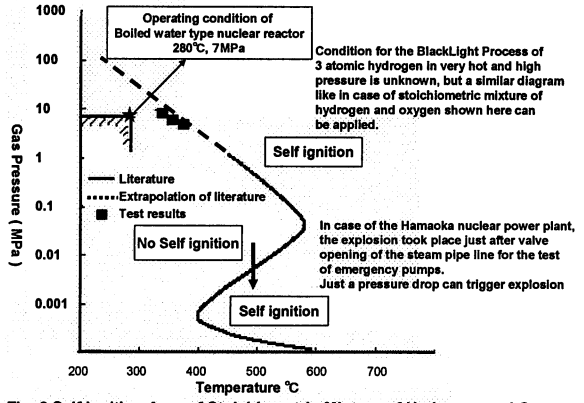

Fig. 2 Self Ignition Area of Stoichiometric Mixture of Hydrogen and Oxygen

Source:Chubu Electric Power Company:
Reactor Manual Shutdown Caused by Pipe Rupture in Residual Heat Removal System at the Hamaoka Nuclear Power Station Unit-1 (Final Report), April 2002 (In Japanese).

The author has reported that when the gas pressure of atomic hydrogen reaches such a high pressure that surrounding rocks can not sustain, gas leakage starts and the atomic hydrogen gas plunges into the area of the BlackLight process, resulting in hydrogen fusion under the ground, namely earthquake [2].

According this assumption, it can be expected that there would be helium gas with high concentration near epicenter, namely faults.

6. Helium Distribution in New Mexico

It is commonly perceived that ^4He is generated by radiogenic decay of uranium and thorium and ^3He is mostly primordial and derived from the mantle. The helium isotope ratio ($^3He/^4He$) is a good tool to determine the origin of helium. The atmospheric isotope ratio, *Ra* is 1.4×10^{-6}. The helium isotope ratio of the most of natural gas wells in USA is under $0.08Ra$ [3].

Helium contents of some oil and gas reservoirs in New Mexico are as high as 8%. There are 3 major characteristics for this high concentration of helium.

1) Oil or gas wells with high concentration of helium are located on the densely distributed fault zones.
2) Helium content increases with proximity to the faults.
3) Helium isotope ratio of the one of the gas well, Chupadera Mesa is 0.515Ra, over 6 times bigger than the average.

7. Mechanism for High Concentration of Helium

One of the best known helium gas wells in New Mexico is the Four Corner platform. The content of hydrocarbon in this area is less than 20% and most of non helium fraction is nitrogen [3]. Helium migrates with nitrogen and hydrocarbon, typically methane.

In order to have a higher concentration of helium,

1) Nitrogen or methane have to react with other substances resulting in solid or liquid but it seems no such reaction is possible under the ground because these gases are very stable.
2) Helium may be supplied from the mantle. But, gas wells in Japan that are located close to active volcano zones contains as little as 0.5% of helium and it is unlikely that helium from the mantle can be concentrated over 1 %.

   We need to find out other mechanism for helium concentration.

The fact that helium content increases with proximity to the faults suggests high concentration of helium was made at first at a fault and then propagates outward.

8. Mechanism to Have High concentration of Helium at Faults

Faults are made by earthquakes. If we can assume that earthquakes are caused by hydrogen fusion, then, we can understand why

1) Oil or gas wells with high concentration of helium are located on the densely distributed fault zones.

2) Helium content increases with proximity to the faults.
3) Helium isotope ratio of the one of the gas well, Chupadera Mesa is 0.515Ra, over 6 times bigger than the average.

8. Summary

In the past, it could have been hardly imagined atomic hydrogen gas can explode by itself but the BlackLight process by R. Mills opened the way to investigate the cause of anomalous explosion of hydrogen from a new standpoint of view. From the relationship between water injection into deep wells and occurrences of earthquakes, it can be reasonably assumed that earthquakes are caused by fusion of hydrogen dissociated from water. The outcomes of hydrogen fusion are ^{4}He and a fraction of ^{3}He and this can explain helium concentration in Chupadera Mesa in New Mexico.

References

(1) S. E. Jones, E. P. Palmer, J. B. Czirr, D. L. Decker, G. L. Jensen, J. M. Thorne, S. F. Taylor, J. Rafelski, "Observation of Cold Nuclear Fusion in Condensed Matter," Nature 338, pp737-740

(2) H. Yamamoto,"An Explanation of Earthquakes by the Blacklight Process And Hydrogen Fusion," Proceedings of the 12th International Conference of Cold Fusion, pp. 577-581, Yokohama, 2005

(3) Broadhead, R, F, "Helium in New Mexico:Geologic Distribution and Exploration Possibilities", Presentation at Tulsa Geological Society, October 10, 2006

(4) Broadhead, R, F, "Helium in New Mexico-geologic distribution, resource demand and exploration possibilities, New Mexico Geology, Nov. 2005, Vol.27

(5) Nicholson, Craig and Wesson, R.L., "Earthquake Hazard Associated with Deep Well Injection," A Report to the U.S. Environmental Protection Agency, U.S. Geological Survey Bulletin 1951, pp.74 .

(6) Mills, R, "The Grand Unified Theory of Classical Quantum Mechanics", Blacklight Power Inc., 1999